Optical Properties of By-Design Extreme Wide Bandgap Semiconductor

A Dissertation

Presented in Partial Fulfilment of the Requirements for the

Degree of Doctor of Philosophy

with a

Major in Physics

in the

College of Graduate Studies

University of Idaho

by

Dinesh Thapa

Major Professor: Leah Bergman, Ph.D.

Committee Members: Matthew D. McCluskey, Ph.D.; M. Grant Norton, Ph.D.;

Dev S. Shrestha, Ph.D.

Department Administrator: Ray von Wandruszka, Ph.D.

December 2016

Authorization to Submit Dissertation

This dissertation of Dinesh Thapa, submitted for the degree of Doctor of Philosophy with a major in Physics and titled "Optical Properties of By-Design Extreme Wide Bandgap Semiconductor," has been reviewed in final form. Permission, as indicated by the signatures and dates given below, is now granted to submit final copies to the College of Graduate Studies for approval.

Major Professor _____Date_____
Leah Bergman, Ph.D.

Committee Members _____Date_____
Matthew D. McCluskey, Ph.D.

_____Date_____
M. Grant Norton, Ph.D.

_____Date_____
Dev S. Shrestha, Ph.D.

Department Administrator _____Date_____
Ray von Wandruszka, Ph.D.

Abstract

Alloying has the potential to create new types of semiconductors with novel optical properties that can be tailored to a specific application by the choice of the composition. ZnO and MgO in particular can be used to create the ternary $Mg_xZn_{1-x}O$ alloy system. In the alloy formula, x is the composition that spans the values 0 to 1. The two end members ZnO and MgO both have bandgaps in the UV range: ZnO at ∼3.4 eV (364.7 nm) and MgO at ∼7.5 eV (165.3 nm). Thus, depending on the composition x and the solubility limits, alloys with bandgaps between 3.4 eV and 7.5 eV can be achieved.

One of the desirable features of the $Mg_xZn_{1-x}O$ alloys is that the constituents ZnO and MgO are relatively environmentally friendly materials. Moreover, owing to the deep excitonic binding energies of ZnO and MgO and to their direct bandgaps, $Mg_xZn_{1-x}O$ is an attractive alloy system for the creation of luminescent materials with by-design wavelengths. However, a key obstacle to the realization of viable semiconductor alloys lies in the optimization of their optical properties in a manner that overcomes the impact of various types of defects. In this research, $Mg_xZn_{1-x}O$ alloy films over a wide range of Mg composition were synthesized via sputtering, and the optical and material properties of the films were explored utilizing several analytical techniques.

Main results of this research are: post growth annealing in Ar atmosphere ∼900 °C was found to enhance significantly the desirable UV luminescence. Specifically, for ZnO the enhanced UV luminescence correlated well with the elimination of native defects and improved film's morphology. In the case of $Mg_xZn_{1-x}O$ alloys, the enhanced UV luminescence was found to be related to the reduction of alloy inhomogenity as well as improvement of films's morphology. Moreover, as this alloy system has inherent phase segregation, it is important to consider the composition range where structural segregation occurs. We utilized XRD and selective resonance Raman scattering (SRRS) to study this issue. It is shown that SRRS is highly sensitive optical technique to detect the structural inhomogeneity in the $Mg_xZn_{1-x}O$ alloys.

Acknowledgments

First, I express my sincere appreciation to my advisor Dr. Leah Bergman for her constant support, intellectual input and enlightening guidance through out this work.

I am grateful to my committee members Dr. Matthew D. McCluskey, Dr. M. Grant Norton and Dr. Dev S. Shrestha for their support and advice during my research, and on my dissertation.

Dr. Jesse Huso, Dr. John Morrison and Dr. Hui Che and Amrah Canul all have been extremely helpful in the lab for discussion, and during experiments. I am grateful with Dr. Huso and Dr. Morrison for their hours of discussions in front of the white board. I am also thankful to Kevin Miklos and Bill Duncan for help in English writing.

I express deep gratitude to my parents; surely you had shown me the right direction holding my hand when I was a kid. I am grateful with my brother, Jivan, and can hardly express in words, even being younger than me you always put the family burden on your shoulders and left me free to complete my studies. I also extend my thanks to my nephews Kapil and Kushal making me smile while chatting.

I am grateful to my wife, Samikshya, for your encouragement and constant support; you helped me in many ways during the completion of this work.

Special thanks goes to Dr. Thomas Williams of the center for Electron microscopy and microanalysis for his help in taking the measurements and understanding the samples. I am also grateful with John Failla for his help in the instrumentation.

This work was supported by the U.S. Department of Energy, DE-FG02-07ER46386.

To my Late father Ramesh Thapa and mother Shova Thapa

Table of Contents

List of Tables

List of Figures

Chapter 1

Introduction

1.1 ZnO: a wide bandgap material

Wide bandgap semiconductor materials have been extensively studied due to their potential application in ultraviolet (UV) optoelectronic devices. Due to their capability to emit and absorb light in the UV spectral range, these materials have been utilized as a constituent material in photodetectors, light emitting diodes, laser diodes and as coating materials for protection against UV radiation.[1–6] Group II-VI oxides and group III-V nitrides are the most common examples of wide bandgap semiconductor materials.

As a wide bandgap semiconductor, ZnO is increasingly becoming an attractive material, capable of luminescence in the ultraviolet (UV) region with promising applications in UV optoelectronics. It has a direct wide bandgap ~ 3.37 eV[7] at room temperature, and relatively large excitonic binding energy (60 meV), both attributes of which make it an efficient UV luminescent material at room temperature and at elevated temperatures. ZnO is considered an environmentally friendly, non-toxic and benign material compared to most other semiconductors: it can be used as a dietary supplement in animal feed, as an additive in breakfast cereal, and as an ingredient in sunscreen.[8,9] Furthermore, ZnO is stable against radiation damage making it potentially useful in fabricating devices that can function in harsh environments. Likewise, a relatively lower growth temperature, a much simpler crystal technology compared to GaN and the amenability of a wet chemical method for its processing, potentially pave the way for design of low cost ZnO based devices.[10,11]

Like most other wide bandgap semiconductors, research on ZnO started early in the 1930's and continued for a long time. In an early study, CW Burn experimented using ZnO condensed from the smoke to settle a disagreement between the parameters

determined by x-ray and electron diffraction.[12] The optical studies on ZnO were then investigated in detail in 1954 by Mollwo[13], and the vibration properties were investigated by Damen et al.[14] in 1966. In 1967, Drapek demonstrated ZnO based hybrid heterostructures LEDs using Cu_2O as the p-type material.[15] Tsuraken et al. in 1975 utilized ZnO/ZnTe to create a p-n junction.[16] Indeed, after successful commercialization of GaN based optoelectronic and electronic devices, and some of the similarity in material and optical properties of GaN and ZnO, a renewed research interest on ZnO based wide bandgap materials was started.

Currently, ZnO is considered an alternative material to GaN, and has received a great deal of attention in the scientific community due to its applicability for UV optoelectronic devices such as in UV photo detectors, UV lasers, light emitting diodes, transparent thin-film transistors, and transparent conducting oxide for solar cells among others.[3–5,17,18] Additionally, ZnO based alloy material, specifically $Mg_xZn_{1-x}O$, where x is the composition of Mg, has provided a new tuneable family of wide bandgap material in UV luminescent applications as well as a potential conjugate material in AlGaN-MgZnO hybrid devices.

1.2 Bandgap engineering

Nature has provided materials with a specific, designated value for the bandgap, and spectral emission lines while optoelectronic technology requires much larger choices for the bandgap and emission lines than those found naturally. Bandgap engineering is a common practice to achieve these desired optical properties.

For bandgap engineering purposes, there are two principal ways: one is via quantum confinement, and another is via alloying. In this work, we utilized the alloying process to tune the bandgap, and for completeness a brief discussion of both routes in achieving the bandgap engineering has been presented in the next section.

1.2.1 Quantum confinement

Upon reducing the size of a semiconductor material down to the nanometer range as in the case of nanocrystals, and quantum dots, the electronic and optical properties start changing compared to the bulk counterpart. When the crystallite size is sufficiently small, the particle surface acts like a potential barrier and under its influence, the electrons in the conduction band and holes in the valence band are spatially confined. One may consider the spatially confined particles in a nanocrystal of dimension L to be a "particle in a box" problem in quantum mechanics and as such the energy eigenvalues associated with the particle can be expressed as:

$$E = \frac{h^2}{2m^* L^2}(n_x^2 + n_y^2 + n_z^2) \tag{1.1}$$

From equation 1.1 it is obvious that on reducing crystal size L, the value of E increases. Thus, by controlling the size of the nanoparticles, one can modify the electronic energy levels resulting in new luminescent lines.

The quantum confinement effect in nanocrystals gives rise to some unique optical properties such as a size-tunable bandgap, photoluminescence, and a high quantum yield, rendering these materials potentially useful in solar cells, light emitting diodes, and a novel light emitting display.[19–22] However, some limitations appear to exist while engineering the bandgap via this method. This technique allows the tuning of the bandgap to larger values, but it remains inapplicable whenever bandgap reduction is required. Likewise, through this technique the observable bandgap can be achieved as long as the dimension of the material is sufficiently small, on the order of Bohr's exciton radius. This leads to difficulties in their utilization in optoelectronic devices. Additional shortcomings arise from the self heating effect that might occur in the nanomaterial during device operation, defeating their sole purpose of bandgap tuning.

1.2.2 Alloying

Alloying is an efficient and a commonly used technique for bangap engineering which enables the bandgap tuning over a wide range via the mixing of semiconductors. Upon alloying, some of the lattice sites of the host semiconductor become occupied with the solute atoms, resulting in an alloy material with tailored optical properties. For example, in our study when we alloyed ZnO with a MgO semiconductor, some of the Zn lattice sites are occupied with the Mg atoms providing the $Mg_xZn_{1-x}O$ ternary solid solution.

Ideally, the $Mg_xZn_{1-x}O$ alloy should enable tuning of the bandgap, thus achieving tailored-by-design UV luminescence lines spanning over a wide range of energies extending from the bandgap of ZnO $\sim$ 3.4 eV to that MgO $\sim$ 7.5 eV. However, the different crystal structure of ZnO and MgO will hinder the fabrication of single phase $Mg_xZn_{1-x}O$ over a wide range of compositions. This issue will be briefly discussed in the next section. Despite the existing structural inhomogeneities in $Mg_xZn_{1-x}O$ alloy films for the higher Mg composition, bandgap engineering over a wide UV range of $3.2 - 5.8$ eV has been achieved by our group (Figure 1.1).

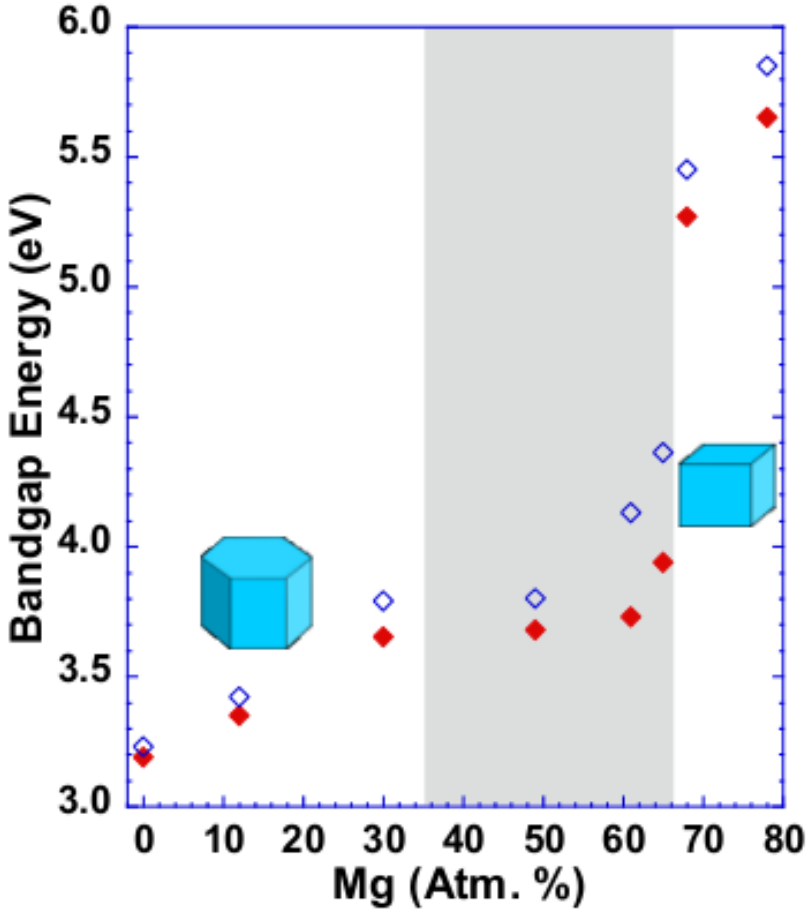

Figure 1.1: *The MgZnO alloy bandgaps as a function of Mg composition. The filled symbols are data points that were obtained via the derivative method while the open symbols are data points obtained via Tauc plot analysis to be discussed in a later chapter. The shaded area presents the phase segregation range obtained from the selective resonant Raman scattering analysis.*[23]

1.3 $Mg_xZn_{1-x}O$ alloy system and solubility issues

$Mg_xZn_{1-x}O$ alloys have emerged as promising semiconductors with excellent material and optical properties, including tunable bandgap, high exciton binding energy, and excellent thermal stability. These obvious useful properties make them potentially useful in UV luminescence, absorption, and lighting applications. $Mg_xZn_{1-x}O$ alloys have been particularly useful as a barrier layer for ZnO quantum wells, as an active component in UV light emitters, solar-blind UV detectors, and in other optoelectronic devices based on heterostructure functionalities. A key step in realizing these applications is in the growth of high quality $Mg_xZn_{1-x}O$ alloy materials. A specific issue that always exists and hinders the fabrication of such alloys over a wide range of Mg composition, is the limited solubility of Mg in ZnO.

The end members of $Mg_xZn_{1-x}O$ alloys (i.e. ZnO and MgO) have different crystal structures: ZnO has a hexagonal wurtzite structure as depicted in Figure 1.2(a) with tetrahedral co-ordination among the cations and anions, while the rock salt cubic structure of MgO as shown in Figure 1.2(b) exhibits octahedral co-ordination among the cations and anions. Upon alloying of these end members, some of the Mg atoms substitute the Zn lattice sites forming a $Mg_xZn_{1-x}O$ solid solution (Figure 1.3). Despite the similar value of covalent radii of Mg (1.36 $\mathring{A}$) and Zn (1.25$\mathring{A}$), the different crystal structures of the two oxides only allow for the synthesis of $Mg_xZn_{1-x}O$ alloys in a certain range of Mg composition. Figure 1.4 presents the phase diagram for the binary $Mg_xZn_{1-x}O$ alloy system as reported earlier by Segnit et al.[24] In accordance with this phase diagram, in the case of MgO dissolved into ZnO, the solid solubility of MgO is limited to $\sim$ 4 atomic percent while the solubility is limited to $\sim$ 40% when ZnO is dissolved in MgO. In the intermediate region of these compositions, phase segregation occurs wherein both the cubic and the wurtzite phase can occur with undefined optical properties.

Despite the solubility limits, there have been several reports on the growth of wurtzite $Mg_xZn_{1-x}O$ alloy films with a larger Mg content. In the earlier studies[1,2,25], $Mg_xZn_{1-x}O$ alloy films with single wurtzite phase up to $\sim 35\%$ had been realized utilizing the plasma laser deposition (PLD) technique. Additionally, in their studies, the $Mg_xZn_{1-x}O$ alloy films in the intermediate region of $\sim 35-50\%$ Mg composition were shown to have the mixed phase while above $\sim 50\%$ Mg composition, the alloys were reported to exit in the single cubic phase.[25] In our study, the phase segregation and strutural inhomogeneities inherent to $Mg_xZn_{1-x}O$ alloy films were investigated utilizing selective resonant Raman scattering, and will be presented in chapter 4. Despite the existing structural inhomogeneities in $Mg_xZn_{1-x}O$ alloy films for the higher Mg composition, bandgap engineering over a wide UV range of $3.2-5.8$ eV has been achieved by our group (Figure 1.1).

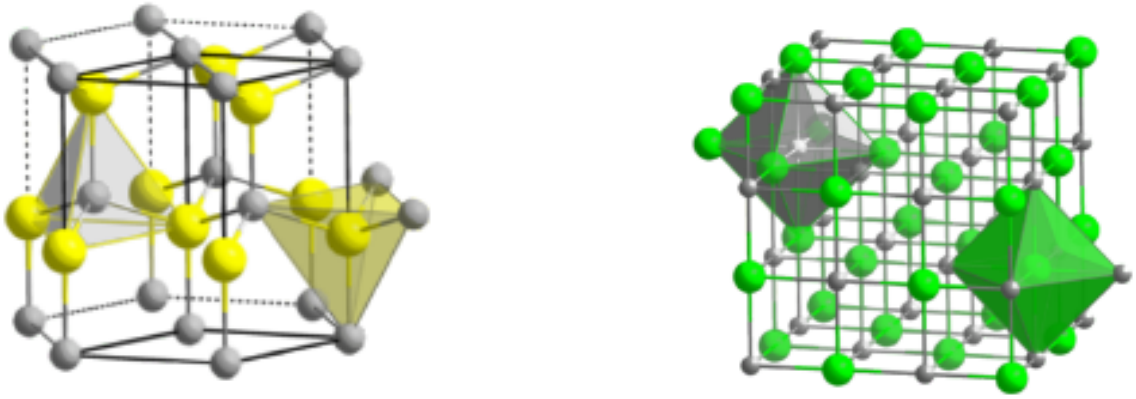

(a) (b)

Figure 1.2: *(a) The hexagonal wurtzite crystal structure of ZnO. The Zinc atoms are yellow while the oxygen atoms are black. The lattice parameters of the wurtzite ZnO crystal structure are a = 3.249 Å and c = 5.206 Å.*[26] *Zinc atoms have a covalent radii of 1.25 Å*[27] *, while oxygen has a covalent atomic radii of 0.73 Å.*[28] *(b) The rocksalt crystal structure of MgO. Mg atoms are shown in green while oxygen atoms are black. The lattice parameter for rocksalt MgO is, a = 4.216 Å.*[26] *The covalent atomic radii for Mg is 1.36 Å.*[27] *Figures taken from Ref.*[29]

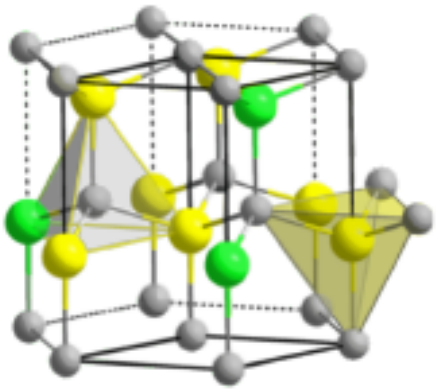

Figure 1.3: *Wurtzite structure of $Mg_xZn_{1-x}O$ film. Oxygen atoms are in black, zinc atoms are in yellow, and magnesium atoms are in green. In the alloying process, some of the magnesium atoms occupy crystal sites which would otherwise be filled with zinc atoms in this structure. Figure taken from Ref.*[29]

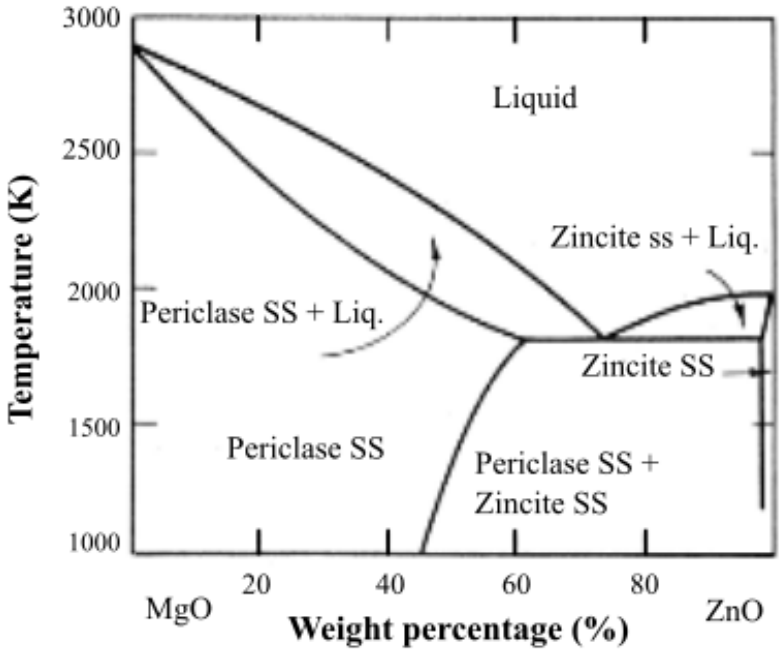

Figure 1.4: *Phase diagram of a ZnO-MgO alloy system as reported by Signet et al.*[24] *Under thermodynamic equlibrium, for Mg composition* $\sim 0-4$ *at% (*$\sim$ *0-2 wt%), the* $Mg_xZn_{1-x}O$ *alloy film retains a wurtzite crystal structure, and above* ~ 40 *at% (*$\sim$ *55 wt%) of Mg, the alloy system will exhibit the cubic phase. In the intermediate region* $\sim 4-40$ *at% Mg a mixed phase exists.*

1.4 UV luminescent properties and defects

As mentioned above, ZnO owing to its unique optical properties is emerging as a leading technological material for next-generation UV optoelectronic devices. In order to realize these potential applications, it is crucial to achieve ZnO materials with high-optical quality that exhibit strong UV luminescence. However, during the growth of ZnO samples, some native defects and impurities can be introduced, and these can impact the material properties significantly. Native point defects will be formed when some of the constituent atoms sit in the interstitial position between lattice sites, are missing from the lattice position, or sit wrongly in the lattice site and are interrupting the periodicity in the crystal. The possible native defects in ZnO include the zinc interstitial (Zn_i), oxygen interstitial (O_i), oxygen vacancy (V_O), zinc vacancy (V_{Zn}), oxygen antisite (O_{Zn}) and zinc antisite (Zn_O).

Indeed, the creation of defects inside the crystal may cost energy; however the increased configurational entropy resulting from the defects reduces the free energy of the system, which in turn favors the formation of point defects.[30] Typically, native defects are unavoidable, and can be present in even the best crystalline material. Hence, irrespective of any growth method and substrate used for the growth of the material, native defects always tend to be present.

Native defects generally bring undesirable effects; specifically, they influence the optical and electrical properties of the material. Defects in semiconductor materials introduce sub-bandgap states which act as recombination centers and impede the efficient emission of light.[30,31] Another important aspect that can be influenced by the defects is the doping of the material. In ZnO, p-type doping has been a big challenge, and this has been attributed to self-compensation effects caused by native defects and impurities.[32] Additionally, the presence of defects in the host material are reported to degrade the device performance and the device operation lifetime. In light of the above

discussions, identification and elimination of the defects has become a key issue.

In this work, an assessment of existing defects and their impact on UV luminescent properties of ZnO and $Mg_xZn_{1-x}O$ films has been carried out and will be presented in chapters 5 and 6. Specifically, in chapter 5, the defect dynamics and their impact on optical properties of ZnO were studied via post-growth annealing in argon (Ar) or O_2 ambient with X-ray diffraction (XRD), imaging, transmission, Urbach analysis, Raman scattering, and photoluminescence (PL). Similar investigations were carried out in achieving the enhanced UV luminescence for the $Mg_xZn_{1-x}O$ alloy film, and will be presented in chapter 6.

1.5 Focus and outline of the study

The focus of this dissertation work is the investigation of the optical and structural properties of ZnO and $Mg_xZn_{1-x}O$ alloy films. The method of synthesis of the films will be presented in chapter 2 while a brief discussion on the spectroscopic techniques including transmission, photoluminescence, Raman spectroscopy utilized in this work will be described in chapter 3.

One aspect of this study is to achieve bandgap tuning via the realization of $Mg_xZn_{1-x}O$ alloy films. Ideally $Mg_xZn_{1-x}O$ alloy films are expected to allow the bandgap tuning spanning from 3.37 eV (bandgap of ZnO) to 7.7 eV (bandgap of MgO). In order to investigate this possibility, $Mg_xZn_{1-x}O$ alloy films with Mg composition ranging from 0 to 78% were successfully grown, and their bandgap tunability was explored, and will be presented in chapter 4.

Another aspect that has been the focus of this study is phase segregation and structural inhomogeneity, an inherent issue for the technological application of $Mg_xZn_{1-x}O$ alloy films. The covalent radii of Zn and Mg are comparable; however, because of the different crystal structures, the two oxides do not exhibit a complete solid solution and an intermediate composition range exists in which an alloy is phase separated into the

wurtzite and cubic structures. The issue of phase segregation, inherent to the MgZnO alloy system, was investigated via selective resonant Raman scattering and will be presented in chapter 4.

Additionally, the investigation of UV luminescent properties of ZnO and MgZnO alloy films has become a research focus in this dissertation. In view of the potential device application, ZnO and $Mg_xZn_{1-x}O$ alloy films should be of a high optical quality and capable to luminescence efficiently in the UV region. Unfortunately, the as-grown ZnO films usually contain intrinsic defects and impurities which can diminish the UV luminescent properties of these films. In an effort to achieve the enhanced UV-PL from the ZnO and alloy films and understand the types and nature of the defects present in those films, we performed post growth annealing studies under controlled environments, and will be covered in chapter 5 and 6. Chapter 7 will provide a brief summary of the results for this research work.

1.6 Conclusion

In this chapter, we have reviewed on the optical properties of the wide bandgap semiconductor materials, particularly focusing on ZnO and $Mg_xZn_{1-x}O$ alloy which are receiving a great of attention for the UV optoelectronics. The possibility of bandgap tuning via the alloying of ZnO and MgO has been discussed. Furthermore, an inherent phase segregation issue that always exists and hinders the fabrication of $Mg_xZn_{1-x}O$ over a wide range of Mg composition has been discussed. An overall focus of the study in this dissertation work has been briefly outlined. Detailed experimental approach, synthesis of the films, their structural and optical characterization will be presented in the later sections.

References

[1] A. K. Sharma, J. Narayan, J. F. Muth, C. W. Teng, C. Jin, A. Kvit, R. M. Kolbas, and O. W. Holland, Applied physics letters **75**, 3327 (1999).

[2] A. Ohtomo, M. Kawasaki, T. Koida, K. Masubuchi, H. Koinuma, Y. Sakurai, Y. Yoshida, T. Yasuda, and Y. Segawa, Applied Physics Letters **72**, 2466 (1998).

[3] Y. Hou, Z. Mei, and X. Du, Journal of Physics D: Applied Physics **47**, 283001 (2014).

[4] D. C. Reynolds, D. C. Look, and B. Jogai, Solid State Communications **99**, 873 (1996).

[5] C.-T. Lee, Materials **3**, 2218 (2010).

[6] A. Becheri, M. Dürr, P. L. Nostro, and P. Baglioni, Journal of Nanoparticle Research **10**, 679 (2008).

[7] Y. Chen, D. M. Bagnall, H.-j. Koh, K.-t. Park, K. Hiraga, Z. Zhu, and T. Yao, Journal of Applied Physics **84**, 3912 (1998).

[8] J. Smith, M. Tokach, R. Goodband, J. Nelssen, and B. Richert, Journal of animal science **75**, 1861 (1997).

[9] J. Huso, *Advanced Optical Alloys: Thin Films and Phonon Properties, Ph.D. Dissertation* (2012).

[10] Ü. Özgür, Y. I. Alivov, C. Liu, A. Teke, M. A. Reshchikov, S. Doğan, V. Avrutin, S.-J. Cho, and H. Morkoç, Journal of applied physics **98**, 041301 (2005).

[11] J. C. Fan, K. M. Sreekanth, Z. Xie, S. L. Chang, and K. V. Rao, Progress in Materials Science **58**, 874 (2013).

[12] C. W. Bunn, Proceedings of the Physical Society **47**, 835 (1935).

[13] E. Mollwo, Z.Angew.Phys. **6**, 257 (1954).

[14] T. C. Damen, S. P. S. Porto, and B. Tell, Physical Review **142**, 570 (1966).

[15] I. T. Drapak, Semiconductors **2**, 624 (1968).

[16] A. E. Tsurkan, N. Fedotova, L. Kicherman, and P. G. Pas' ko, Semicond. Semimetals **6**, 1183 (1975).

[17] R. L. Hoffman, B. J. Norris, and J. F. Wager, Applied Physics Letters **82**, 733 (2003).

[18] O. Madani Ghahfarokhi, K. Chakanga, S. Geissendoerfer, O. Sergeev, K. von Maydell, and C. Agert, Progress in Photovoltaics: Research and Applications **23**, 1340 (2015).

[19] K.-F. Lin, H.-M. Cheng, H.-C. Hsu, and W.-F. Hsieh, Applied physics letters **88**, 263117 (2006).

[20] J. G. Lu, Z. Z. Ye, Y. Z. Zhang, Q. L. Liang, S. Fujita, and Z. L. Wang, Applied physics letters **89**, 023122 (2006).

[21] W. Yang, H. Yang, W. Ding, B. Zhang, L. Zhang, L. Wang, M. Yu, and Q. Zhang, Ultrasonics sonochemistry **33**, 106 (2016).

[22] R. Könenkamp, R. C. Word, and C. Schlegel, Applied Physics Letters **85**, 6004 (2004).

[23] D. Thapa, J. Huso, H. Che, M. Huso, J. L. Morrison, D. Gutierrez, M. G. Norton, and L. Bergman, Applied Physics Letters **102**, 191902 (2013).

[24] E. R. Segnit and A. E. Holland, Journal of the American Ceramic Society **48**, 409 (1965).

[25] S. Choopun, R. D. Vispute, W. Yang, R. P. Sharma, T. Venkatesan, and H. Shen, Applied Physics Letters **80**, 1529 (2002).

[26] H. Morkoç and Ü. Özgür, *Fundamentals, materials and device technology* (Wiley VCH, 2009).

[27] W. Sargent, *Table of periodic properties of the elements* (1980).

[28] C. Zuo, J. Wen, S. Zhu, and C. Zhong, Optical Materials **32**, 595 (2010).

[29] A. Canul, *Analysis of Band-Edge Dynamics in ZnO and MgZnO Thin Films, M.S Thesis* (2015).

[30] A. Alkauskas, M. D. McCluskey, and C. G. Van de Walle, Journal of Applied Physics **119**, 181101 (2016).

[31] V. Khranovskyy, G. R. Yazdi, G. Lashkarev, A. Ulyashin, and R. Yakimova, physica status solidi (a) **205**, 144 (2008).

[32] F. Oba, M. Choi, A. Togo, and I. Tanaka, Science and Technology of Advanced Materials **12**, 034302 (2011).

Chapter 2

Synthesis of ZnO and $Mg_xZn_{1-x}O$ Alloy Films

2.1 Background on sputtering

Sputtering is one of the most common techniques to deposit thin films of a wide range of materials, and has been utilized for many years. Historically, sputtering was first realized by W.R. Grove[1] after he noticed a glowing discharge coating the wall when electrical discharge passed between electrodes. At that time, this phenomenon was considered undesirable since this caused the disintegration of the cathode material. However, after years of intensive investigation of the sputtering phenomenon, it has now become a widely used and well established technique in synthesizing thin films.

The phenomenon of sputtering can be considered as a plasma based vapor deposition technique in which the material to be deposited is physically bombarded with energetic ions, and the ejected materials in the form of vapor can be deposited onto any desired surface.[2] The mechanics of the sputtering process is straightforward and will be discussed in the next section.

Besides the growth of films, sputtering has found application in the cleaning, etching, and surface layer analysis of material samples.[3,4] Furthermore, this technique is simple to perform, versatile, and easily scaleable. Sputtering has made a significant impact in application areas including wear-resistant coating, low friction coatings, corrosion-resistant coating, decorative coating, and coating with specific optical and electrical properties.[5–7]

2.1.1 Mechanism behind the sputtering process

Typically, sputtering involves the bombardment of the material to be deposited (known as a target material) by energetic ions generated in a plasma under vacuum. Upon impact, these energetic ions transfer their momentum and energy to the target

material, resulting in the ejection of some target material in vapor form which will eventually be deposited on the surface of another material, known as a substrate.

As shown in Figure 2.1, the sputtering process is usually carried out in a chamber equipped with a pair of oppositely placed electrodes (cathode and anode). The target material desired to be coated is mounted in front of a cathode while substrates awaiting coating are placed on the anode. Initially, the chamber is evacuated and then backfilled with working gas, typically argon (Ar). Occasionally, other non-reactive gases such as neon or krypton can be used to match the atomic weight of the target material in order to achieve efficient transfer of momentum to the target.

After backfilling the chamber, a strong electric potential is set up between the electrodes. Under such an arrangement, some of the stray electrons will be accelerated towards the cathode and their subsequent collisions with the working gas atoms will result in a cascade of ionization resulting in a glowing discharge commonly known as plasma. The positively charged ions in the plasma will be accelerated towards the cathode striking the target material. If the kinetic energy of these particles exceeds a certain threshold, some of the target material will be knocked off in the form of mostly neutral atoms along with some ions and secondary electrons. Neutral particles will travel across the electric field and plasma region landing on the substrate. As the process continues over time, a uniform thin film of the desired material will be deposited. A schematic of the process has been presented in Figure 2.1.

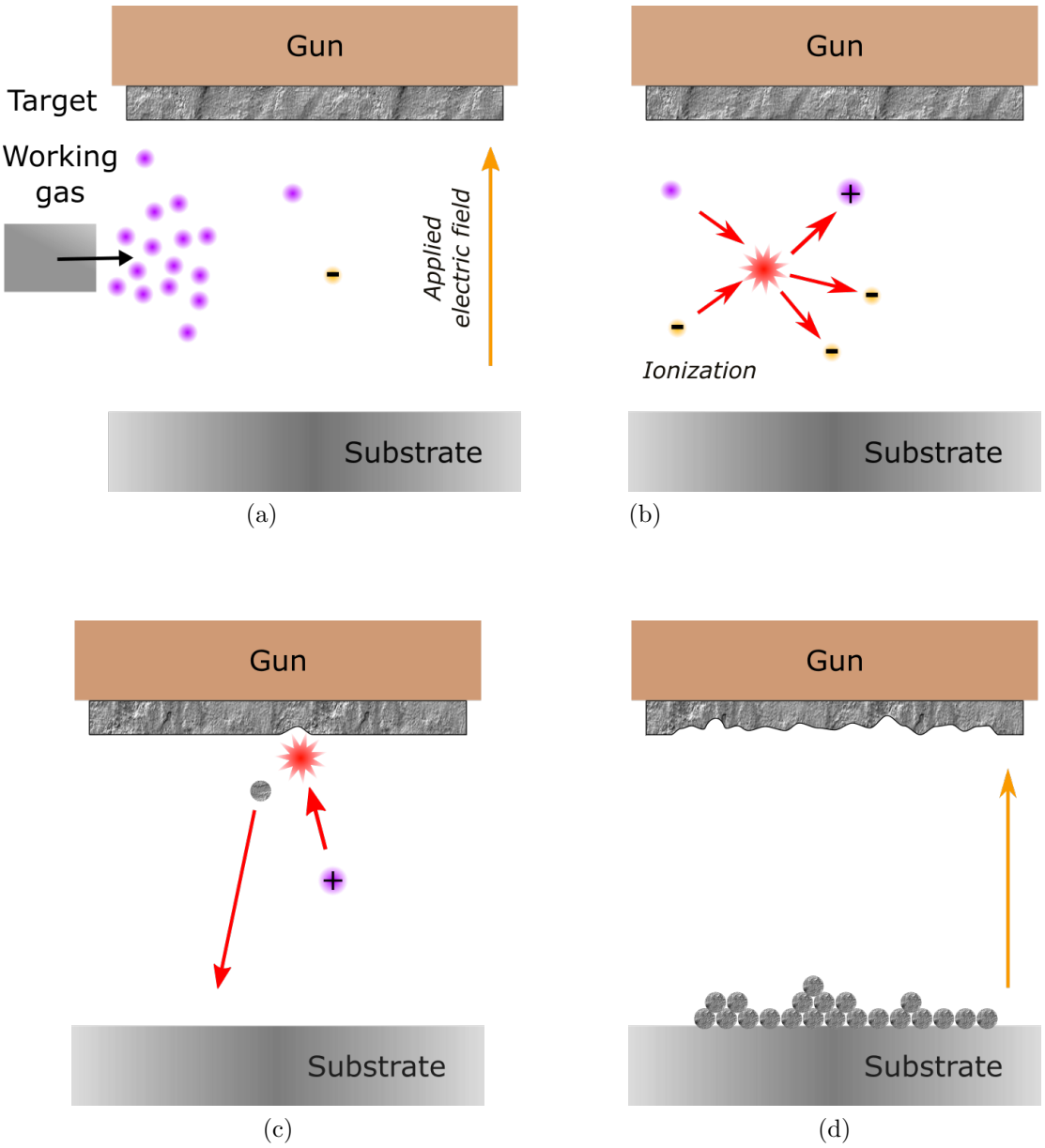

Figure 2.1: *A schematic representing the DC sputtering mechanism for the growth of thin film. (a) Working gas fills the chamber (purple), stray electrons (orange) are accelerated under the applied electric field. (b) These electrons collide with the gas atoms generating more electrons and ions (purple +). (c) Positive ions accelerate towards the target under the effect of the electric field colliding with the target. The material from the target is then ejected. (d) Over time, this process results in a build up of target material on the substrate. Figures are adapted from Ref.* 8

2.1.2 Direct current sputtering and radio frequency sputtering

In the previous section, the discussion was limited to a basic sputtering process in which the target material is bombarded with energetic positive ions generated in the plasma. The plasma itself is generated in the vacuum chamber in the presence of working gas and an electric potential across the cathode and anode. This electric potential can be set in two modes using a direct current (DC) or a radio frequency (RF) power supply. Sputtering performed in each case is referred to as DC sputtering or RF sputtering, respectively.

DC sputtering is preferable compared to RF sputtering since it maximizes the sputtering rate and reduces the growth time of the films. However, this technique has some major limitations. For instance, it can't be employed if one has to use an insulating target during film growth. In this case, the target will not permit the dissipation of positive ions that are incident on it during sputtering. This process would build up a positive charge on the target to a point that it would start to repel any further bombarding positive ions, eventually ceasing the sputtering process. Likewise, arcing is another major concern one typically encounters in reactive DC sputtering.[9,10]

In reactive sputtering, the reactive gas may combine with the metallic target forming an insulating layer such as oxide, carbide, nitride, or any combination depending on the nature of the gas and type of target used.[9] This situation is generally known as target poisoning. In the target-poisoned region, the bombarded positive ions will start to build up until a breakdown occurs in the form of an arc. Arcing can affect the quality and microstructure of the films, stability of the deposition process, and can even cause significant damage to the vacuum chamber and the electronics involved in the sputtering process. Fortunately, in most sputtering systems including the one used in this work, DC power supplies are designed and operated in such a way they can

detect and suppress the arcing issue to a large extent.

As an alternative approach to handle the issues associated with DC sputtering, one can utilize RF sputtering to grow the thin films. As a trade off to this approach, deposition rate will be reduced greatly, making it difficult to scale up the growth process. In RF sputtering, similar to dc sputtering, a high voltage is applied across the electrodes. However, the voltage is oscillating at high frequency (generally at 13.5 MHz). During the first half cycle, the positive ions will move toward the target, and upon impact build up a positive charge on the target surface. During another half cycle, the polarity of the field is reversed, and electrons start accelerating towards the cathode, thereby neutralizing the positive charges built up in the earlier cycle. As such, it should be obvious that RF sputtering effectively leads to sputtering only during each half cycle, which hampers the deposition rate. Additional instruments such as the impedance matching network, and impedance controller unit are required to deliver power to the cathode. Hence, DC sputtering has become the choice of deposition method as long as it can be implemented. We have utilized DC sputtering to grow all the ZnO and $Mg_xZn_{1-x}O$ alloy films investigated in this study.

2.2 Magnetron sputtering system

The basic sputtering system has been known for many years, and has been applied successfully to grow thin films of various materials. However, it is limited by low deposition rates, low ionization efficiencies in the plasma, and high substrate heating effects.[5] These limitations have been overcome by the use of what is known as the magnetron sputtering system. The magnetron sputtering system is quite similar to the basic sputtering system, except that it utilizes a magnetic field configured parallel to the target surface to enhance the plasma during sputtering. This magnetic field is established by placing magnets underneath the target. Furthermore, the magnets are arranged in different configurations with different types of magnetrons suited for

specific applications. In the present work, the magnetic field (B) is configured in the concentric ring pattern near the surface of the target. Additionally, in this configuration, B is perpendicular to an electric field (E) present across the electrodes. A cross-sectional side view of a magnetron arrangement is shown in Figure 2.2(a).

In the presence of an E and B field, motion of any charged particle is governed by the Lorentz force, given by:

$$E = q(\vec{E} + \vec{v} \times \vec{B}) \tag{2.1}$$

With the E and B field arrangements in the magnetron described above, the Lorentz force will guide charge q (of mass m) in a helical path forming closed loops in the region close to the target surface. The radius of the helical path is given by:

$$r = \frac{mv}{qB} \tag{2.2}$$

In the case of electrons produced during sputtering, this radius is on the order of millimeters, and hence electrons will be confined in a region forming a closed loop near the target surface which result in a target erosion profile as shown in Figure 2.2(b). For positive ions of the working gas, this radius becomes much larger than the system dimensions, and these positive ions ultimately remain unaffected by the magnetron configuration. This can be attributed to the large mass of positive ions. Likewise, the particle sputtered off the target, being mostly neutral will not be affected by the field. Coming back to the case of confined electrons in the vicinity of the target, they will have a greater chance of colliding with atoms of the working gas, generating a more stable and intense plasma resulting in an increased deposition rate. Furthermore, this arrangement will allow for growth of the films with the working gas at a low pressure, resulting in an improved film quality.

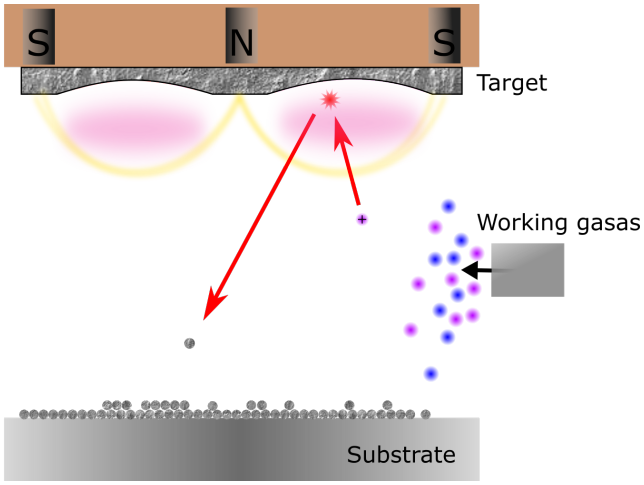

(a)

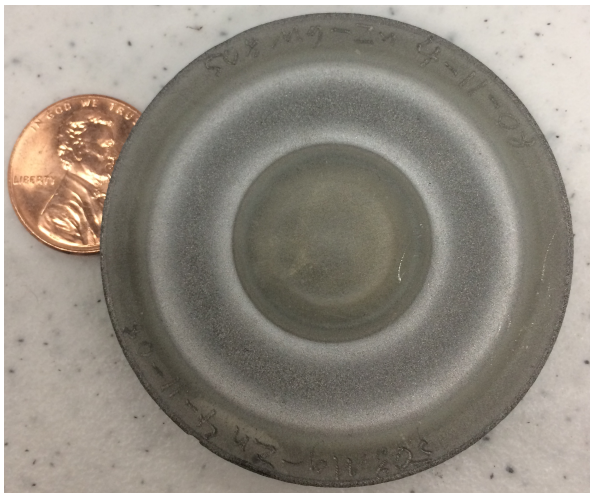

(b)

Figure 2.2: *(a) A cross sectional side view of the magnetron configuration utilized in this work. (b) The electrons generated during sputtering are confined in a magnetic field resulting in a target erosion profile.*

2.3 Sputtering system and instruments used in this work

In this work, thin films were synthesized using the magnetron sputtering system. The magnetron system has dual sputtering guns, and has the capability to operate both in RF and DC modes. However, in this work, only DC sputtering of the target material is carried out using the water-cooled ST20 magnetron sputtering gun AJA international. The basic components of the sputtering system utilized in this work are briefly described as follows:

(a) Sputtering chamber

The magnetron system is contained in a custom sputtering chamber (Figure 2.3). The chamber is sealed using Viton elastomer flanges, copper conflate style flanges, and it is equipped with a Varian V200 turbomolecular pump backed with a Welch model 1402 DuoSeal belt drive mechanical roughing pump.

Pressure inside the chamber is monitored using three types of gauges: a Duniway convection gauge measuring in the range $100 - 10^{-4}$ Torr, a capacitive gauge measuring in the range $10^{-3} - 10^{-4}$ Torr and a Bayard-Alpart style hot cathode ion gauge measuring in the range $10^{-3} - 10^{-10}$ Torr. With the configuration of the chamber described above, the chamber may reach an initial vacuum pressure (i.e. base pressure) of 2.6×10^{-6} Torr. Once this base pressure is achieved, both working and reactive gases, Ar and O_2 are introduced successively, noting their resulting partial pressures. During the growth of the films, the chamber pressure is monitored via the use of a capacitive gauge whose reading is independent of any gas composition. This feature is particularly useful in monitoring the pressure during reactive sputtering which involves different types of gases.

Furthermore, the flow of the gases inside the chamber is regulated through the use of MKS type P4B digital mass flow controllers (MFCs). Their measurement of gas flow is based on the differential heat transfer between temperature-sensing elements attached

to the exterior of the sensing tube. A computer-based flow control application will permit the real-time control of gas with a resolution of 0.07 standard cubic centimeters per minute (sccm) and an accuracy reading of approximately $\pm 1\%$.

According to Dalton's law of partial pressures, the total pressure exerted by a mixture of non-reactive gases is equal to the sum of the partial pressure of the individual gases. Thus, the total pressure inside the chamber during the sputtering process can be described as the sum of the base pressure P_{base}, the partial pressure of Ar, (P_{Ar}), and the partial pressure of O_2 (P_{O_2}) i.e.

$$P_{total} = P_{base} + P_{Ar} + P_{O_2} \tag{2.3}$$

As mentioned above, once base pressure, P_{base}, is attained, Ar and O_2 are introduced successively. The recorded gas pressure for each gas type yields the partial pressure of each gas. This allows for more control of the gas environment, and ensures the repeatability of the material growth.

Figure 2.3: *A photograph of the Magnetron sputtering system that we utilized in our work. On the left is the rack consisting of control electronics, and power generators. On the right is the growth chamber and underneath it is the turbo molecular vacuum pump backed up by the roughing pump.*

(b) Sputtering power source

In this study, ZnO and $Mg_xZn_{1-x}O$ films are fabricated using Zn and Zn-Mg metallic targets and hence, DC Magnetron sputtering is employed to deposit such films. During sputtering, the DC source used is an MDX 500 from Advanced Energy with a maximum power of 500 W with built-in arc suppression circuitry as depicted in Figure 2.4.

(c) Sputtering targets

The sputtering technique allows us to use a wide range of target materials including metal, alloy metal, or ceramic to deposit thin films. Regardless of the type of material used, the target must be pure, dense, and of uniform thickness so as to avoid the destruction of the target or contamination during film growth. Additionally, the sputtering process causes the target to accumulate a large amount of heat, which may crack or damage the target itself. These effects can be minimized by cooling the target or applying certain other measures to avoid catastrophic destruction.

Sputtering targets are commercially available from different manufacturers; however, they are limited to a certain range of materials and composition. As a result, sometimes one might need to make a custom target. In the current study, ZnO and $Mg_xZn_{1-x}O$ films with varying Mg composition are synthesized using Zn and Zn-Mg targets. The utilization of custom built Zn-Mg targets turns out to be more efficient in realizing $Mg_xZn_{1-x}O$ of a desired composition. For consistency, a custom Zn metallic has been used to grow ZnO film. In order to create such targets, Zn powder and Zn-Mg powders mixed in appropriate proportions are pressed in a 2 inch die at 45,000 lbs ram force for 24 hours utilizing a Carver hydraulic press. With the use of such targets, it becomes possible to control the Mg composition of $Mg_xZn_{1-x}O$ films. Such targets might have certain limitations. For example, they may have lower densities and some internal flaws when compared to commercial targets. Hence, lower power should be used in sputtering these targets.

(d) Heating arrangements of the substrates

During the growth of ZnO and $Mg_xZn_{1-x}O$ films in this study, the substrates are heated and maintained at 250 °C using a custom-constructed temperature controller and a custom built stainless steel strip heater from Watlow, and as shown in Figure 2.5 (a) and (b). The controller, which is based around a Yokogawa UT-150 PID controller, allows us to maintain the temperature of the substrate at the desired value between room temperature and 780 °C with tight control. This enables the repeatability of the growth conditions of the films.

Figure 2.4: *A power generator, model MDX 500, used for DC sputtering of ZnO and $Mg_xZn_{1-x}O$ films. This power generator can supply power up to 500 W, and has built in arc suppression circuitry.*

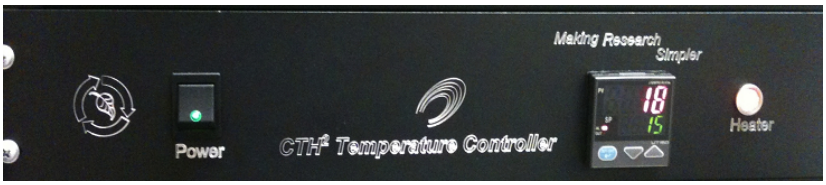

(a)

(b)

Figure 2.5: *(a) A custom built temperature controller based around a Yokogawa UT-150 PID controller. This system is able to control the substrate temperature at the desired value between room temperature and 780 °C.(b) A Watlow stainless steel heater used in our work, capable of heating our substrate to 780 °C .*

(e) Substrates

Typically, substrates are chosen in such a way that they have a similar lattice structure and lattice parameter with the material being deposited. This is a crucial step in synthesizing epitaxial films. However, this is is not always possible, and a buffer layer can be introduced to act as a template for the film to be synthesized. As another consideration, the substrates are expected to not interfere with spectroscopic and other analyzing techniques employed to investigate the thin film properties. Particularly, this becomes an issue if the elimination of the background signal from the substrates is not straightforward. In the present study, ZnO and $Mg_xZn_{1-x}O$ films are synthesized on sapphire (Al_2O_3), quartz (SiO_2) and calcium fluoride (CaF_2). There have been several previous reports on the growth of such films on sapphire substrates, while there are only a few reports on CaF_2. The lattice mismatch between ZnO and CaF_2 is 15.8%-slightly smaller compared to the lattice mismatch between ZnO and sapphire which is about 18.4%.[11] As such, slightly improved qualities of the films are expected using the CaF_2 substrates. However, films synthesized on CaF_2 substrates are limited to further post treatment. For example, annealing the films above 800 °C, CaF_2 substrates appear to change their optical properties, turning from the initial transparent substrate to being a more milky color. As will be seen later in the chapter 5, when post annealing treatment becomes important, films grown on sapphire substrates are preferred.

Additionally, the main advantage of using sapphire, quartz and calcium fluoride as a substrate arises from their UV compatibility. These substrate materials are transparent in a wide range of UV spectral range due to their large bandgap values $\sim$ 8-12 eV and thus will not interfere while performing optical measurements.

2.4 Analytical tools for the characterization of the films

(a) Scanning electron microscopy (SEM)

SEM is a non-destructive method used for surface analysis. Similar to an optical

microscope which uses visible light reflected from a sample surface, SEM uses a different form of radiation, an electron beam. Since the wavelength of the electron is smaller than visible light, the resolution in SEM is therefore much higher, up to 750,000X.[12] When the electron beam bombards the sample, the beam interacts inelastically with atoms in the sample, resulting in secondary electrons, X-rays, and Auger electrons. The secondary electrons mostly contain information regarding the surface morphology. These electrons are generated throughout the primary beam path. However, the electrons can only escape from the surface, and down to 10 nm. Readily interpretable images can be produced by capturing the secondary electrons with an appropriate detector.

Compared to optical microscopes, SEM provides a large depth of field which allows focusing across a large distance with varying depths. This will help in achieving well resolved details of the surface features even if it is rough. Large magnification, small signaling depth and a large depth of field all make SEM ideal for surface imaging, and has been used to study the surface morphology of our sputtered films.

While obtaining images of insulating material, charges start accumulating on the surface. These charges may heat up the sample and eventually build up enough charge to distort the image. In extreme cases, the built up charge can deflect the primary electron beam away from the sample, and into the walls of the SEM chamber.

In an effort to reduce the charging effect, the energy of the beam should be reduced. However, the best way to prevent charging is to coat the sample with some conducting material. While coating, the thickness of the coating material must be carefully controlled: if it becomes too thin, it may not dissipate the charge; and if it is too thick, it can hinder the escaping of secondary electrons from the surface which results in a weak image.

(b) Energy dispersive X-ray spectroscopy (EDS):

Energy dispersive X-ray spectroscopy (EDS) is a non-destructive microanalysis

technique, and can be used in conjunction with SEM to determine the presence and relative abundance of the constituent elements of a sample. When an energetic electron beam strikes the sample, X-ray photons are produced, and collected via an EDS detector placed near the sample. Since the energy of these emitted photons is the characteristic of the parent element, the collected X-ray signal will yield information about the chemical composition of the sample.

The emission process behind the X-ray signal from the specimen surface upon bombardment with an energetic beam can be better understood in terms of the Bohr model, shown in figure 2.6. Accordingly, when a focused electron beam impinges on the sample, it may collide with electrons in the inner shell and eject the electrons from the atom. For example, if the energy of the primary electron beam is slightly greater than the binding energy of the K-shell electron (inner most electron), this bound electron will be ejected, leaving a hole behind. Subsequently, the electrons from the next higher levels (L or M) will jump into the K-shell, filling in the vacancy, resulting in X-ray photons. If an electron jumps from the L-shell to the K-shell, the emitted X-ray is called K_α while if an M-shell electron fills the vacancy, the corresponding X-ray emission is designated as K_β. The photon energies resulting from such transition are characteristic of a particular atom, and thus these photon energies can be used to identify the elements that compose the sample.

The energy position of the peak yields the information about the type of element present, while the intensity of the peak will reveal the relative abundance of the element in the sample. For an illustration, a representative EDS spectrum of our MgZnO alloy film is shown in figure 2.7. Important peaks corresponding to the different elements have been labeled. To identify the chemical composition of the sample, knowledge regarding the elements composing the sample, and a good library of reference spectra is needed. Usually, standard analytical software such as NSS is used, which automatically identifies the peak for each element, and also provides the relative concentration of each

element in the sample. In certain cases the X-ray energies may overlap. For example the K line of sodium (1.04 keV) overlaps with the L line of Zn (1.00 keV). In these cases one must resort to an alternative method for composition analysis. However, in the present cases, no relevant X-ray peaks overlap so this additional consideration does not need to be considered further.

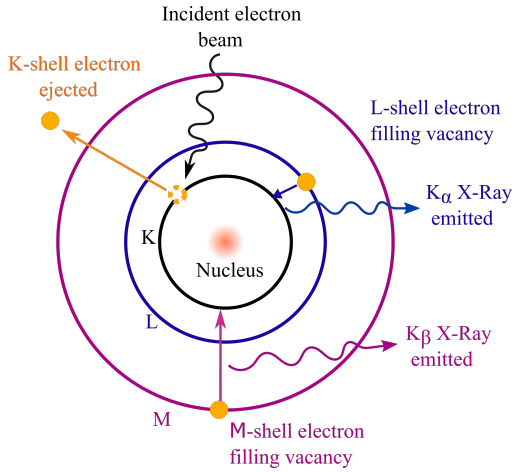

Figure 2.6: *Schematic illustration of X-ray emission lines using Bohr model of an atom. An electron vacancy is created in the inner K shell when primary beam of electrons strike the sample. The electrons from the higher shells (L or M) fill the vacancy and the amount of energy equal to such transition will be released in the form of X-rays.*

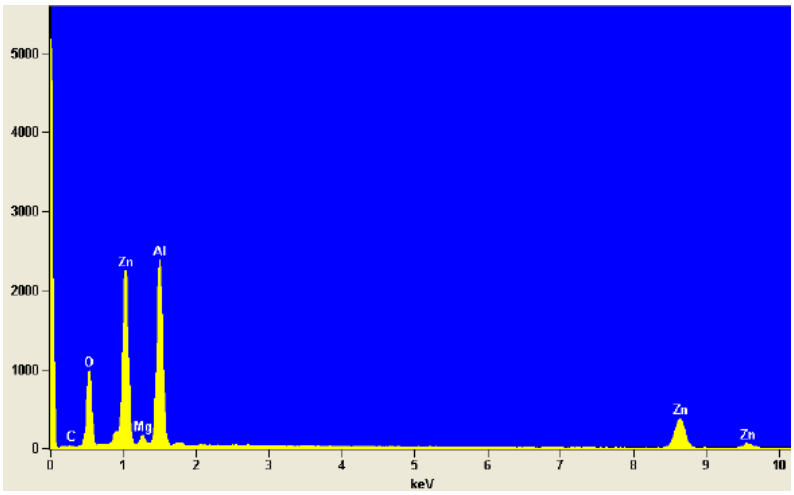

Figure 2.7: *A typical spectrum for an EDS scan of MgZnO film. Spectral peak for Al arises from the sapphire substrate.*

(c) X-ray diffraction

X-ray diffraction (XRD) is a well-known non-destructive technique, and has been commonly used to study the crystalline quality of materials. A basis for XRD lies on the fact that a crystalline material consists of periodic arrays of atoms. These arrangements of atoms can be considered as a set of evenly spaced atomic planes. As the spacing between the atomic planes is on the order of the wavelength of X-rays, a crystal can scatter the X-ray beam.

In a simplistic picture, we can think of each atomic plane as a partially transparent mirror. Hence, when the crystal is being irradiated with X-rays, it is convenient to think of them as being reflected from the atomic planes as shown in Figure 2.8. Any of the two diffracted beams from the adjacent atoms will interfere constructively or destructively depending on their phase. If the path difference between these reflected beams is an integral multiple of wavelength, they will be in phase and interfere constructively. The general equation that governs this requirement is known as Bragg's law, and can be written as:

$$n\lambda = 2dsin\theta \tag{2.4}$$

Where λ is the wavelength of the X-ray beam, d is the spacing between the atomic planes, θ is the scattering angle and n is an integer that indicates the order of reflection.

From Bragg's law it is obvious that for a given value of λ, a crystal with different atomic spacing will produce in-phase scattering at a different value of theta. Experimentally, XRD spectra of a given sample are obtained by detecting the intensity of the reflected beam as function of the scattering angle over a wide range of angles. Based on the d-spacing value of the specimen, the XRD spectra will yield a diffraction peak at a specific angle. By comparing the position of the detected diffraction peak with the standard reference database, the crystal structure of the sample can be identified. When a sample exhibits poor crystalline quality, it might need longer time on collecting the data at each angle and small step size of scan to achieve increase signal-noise ratio

and better resolution.

In this study, XRD measurements on our samples have been carried out utilizing X-ray powder diffractometer where the sample is treated as an ensemble of randomly orientated crystallites. In such randomly orientated crystallites, all lattice planes for each given type of crystal can produce diffraction pattern at specific angles which would allow us to identify the crystal structure of the samples. In this study, XRD has been found extremely useful while finding crystal quality of the ZnO and MgZnO alloy films. Additionally, it has been used to study the structural inhomogeneity of the MgZnO films in conjunction with other technique. This will be presented later in chapter in four in detail.

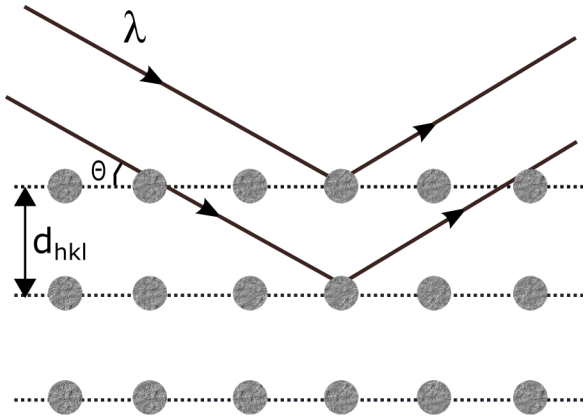

Figure 2.8: *A schematic illustrating for the diffraction of X-rays by the atomic planes in the crystal. If the path difference between the diffracted beams is integral multiple of wavelength, the diffracted beams interfere constructively, and this condition is governed by Bragg's law.*

2.5 Conclusion

The basic theory and instrumentation involved in reactive sputtering utilized to synthesize ZnO and MgZnO thin films have been discussed in this chapter. This growth technique is considered relatively simple and straightforward, and has been

widely used in research laboratories and industrial volume production lines. Some important aspects for the growth of the films such as synthesis of the sputtering target, gas environments, and substrate requirements for the growth of the films have been discussed.

Additionally, a brief introduction and a basic explanation of the material characterization techniques including EDS, SEM and XRD utilized in this study have been presented.

References

[1] W. R. Grove, Philosophical Transactions of the Royal Society of London **142**, 87 (1852).

[2] D. M. Mattox, Metal Finishing **97**, 410 (1999).

[3] P. Cools, N. D. Geyter, E. Vanderleyden, P. Dubruel, and R. Morent, Plasma Chemistry and Plasma Processing **34**, 917 (2014).

[4] H. Kudo, E. Yoshida, and T. Ishihara, Japanese journal of applied physics **32**, L650 (1993).

[5] P. J. Kelly and R. D. Arnell, Vacuum **56**, 159 (2000).

[6] M.-H. Lee, C.-C. Shih, J.-S. Chen, W.-M. Huang, F.-Y. Gan, Y.-C. Shih, C. X. Qiu, and I.-S. Shih, in *SID Symposium Digest of Technical Papers* (Wiley Online Library, 2009), vol. 40, pp. 191–193.

[7] H. Nanto, T. Minami, S. Shooji, and S. Takata, Journal of applied physics **55**, 1029 (1984).

[8] J. Huso, *Advanced Optical Alloys: Thin Films and Phonon Properties, Ph.D. Dissertation* (2012).

[9] J.-W. Lee, S.-K. Tien, and Y.-C. Kuo, Journal of electronic materials **34**, 1484 (2005).

[10] A. Anders, Thin Solid Films **502**, 22 (2006).

[11] H. J. Ko, Y. F. Chen, J. M. Ko, T. Hanada, Z. Zhu, T. Fukuda, and T. Yao, Journal of crystal growth **207**, 87 (1999).

[12] B. L. Gabriel, *SEM: A user's manual for materials science* (American Society for Metals, 1985).

Chapter 3

Characterization Methods: Optical Spectroscopic Techniques

3.1 Spectroscopic techniques

To successfully realize the device applications of semiconductor materials, it is crucial to determine their material and optical properties. In investigating these properties, several characterization techniques have been utilized. Among different characterization methods, optical spectroscopic techniques have turned out to offer distinct advantages such as the ability to acquire a significant amount of information in a non-contact and non-destructive mode. These features are well suited for production lines, and to examine finished products. Additionally, since the optical spectroscopic technique utilizes electromagnetic radiation, by manipulating the light beam, the specimen can be probed to give two- or three-dimensional maps of its properties.[1]

In our work, the spectroscopic techniques: photoluminescence, Raman scattering and transmission have been extensively utilized. A brief discussion and practical means of performing each of these techniques will be presented in this chapter.

3.2 Photoluminescence spectroscopy

Photoluminescence (PL) can be defined as the emission of light from a material under optical excitation. Since the invention of the laser in 1960, PL spectroscopy has been extensively utilized as a characterization tool in the study of semiconductor materials.[2–5] It involves thorough analysis of the energy distribution of photons emitted after optical excitation. This energy distribution is then analyzed to determine material properties such as defect species, defect energy levels, bandgap, etc.

PL spectroscopy is simple, versatile, and a non-destructive technique, offering distinct advantages over other spectroscopic techniques. In PL measurements, the sample does not require any particular handling, preparation, or environmental control. Since

the sample is optically excited, electrical contacts and junctions are unnecessary. Likewise, it is very sensitive, and enables the detection of chemical species even present in the sample at low density. Additionally, a small amount of the material is sufficient to perform PL measurements.

3.3 Mechanisms of photoluminescence

In the PL process, light emission occurs due to radiative recombination[6,7] which can be further understood by considering the band nature of semiconductors. Every semiconductor material has a valence and conduction band. The two bands are separated by a certain energy range referred to as the bandgap (Eg). Typically, electrons reside in the valence band, which is energetically the lowest state. When light of sufficient energy is incident on the material, electrons make a transition to the CB. This state of the crystal not being favorable, the excited electrons relax back to the ground state, emitting photons. This process of light emission can effectively take place in direct bandgap semiconductor materials. GaN, ZnO and their alloy materials are some of the common examples of direct bandgap materials.[8,9]

There are several radiative recombination routes that will lead to light emission after optical excitation, and some of the basic routes have been depicted in Figure 3.1. Below a brief discussion of these basic routes has been presented:

- Band to band recombination: This involves the recombination of electrons in the conduction band and holes in the valence band (process 3 in Fig. 3.1) resulting an emission at energy equal to the bandgap, E_g.

- Free exciton emission: An electron and a hole residing in the CB and VB respectively may become bound via attractive coulomb interaction to form a bound

exciton. An exciton energy level associated with the exciton will be created at an energy lying slightly below the CB. Electrons and holes forming excitons will recombine radiatively (process 4 in Fig.3.1) emitting photons, and the resulting light is referred to as excitonic emission. The energy of the excitonic emission, E_{ex}, is given by:

$$E_{ex} = E_g - E_b \tag{3.1}$$

Where E_b is the binding energy of the free exciton. The binding energy can be estimated using the Bohr hydrogen model, and is given by:

$$E_b = \frac{m^* e^4}{32\pi^2 \varepsilon^2 \hbar^2} \tag{3.2}$$

Where ε is the permittivity of the semiconductor material and m^* is the reduced effective mass of the electron and hole.

- Bound exciton emission: Excitons may become bound with a donor, or an acceptor forming a bound exciton complex. The energy of emission as a result of bound exciton recombination, E_{BX}, is given by:

$$E_{BX} = E_{ex} - E_{bBX} = E_g - E_b - E_{bBX} \tag{3.3}$$

Where E_{bBX} refers to the binding energy of the bound exciton.

Among different types of recombination routes discussed here, light emitted from the free excitonic emission is the most desirable one as far as efficiency is concerned. With the presence of the excitonic level, electrons from the conduction band drop out from the conduction band in to the excitonic level. While residing in this level, electrons are much less likely to participate in crystal vibration or any other interaction. Rather, these electrons will relax back to the valence band and combine with the holes resulting in an efficient emission of light. In the case of ZnO and $Mg_xZn_{1-x}O$ alloy materials,

the large excitonic binding energy makes them excellent emitters potentially useful in device applications.

3.4 Effect of bandgap engineering on PL

As discussed in chapter 1, alloying of semiconductors is a key technique in realizing new bandgaps that are not provided by naturally occurring semiconductors. Furthermore, a tunable band-edge emission is expected via such alloying process. In earlier work by Morrison et al.[10], the PL emission has been reported to exhibit the blue shift $\sim$ 0.25 eV for a Mg composition of 30 at.% in $Mg_xZn_{1-x}O$ nanocrystal. As will be discussed in 4, the current study has established the bandgap modulation spanning in the range $\sim$ 3.30 to 5.85 eV for Mg composition in the range 0 to 78 at.%. However, regarding the light emission properties of alloy films, an extensive study for $Mg_{0.17}Zn_{0.83}O$ film has been carried out, and will be presented in chapter 6.

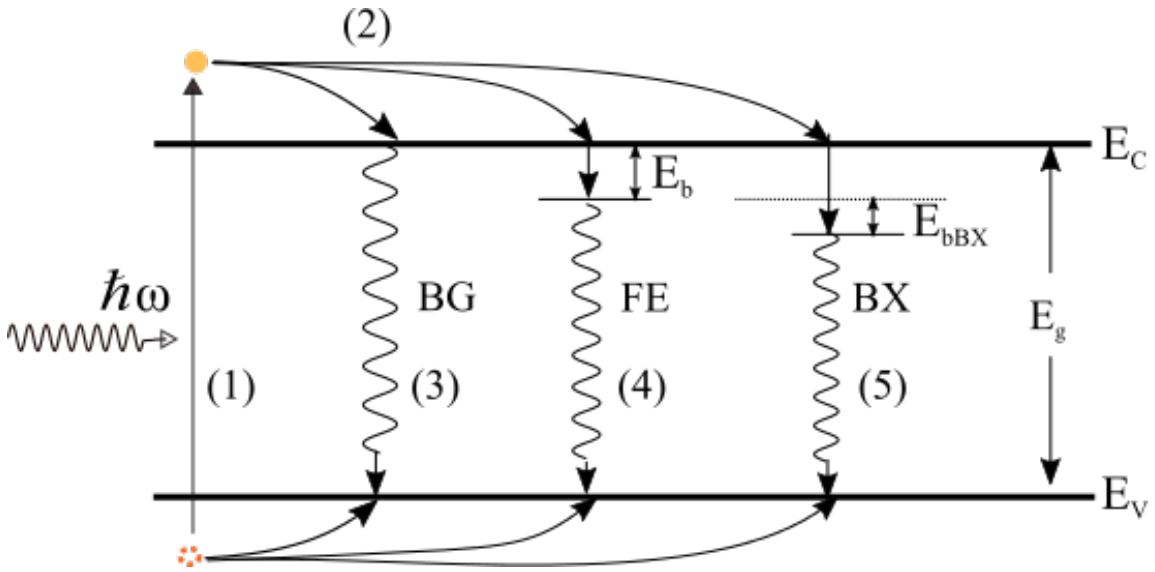

Figure 3.1: *Schematic representing potential routes for photoluminescence in a direct bandgap semiconductor. (1) The incident laser light of energy, $\hbar\omega$, excites electrons from the valence band to the conduction band, leaving a hole in the valence band. (2) The electron thermalizes to the lowest energy state of the conduction band, and then will recombine radiatively with the hole in the valence band in one of the following ways: (3) bandgap recombination, (4) free exciton emission, or (5) bound exciton emission.*

3.5 Instrumentation for PL spectroscopy

A number of custom built spectroscopes have been described in the literature for the PL measurements. In the current study, the custom built micro-Raman and PL system of model Jobin Yvon/Horiba T64000 has been utilized (Figure 3.2). This system is optimized for UV spectroscopy and is capable of probing a spot size less than a $1\mu m$. The laser light used as excitation sources are a Kimmon He-Cd laser operating at 325 nm (3.8eV), and a Lexel SHG frequency doubled argon ion laser operating at 244 nm (5.1eV): both lasers operate in continuous wave mode. The Lexel laser has a beam diameter of 0.8 mm, and a tunable output power up to 100 mW while the Kimmon laser has a beam diameter of 1.2 mm and output power of 50 mW.

The optical system has been equipped with a triple monochromator, confocal microscope and CCD for photon detection. The gratings used for the spectrometer and premonochromator are 2400 lines/mm and 1800 lines/mm respectively. Such a combination provides a reasonable compromise between resolution and range. The confocal microscope increases spatial and lateral depth resolution. Additionally, the system consists of a UV camera and a TV screen, enabling a view of the area being sampled as well as the laser spot on the sample.

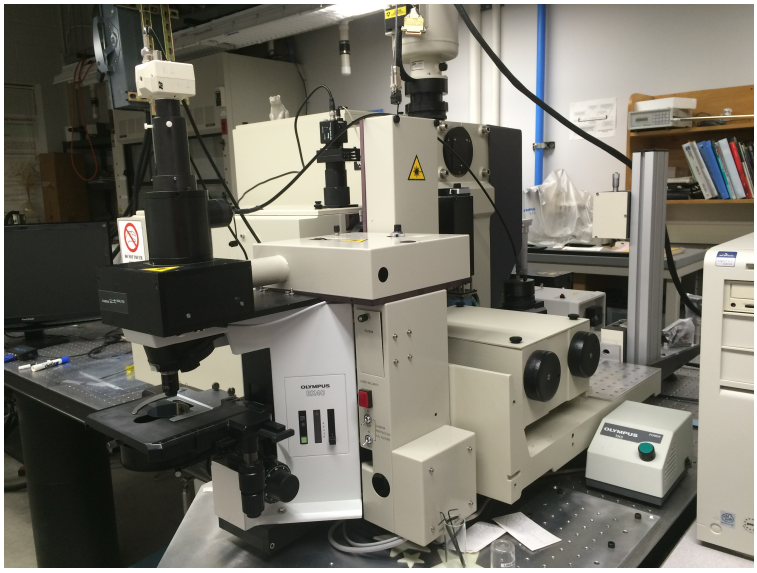

(a)

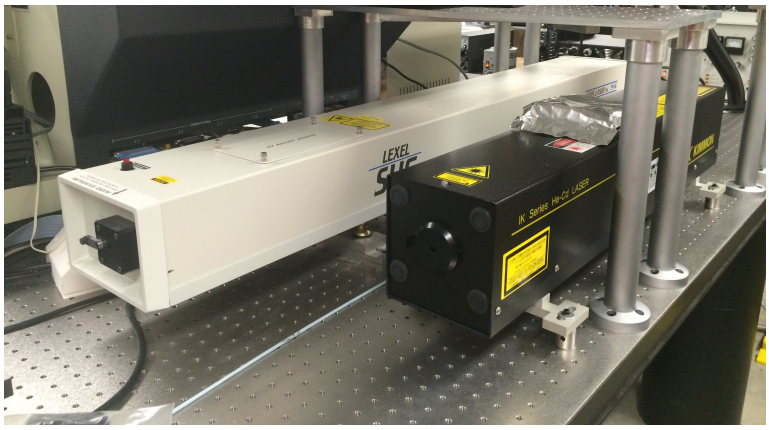

(b)

Figure 3.2: *A photograph of the instrumentation used for the Raman and PL measurements (a) The Jobin Yvon/Horiba T 64000 photoluminescence/Raman system (b) The Kimmon He-Cd laser operating at 325 nm (3.8 eV) wavelength (on the right) and a Lexel SHG frequency doubled argon ion laser of wavelength 244 nm (5.1 eV).*

3.6 PL measurements at low temperatures

Low temperature PL measurements are effective and powerful in examining the optical properties of semiconductors. With such measurements, one can examine the presence of defects, measure the bandgap, and determine the overall crystal quality of the semiconductors. When the temperature is sufficiently low, optically excited carriers are trapped at the binding centers (such as donor and acceptor centers). If these carriers recombine radiatively, the energy of the emitted light yields the energy of the defect or impurity level. Various recombination routes, such as free exciton emission and excitons bound to impurities, can be resolved and systematically identified. Additionally, an investigation of optical properties of semiconductors at low temperature can be extremely useful in fabrication of devices that are expected to operate at cryogenic temperatures.

Figure 3.3 shows how well resolved excitonic features could appear in the PL spectra of bulk ZnO[11] collected at liquid nitrogen temperatures; the spectra collected at room temperature and at 180 K are included for comparison. At room temperature, ZnO displays a single emission peak in the UV region. As ZnO is cooled to liquid nitrogen temperatures, the single peak splits into multiple sharp peaks. These sharp peaks are attributed to various excitons and phonon replicas present in the bulk ZnO. More specific and detailed low temperature PL studies for our ZnO and MgZnO films will be presented in chapters 5 and 6.

In our studies, the low temperature PL measurements were performed utilizing an Instec microscopy cell of model HCS600V capable of operating in the temperature range of 77 K to 873 K. This cell is equipped with a glass window which is highly transparent to the light in the UV range, making it ideal for the UV spectroscopic measurements. An experimental set up for low temperature PL measurements is shown in Figure 3.4

As can be seen in Figure 3.4 an Instec stage is attached with an MK1000 temper-

ature controller and Instecs LN2-SYS cooling system, the controller will control the temperature of the stage precisely, and the cooling system allows the fast and accurate cooling of the Instec stage using liquid nitrogen. Additionally, during low temperature measurements, the vacuum environment (about 10^{-2} Torr) was created inside the stage utilizing a Duniway adsorption pump attached to the instec stage.

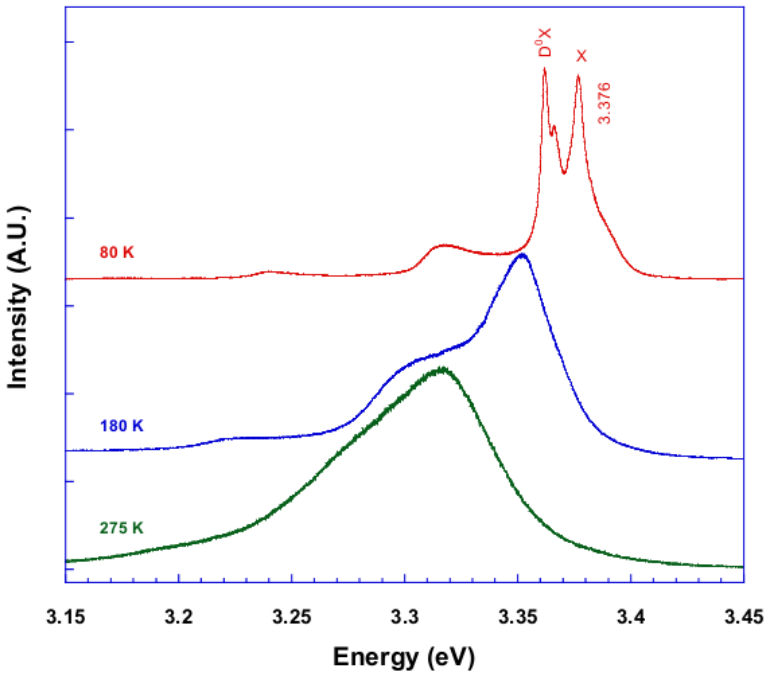

Figure 3.3: *Representative PL spectrum of bulk ZnO crystal at various temperatures. The PL spectrum at room temperature (the lower trace, green) displays a single broad peak. The PL spectrum collected at 180 K (middle trace, blue) starts showing distinct features, but it is still not well resolved. The PL spectrum at 80 K (upper trace, red) displays well resolved excitonic features: D°X∼ 3.362 eV, and free exciton X∼3.376 eV. Smaller peaks that appear at the lower energy position are phonon replicas of the free exciton (taken from ref.* 11*)*

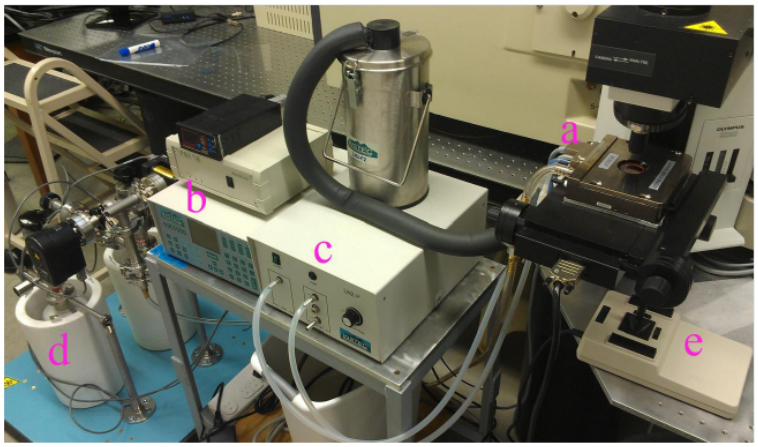

Figure 3.4: *An instrumental set up for the temperature dependent PL measurements performed in this work (a) An Instec microscopy cell of model HCS600V, which can operate in the temperature range 77K to 873K. (b) A programmable high precision temperature controller, model MK1000, which can control temperature in the range -190 °C to 600 °C. (c) Instec's LN2-SYS liquid nitrogen cooling system, capable of cooling the stage fast and accurately and (d) An adsorption pump system that creates a vacuum inside the Instec cell.*

3.7 Overview of Raman spectroscopy

When light is incident upon a material, it can interact with a material in different ways: it may be absorbed or scattered, or may not interact with the material passing straight through it.[12] During scattering, a large fraction of light is elastically scattered, exhibiting the same frequency as that of the incident light. This phenomenon was discovered by Lord Rayleigh in 1871, and is known as Rayleigh scattering. In 1928, Chandrasekhara Venkata Raman, an Indian physicist and his collaborator discovered that when monochromatic light of frequency ν_0 impinges on a material, a small fraction of the scattered light, perhaps 1 photon in 10^6 or 10^7, will be scattered inelastically either towards lower frequencies (Stokes scattering) or higher frequencies (anti-stokes scattering). This phenomenon is known as the Raman effect.

3.8 Basic theory of Raman scattering

The classic theory of Raman scattering is based upon the light scattering event in terms of the oscillating dipole.[13,14] When electromagnetic radiation E is illuminated on the sample, the resulting dipole moment produced in the molecule is given by:

$$P = \alpha E \tag{3.4}$$

Where α is the polarisability of the molecule, and electromagnetic radiation $E = E_0 cos(2\pi\nu_i t)$. Upon substituting for E, Eqn. 3.4 becomes:

$$P = \alpha E_0 cos(2\pi\nu_i t) \tag{3.5}$$

The vibrational modes of atoms in the solid are oscillating in nature, and can be described in terms of normal coordinate, (Q), as:

$$Q = Q_0 cos(2\pi\nu_p t) \tag{3.6}$$

where ν_p is the frequency corresponding to the normal mode of vibration. The oscillation of the atoms may affect the polarizability and it can be expanded in Taylor series as for a small oscillation:

$$\alpha = \alpha_0 + \left(\frac{\partial\alpha}{\partial Q}\right)_0 Q + \text{higher-order terms} \tag{3.7}$$

Plugging the expression for Q from Eq. 3.6 in Eq. 3.7 and then substituting the resulting expression of α in Eq. 3.4 yields the following expression:

$$p = \alpha_0 E_0 cos(2\pi\nu_i t) + \frac{1}{2} E_0 Q_0 \left(\frac{\partial\alpha}{\partial Q}\right)_0 \{cos[2\pi(\nu_i + \nu_p)t] + cos[(2\pi(\nu_i - \nu_p)t]\} \tag{3.8}$$

Examining the last expression, it is obvious that the induced dipole oscillates at three different frequencies. The first term corresponds to an oscillating dipole radiating at incident frequency ν_i, i.e. Rayleigh scattering while the latter two terms represent oscillating dipoles radiating at frequencies $\nu_i + \nu_p$ and $\nu_i - \nu_p$, and thus represent the inelastic Raman process. A schematic representation of the Raman scattering process has been shown in Figure 3.5. Furthermore, the above equation reveals that only certain vibrational modes of a molecule become Raman active if the polarisability changes corresponding to these vibration modes i.e. $\left(\frac{\partial\alpha}{\partial Q}\right) \neq 0$. However, this condition is governed by the symmetry of the crystal being studied. Equation 3.8 reveals that Raman scattering is sensitive to the polarizability and phonon frequency of vibration. These parameters in turn depend on several chemical and physical parameters such as the nature of the atoms involved in the bond, the nature of the bond and the symmetry

of the crystal or molecule under study.[15]

As discussed above, when light interacts with the normal mode of vibration of crystal or molecule, Raman scattering occurs. In a Raman spectrum, a set of frequencies corresponding to the normal modes of vibrations appear shifted from the frequency of incident light (usually the laser light). These shifted frequencies are independent of the frequency of laser light, but are the characteristic of the material giving rise to Raman scattering. Thus, a Raman spectrum can be considered as the fingerprint for the material being studied. Typically, the Raman peaks are narrow and exhibit a Lorentzian shape[15].

In practice, Raman signals are quite weak which is due to the fact that only a very few photons, about 1 in 1,000,000 to 10,000,000, undergo Raman scattering. The probability that a photon will undergo Raman scattering can be written as:[12]

$$I = Kl\alpha^2\omega^4 \tag{3.9}$$

Where K is a constant, and involves quantities such as speed of light, l is the laser power, α is the polarizability of the molecule or crystal being studied, and ω is the frequency of the incident light. As one can see from equation, use of a laser light with a high frequency, as an excitation source during acquisition of Raman spectra, can improve the intensity of the Raman signals.

By convention, spectroscopists normally use wavenumber for the measurements in Raman spectroscopy. The wavenumber is written with units in cm^{-1}, and can be expressed as:

$$\overline{\nu} = \frac{\nu}{c} = \frac{1}{\lambda}(cm^{-1}) \tag{3.10}$$

Where c is the speed of light in cm/s.

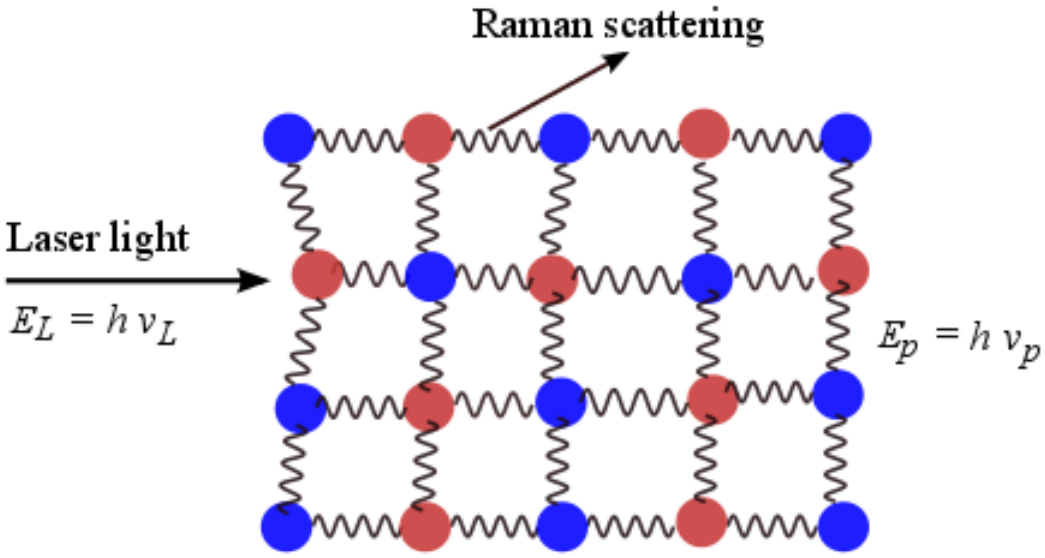

Figure 3.5: *Schematic illustration for the Raman scattering effect in a crystal. Upon excitation with the laser light of energy E_L, vibrational modes known as phonons of energy E_p are created in the crystal, and the rest of the radiant energy, E_s being scattered off the crystal. The conservation of energy gives: E_L=E_p + E_s. The scattered light from the crystal E_s is detected by the Raman detector; which allows the calculation of phonon energy E_p.*

3.9 Instrumentation for Raman spectroscopy

The instrumentation used to perform the Raman scattering experiments in our studies is essentially identical to the one described in section 3.5. The only difference lies in the position of the grating while collecting Raman and PL spectra. While collecting PL spectra, the gratings are required to scan over a wide range of energy (for example a spectrum might cover a range of 2.8 eV to 5.1 eV). In contrast, for Raman spectra the system is required to scan over a much smaller range. Additionally, since the Raman signals are weak, Raman scattering requires much larger acquisition time relative to PL. However, for resonant Raman scattering (discussed in the later section) one might record the signal with less acquisition time. As a further note, for low temperature Raman measurements, the additional instrumentation described in section 3.6 is needed.

3.10 UV-Visible transmission spectroscopy

When material is irradiated with electromagnetic radiation, light-matter interaction results a number of processes. Light may be absorbed, scattered and re-emitted and so forth. Up on excitation of molecules (or atoms) with appropriate photon energy, electronic transition will occur in which the electrons associated with more than one nucleus, the so-called bonding electrons undergo energy level transition. The electron transition in molecules in turns lead to the absorption of photons of incident electromagnetic radiation. However, in some cases depending on photon energy, molecules may exhibit molecular vibration or rotation instead of exhibiting electronic transition. The electronic transition in molecules require high energy and hence UV-Visible part of EM radiation can stimulate such transition. However, the energy difference between the levels associated with vibration and rotation of the molecules is smaller compared to those involved in electronic transition, a longer wavelength of radiation i.e., infrared

and far infrared (or microwave) part of EM radiation may result in vibration and rotational absorption, respectively.

In UV-Visible transmission spectroscopy, samples are irradiated with UV-Visible light and upon excitation electrons from the ground state may be prompted to excited states. In a semiconductor, when the photon energy of incident light becomes sufficient (i.e., equal or greater than the bandgap value), the electrons residing in the valence band may undergo transition to the higher states in the conduction band. On the other hand, if the photon energy of the incident light is less than the bandgap, light will be transmitted through the material. In UV-Visible transmission spectroscopy, one records the amount of light passing through the material relative to the incident light as a function of wavelength and obtains the transmission spectrum, which equivalently provides the information on absorption properties of the material.

Transmission spectroscopy is a complementary technique to photoluminescence spectroscopy (PL). On analyzing the PL emission spectra from the material upon excitation, the spectra will provide information such as exciton energy, defects and doping. But PL does not convey information on bandgap of the material, particularly if the material exhibits excitonic emission and defects. As such, transmission spectroscopy becomes essential in deducing the value of bandgap, an important quantity which determines the electronic properties of the material. Besides this application, the transmission spectra are quite useful in determining the thickness, refractive indices, and Urbach energy of the sample. Hence, transmission spectroscopy in conjunction with PL spectroscopy reveal an extensive picture on optical properties of the semiconductor materials.

3.11 Transmission spectra: bandgap analysis

As mentioned above, when semiconductor material is exposed to light irradiation, the material becomes transparent to photon energies below bandgap while photons

with energies higher than Eg will be absorbed by the semiconductor. A representative transmission spectrum acquired for ZnO bulk is shown in Figure 3.6. In the lower wavelength region, the film appears to be highly transparent while the transmission drops sharply about the bandgap value of the material. Thus, by analyzing the transmission spectrum, one can extract the bandgap value for semiconductor material. Particularly for the films ZnO and $Mg_{1-x}Zn_xO$ alloy films studied in this work, the bandgap has been determined utilizing the transmission spectra via two methods:

(a) Tauc Plot analysis

(b) Derivative method

Since Tauc plot analysis utilizes the absorption spectrum, deduced from the transmission spectrum, it would be wise to discuss the fundamental absorption process in the semiconductor material. This will be presented in the following section.

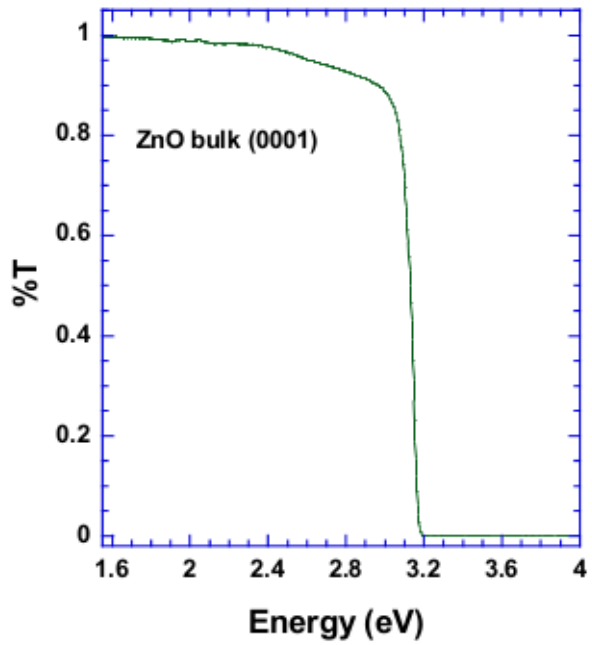

Figure 3.6: *Transmission spectrum of bulk ZnO. This transmission spectrum reveals that the transmission drops sharply around 3.1 eV, and the steep drop is due to the bandgap of ZnO. The methods of extraction of bandgap utilizing the transmission spectra are presented in in sections 3.13 and 3.14.*

3.12 Interband absorption

As shown in Figure 3.7 consider a fundamental absorption process in a semiconductor material upon interaction with photons of energies $h\nu$. Further, for simplicity, let us consider that the lower states are completely filled while the upper states are empty, which is strictly true at 0 K. In the case of direct bandgap semiconductor, all the vertical transition are possible, and the transition probability becomes independent of photon energy. As shown in the Figure 3.7, every initial state E_i is associated with the final state E_f such that:

$$E_f - E_i = h\nu \tag{3.11}$$

In parabolic band,

$$E_f = E_g + \frac{\hbar^2 k^2}{2m_e^*} \tag{3.12}$$

and

$$E_i = -\frac{\hbar^2 k^2}{2m_h^*} \tag{3.13}$$

Hence,

$$h\nu = E_g + \frac{\hbar^2 k^2}{2}\left(\frac{1}{m_e^*} + \frac{1}{m_h^*}\right) \tag{3.14}$$

Next, the density of the states associated with the transition can be given by:

$$N(h\nu)d(h\nu) = \frac{8\pi k^2 dk}{(2\pi)^3} \tag{3.15}$$

Using equation 3.14, equation 3.15 can be further written as:

$$N(h\nu) = \frac{(2m_r)^{\frac{3}{2}}}{2\pi^2\hbar^3}(h\nu - E_g)^{\frac{1}{2}} \tag{3.16}$$

where m_r is the reduced mass of an electron and hole.

Following Ref. 16, the absorption coefficient due to band to band transition can be expressed as:

$$\alpha = \frac{4\pi^2 e^2}{ncm^2\omega} \mid P_i f \mid^2 N(h\nu) \tag{3.17}$$

where $\mid P_i f \mid^2$ is the matrix element of the momentum. Without going further into detail for $\mid P_i f \mid^2$, and simply using its value from ref. 17 and using equation 3.16, equation 3.17 can be written as:

$$\alpha(h\nu) = A^*(h\nu - E_g)^{\frac{1}{2}} \tag{3.18}$$

where

$$A^* \approx \frac{q^2\left(\frac{m_h^* m_e^*}{m_h^* + m_e^*}\right)^{\frac{3}{2}}}{nch^2 m_e^*} \tag{3.19}$$

where n is the index of refraction. Eqn. 3.18, reveals that for $h\nu = E_g$, absorption coefficient(α) becomes zero while $h\nu > E_g$, it varies as $(h\nu - E_g)^{\frac{1}{2}}$. This provides main

basis for the Tauc plot analysis discussed as in the next section.

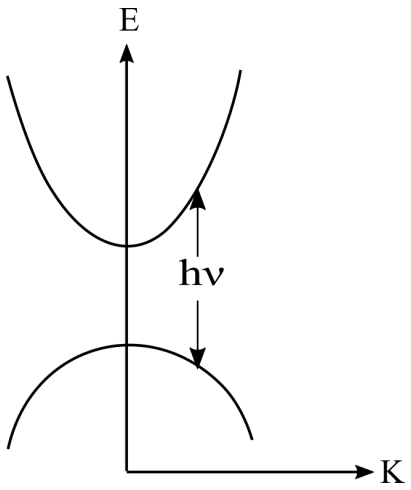

Figure 3.7: *Band to band transition in a direct bandgap semiconductor upon interaction with photons of energies $h\nu$. For a direct bandgap semiconductor, only vertical electronic transitions are allowed, and each energy state in valence band is associated with each energy state in the conduction band*

3.13 Tauc plot analysis and determination of bandgap

Following the quantum mechanical model, Ridley[18] deduced the expression for absorption coefficient associated with inter-band optical absorption processes in direct bandgap semiconductor material, which is slightly deviated from Eqn. 3.18 and is given by:

$$\alpha = C\frac{1}{E\eta_r}(E - E_g)^{\frac{1}{2}} \tag{3.20}$$

where $C = \frac{8}{3}\beta a_H^2 R_H^2 \frac{P_{cv}^2}{2m}\left(\frac{2m_r^*}{\hbar^2}\right)^{\frac{3}{2}}$ is a constant.

Further, above Eqn. 3.20 can be written as:

$$\alpha^2 E^2 \eta_r^2 \propto (E - E_g) \tag{3.21}$$

Furthermore, as will be discussed in the next section, the absorption coefficient can be deduced from the transmission spectra using $\alpha = \frac{-lnT}{t}$.

In accordance with the above relation, a plot of $[(-lnTt^{-1})^2 E^2 \eta_r^2]$ versus energy yields a straight line over the energy range beyond E_g, and the extrapolation of this straight to intersect the energy axis provides the value of bandgap.

Though the method described above is straightforward and provides a reasonable value of the bandgap value for pure semiconductor material, this method has some issues while determining bandgap value of alloy semiconductors or semiconductors with defects and impurities. In such cases, the absorption edge becomes broad which in turn provides an ambiguity in the usual extrapolation of the bandgap via linear fitting. As such this method may not render a good result for bandgap values. As a further note, practically, it is common to assume refractive index η as constant over a spectral region of absorption and hence in Tauc plot analysis, a plot of $[(-lnTt^{-1})^2 E^2]$ versus energy will be obtained. A similar plot has been employed in this work while

applying Tauc plot analysis to ZnO and $Mg_{1-x}Zn_xO$ films and will be presented in chapters 4, 5, and 6.

3.14 Determination of bandgap: the derivative method

In order to overcome the limitations associated with Tauc plot analysis as mentioned earlier, the derivative method can be used in determining the bandgap of semiconductor material. In this method a plot of first order derivative of transmission versus energy will be obtained, and the point of inflection in the plot yields the value of bandgap. This method has been found useful in determining optical bandgap for alloyed film, nanostructures and phase segregated materials.[19] This method of bandgap determination has been thoroughly discussed in Ref. 20, and presented here briefly. Transmission through a film of thickness, t, can be approximated as:

$$T(E) = e^{-C^* \frac{1}{E\eta_r}(E-E_g)^{\frac{1}{2}}} \tag{3.22}$$

where $C_* = Ct^{-1}$. Without going further detail, from Ref. 20 the limiting value of first derivative of transmission with respect to energy when the energy of incident light approaches the bandgap can be written as:

$$\lim_{E \to E_g} \frac{dT}{dE} = -C^* \left(-0 - 0 + 1/0\right) \to -\infty \tag{3.23}$$

Hence on plotting between dT/dE versus energy, a sharp inflection point will be obtained when the incident energy becomes equal to the bandgap value.

3.15 Thickness of the films

While performing transmission measurements in a material in thin film form, practically film configuration during measurements can be considered as depicted in Figure

3.8. As can be seen in the figure, A light beam upon incident normally at the air/film interface will be partially reflected and partially transmitted at the front and back interface of the film. Taking all these reflected and transmitted light, and further considering the the film to be uniform and weakly absorbing, the transmission through the film is given by:[21]

$$T = \frac{16 n_s n^2 x}{(1+n)^2(n+n_s)^2 - 2x[(n^2-1)(n^2-n_s^2)cos(\gamma) + (n-1)^2(n-n_s)^2 x^2} \tag{3.24}$$

where $x = exp(\frac{-4\pi nd}{\lambda})$ and $\gamma = \frac{4\pi nd}{\lambda}$. Light waves from the air-film and film-substrate interfere and hence the transmitted light through the film exhibits the interference pattern as in Figure 3.9. For maxima and minima, the cosine term in the denominator of equation 3.24 equals +1 and -1 respectively.

If n_1 and n_2 are the refractive indices at two maxima (or minima) at λ_1 and λ_2, then the condition for the interference maxima yields:

$$2n_1 d = m_1 \lambda_1 \tag{3.25}$$

$$2n_2 d = m_2 \lambda_2 \tag{3.26}$$

where m_1 and m_2 are integers.

Thus,

$$m_1 - m_2 = M = \frac{2n_1 d}{\lambda_1} - \frac{2n_2 d}{\lambda_2} \tag{3.27}$$

where M is the number of inter-fringes (i.e. number of maxima) in the spectral range of $(\lambda_1 - \lambda_2)$.

Hence,

$$d = \frac{M\lambda_1\lambda_2}{2(n_1\lambda_2 - n_2\lambda_1)}) \tag{3.28}$$

In the transmission spectra shown in figure 3.9, the maxima indicated in the figure are located at $\lambda_1 = 700.5$ nm and $\lambda_2 = 537.2$ nm and $M = 2$. Hence, using above equation 3.28, $d = 926$ nm.

The values of thickness acquired via this method were cross checked with the values measured utilizing an independent method, stylus profilometry, which will be discussed in the next section.

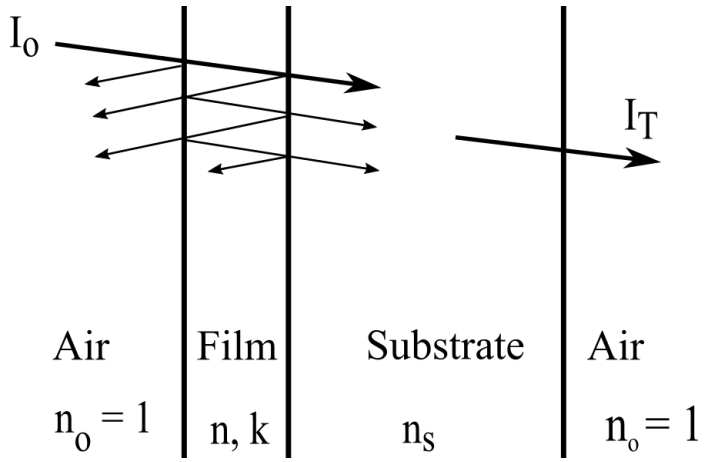

Figure 3.8: *Transmission of a light beam through a weakly absorbing thin film deposited on a transparent semi-infinite substrate. For clear view, the normal incident beams are slightly tilted away from the normal to the surface. Figure adapted from Ref.* 22

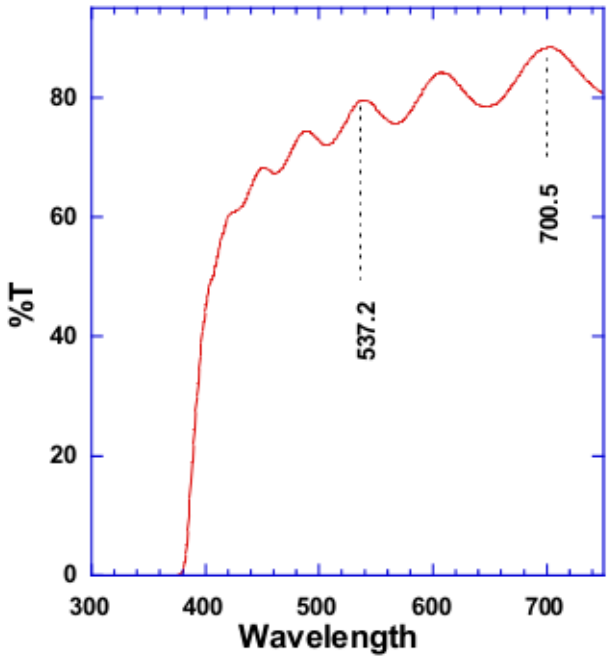

Figure 3.9: *Transmission spectrum of ZnO film deposited on CaF_2 substrate. The transmission spectrum reveals that the transmission drops sharply around 3.20 eV, and the steep drop is due to the bandgap of ZnO. The sinusoidal pattern at the transparent region is due to the thin film interference. The spectral position of two maxima, which are chosen for the film thickness, are indicated by the dotted lines.*

3.16 Stylus profilometry

Stylus profilometry is a straightforward technique to measure the thickness of a film. Typically, a profilometer is equipped with a very small needle like stylus which can move vertically and laterally in contact with the surface of the sample over a certain distance. By monitoring the vertical position of the stylus while it is moved across the sample, one can measure the surface height and the thickness of the sample.

To determine the film thickness via this method, one may need to create a step edge between the film and substrate. Such a step edge can be created by masking a small portion of substrate during the growth of the film. In our studies, small portions of a couple substrates used during the growth of the films were masked by attaching krypton tape. After the completion of film growth, the tape was removed, and cleaned carefully to remove the residue. This results in a sharp edge between the film and substrate. For comparison, the measured values of thickness for a few film samples via both the transmission spectra and profilometry method were tabulated in Table 3.1. As can be seen in the table, the measured values of thickness utilizing both methods agree reasonably. In our studies, we have opted to use the transmission spectra, since this way of finding the thickness is indeed fast, clean, and does not required any additional steps like in the profilometry method.

Table 3.1: Thickness of the films

Thickness of the films	Transmission method	Profilometry method
ZnO film	1062 nm	926 nm
$Mg_{0.65}Zn_{0.45}O$ film	165 nm	151 nm

3.17 Conclusion

This chapter presents a brief discussion on the spectroscopic techniques: Raman, PL and Transmission spectroscopy. Particularly, a physical basis and a practical means of performing each of the spectroscopic techniques have been discussed. Representative spectra acquired utilizing each technique have also been included to indicate the basic semiconductor quantities measured, and how the measurement is made for each technique.

Basic radiative routes for the PL process, a basic theory on Raman scattering has been briefly reviewed. Additionally, two different methods of bandgap determination utilizing the transmission spectra have been discussed. Furthermore, other useful aspect of the transmission spectra, determination of the thickness of the film has been included.

The spectroscopic techniques discussed here will allow us to investigate the material and optical characterization of the ZnO and MgZnO sputtered films, and will be presented in chapters 4, 5 and 6.

References

[1] S. Perkowitz, *Optical characterization of semiconductors: infrared, Raman, and photoluminescence spectroscopy* (Elsevier, 2012).

[2] M. L. W. Thewalt, A. G. Steele, and J. E. Huffman, Applied physics letters **49**, 1444 (1986).

[3] E. Przeździecka, E. Kamińska, K. P. Korona, E. Dynowska, W. Dobrowolski, R. Jakieła, Ł. Kłopotowski, and J. Kossut, Semiconductor science and technology **22**, 10 (2007).

[4] G. Santana-Rodríguez, A. Mejía-Montero, B. M. Monroy-Peláez, M. López-López, Y. L. Casallas-Moreno, M. Ramírez-López, G. Contreras-Puente, and O. de Melo-Pereira, Materials Sciences and Applications **2014**, 267 (2014).

[5] G. D. Gilliland, Materials Science and Engineering: R: Reports **18**, 99 (1997).

[6] H. Kuzmany, *Solid-state spectroscopy: an introduction* (Springer Science & Business Media, 2009).

[7] B. Henderson and G. F. Imbusch, *Optical spectroscopy of inorganic solids*, vol. 44 (Oxford University Press, 2006).

[8] A. Ohtomo, M. Kawasaki, T. Koida, K. Masubuchi, H. Koinuma, Y. Sakurai, Y. Yoshida, T. Yasuda, and Y. Segawa, Applied Physics Letters **72**, 2466 (1998).

[9] A. K. Sharma, J. Narayan, J. F. Muth, C. W. Teng, C. Jin, A. Kvit, R. M. Kolbas, and O. W. Holland, Applied physics letters **75**, 3327 (1999).

[10] J. L. Morrison, J. Huso, H. Hoeck, E. Casey, J. Mitchell, L. Bergman, and M. G. Norton, Journal of Applied Physics **104**, 123519 (2008).

[11] J. Huso, *Advanced Optical Alloys: Thin Films and Phonon Properties, Ph.D. Dissertation* (2012).

[12] E. Smith and G. Dent, *Modern Raman spectroscopy: a practical approach* (John Wiley & Sons, 2013).

[13] D. A. Long, *Raman spectroscopy* (Wiley and Chapman and Hall, 1977).

[14] R. Loudon, in *Proceedings of the Royal Society of London A: Mathematical, Physical and Engineering Sciences* (The Royal Society, 1963), vol. 275, pp. 218–232.

[15] G. Gouadec and P. Colomban, Progress in Crystal Growth and Characterization of Materials **53**, 1 (2007).

[16] J. I. Pankove, *Optical processes in semiconductors* (Dover, New York, 1975).

[17] J. Bardeen, F. Blatt, and L. Hall, in *Proc. of Atlantic city Photoconductivity Conference 1954* (J.Wiley and Chapman and Hall, 1956), p. 146.

[18] B. K. Ridley, *Quantum processes in semiconductors* (Oxford University Press, 2013).

[19] D. Thapa, J. Huso, H. Che, M. Huso, J. L. Morrison, D. Gutierrez, M. G. Norton, and L. Bergman, Applied Physics Letters **102**, 191902 (2013).

[20] H. Che, J. Huso, J. L. Morrison, D. Thapa, M. Huso, W. J. Yeh, M. C. Tarun, M. D. McCluskey, and L. Bergman, Journal of Nanomaterials **2012**, 1 (2012).

[21] J. C. Manifacier, J. Gasiot, and J. P. Fillard, Journal of Physics E: Scientific Instruments **9**, 1002 (1976).

[22] B. Šantić and F. Scholz, Measurement Science and Technology **19**, 105303 (2008).

Chapter 4

Study of the Structural Inhomogeneities Embedded in MgZnO Alloys via Selective Resonant Raman Scattering

4.1 Introduction

In recent years, the $Mg_xZn_{1-x}O$ alloy has attracted considerable attention due to to its advantageous material and optical properties. In particular, the $Mg_xZn_{1-x}O$ system allows for bandgap tunability into the UV range, has deep excitonic energy which makes the alloys optically stable at and above room temperature, and is a relatively environmentally friendly and cost effective material.[1–6] ZnO has the hexagonal wurtzite structure and a bandgap of ~ 3.4 eV, while MgO has the NaCl cubic structure and a bandgap of ~ 7.4 eV.[7,8] $Mg_xZn_{1-x}O$ alloys spanning the UV range of $\sim 3.4 - 6.5$ eV have been realized.[1–3]

The compatible sizes of the Zn and Mg atoms permit solubility for which low Mg composition alloys favor the wurtzite structure while at the high range the alloys crystallize with the cubic structure. However, due to the two different crystal structures of the end members of the $Mg_xZn_{1-x}O$ alloy system, the two oxides do not show complete solid solubility, and an intermediate composition range exists in which an alloy is phase separated into the wurtzite and cubic structures.[1,3,9,10]

As discussed in chapter 1, according to the phase diagram of the ZnO-MgO solid solution, the thermodynamic solubility limit of MgO in ZnO is very small $\sim 4\%$, while that of ZnO in MgO is $\sim 40\%$.[11] MgZnO films grown via pulsed laser deposition were found to exceed the low solubility limit of MgO in ZnO due to the thermodynamic growth conditions, and single phase films with the wurtzite structure of up to $\sim 35\%$ Mg were achieved.[1,12] A similar solubility limit was obtained in the present work via the sputtering growth technique. During the sputtering, the relatively high energy precursor material cools rapidly to the substrate temperature, and due to the lack of

sufficient diffusion, the film crystallizes in a non-equilibrium state resulting in a high MgO solubility limit. On the other hand, the Mg-rich cubic phase has a relatively high solubility limit, and high-quality cubic MgZnO epitaxial films have been realized in order to enable integration with Si technologies.[13] Additionally, in our earlier work, ceramic samples were studied in terms of the thermodynamic conditions required for the formation of the wurtzite and the cubic phases.[14]

The phase segregation phenomenon has been found to also impact the phonon characteristics of the $Mg_xZn_{1-x}O$ alloy system. The LO phonon of ZnO is at $\sim$580 cm^{-1} and that of MgO is $\sim$720 cm^{-1}, and due to the phase segregation, the phonon dispersion is not a continuous function going from one end member of the alloy to the other. Most studies of phonon dynamics of the $Mg_xZn_{1-x}O$ alloy system were carried out via infrared ellipsometry and a few via Raman scattering.[9,10,15–18] A sensitive technique to study the LO behavior and specifically the phase separation properties of the $Mg_xZn_{1-x}O$ system is selective resonant Raman scattering (SRRS).

Generally, in SRRS, one tunes the laser excitation into near resonance with the bandgap of the embedded structure, and thus it is possible to enhance the Raman signal of the domains by many orders of magnitude. This enhancement provides a particular advantage in sensitivity for the segregated minority phase domains which can be in a size regime too small to be detected by X-ray diffraction (XRD). SRRS has been utilized previously, among other studies, in the investigation of semiconductor single quantum dot and quantum wells with sizes of only few nanometers.[19,20] Additionally, the $In_xGa_{1-x}N$ alloy system has been studied via SRRS in order to gain knowledge of the inherent alloy fluctuations resulting from the large size mismatch of its constituents.[21–25]

4.2 Selective resonant Raman scattering (SRRS)

In its general form the Raman scattering intensity I is given by[26]:

$$I(\omega_L) \propto {\omega_s}^4 |\hat{e_S}.R.\hat{e_L}|^2 \left| \sum_{\alpha\beta} \frac{1}{(E_\alpha - \hbar\omega_L)(E_\beta - \hbar\omega_s)} \right|^2 \tag{4.1}$$

where ω_L and ω_s represent the laser excitation and the scattered photon frequency respectively; E_α and E_β are the energies of intermediate crystal states; $\hat{e_S}$ and $\hat{e_L}$ are the scattered and incident polarization vectors; and R is the Raman tensor. The first term in the above equation is due to the dipole transition radiation, the second term represents the Raman selection rules which takes into consideration of crystal symmetry, and the last term leads to resonance effects.[27]

Energy conservation relates ω_L and ω_S to the phonon frequency ω as:

$$\hbar\omega = \hbar\omega_L - \hbar\omega_S \tag{4.2}$$

As is evident from Eqn. 4.1, when the incident laser frequency approaches the energies of the crystal intermediate states, the Raman intensity becomes larger and the signal is said to be resonance-enhanced; an additional enhancement comes from the dipole radiation term. In general, for semiconductors there may be three relevant types of intermediate states: Bloch states which are the conduction-valence bands, exciton states, and in-gap impurity states. Thus, when the laser excitation is in vicinity of the bandgap energy, the denominator in Eqn. 4.1 becomes smaller leading to enhancement in Raman intensity.

4.3 Synthesis of $Mg_xZn_{1-x}O$ alloy films

For this study, eight $Mg_xZn_{1-x}O$ thin films were grown on (111) CaF_2 substrates using reactive DC magnetron sputtering described in chapter 2. The base pressure of the growth chamber was at 10^{-6} Torr. Mg-Zn metallic custom targets with desirable composition were used, and the deposition of the films were carried out in Ar-O_2 environment at a working pressure of 11 mTorr with delivered power of 30 W to the sputtering target. The sputtering duration was typically set for 2 hours and the substrate temperature was maintained at 250 °C during the growth process. Film thickness was measured using the well-known optical interference technique[28] and confirmed via profilometry as discussed in chapter 3. In accordance with the optical interference technique, the film thickness is calculated via the expression:[28]

$$t = \frac{M\lambda_1\lambda_2}{2(n_1\lambda_2 - n_2\lambda_1)} \tag{4.3}$$

where M is the number of maxima or minima in the spectral range of $(\lambda_1 - \lambda_2)$; n_1 and n_2 are the refractive indices at two maxima (or minima) at λ_1 and λ_2, and can be determined via the envelope method described by Manifacier et al.[28] In these calculations, we have used the reported values of refractive indices.[12,29] The alloy compositions were determined by energy dispersive X-ray spectroscopy (EDS). The samples in this study are referred to as 0%, 12%, 30%, 49%, 65% and 78%, reflecting their Mg composition. The crystal structure and quality of the $Mg_xZn_{1-x}O$ films were investigated via X-ray diffraction (XRD), using a Siemens Diffractometer D5000 with the CuKα1 line. The resonant Raman scattering was acquired in a backscattering geometry using the Jobin-Yvon T64000 micro-Raman/photoluminescence system equipped with a CCD detector. The probing spot has a spatial resolution of 1 μm and the spectral resolution of the system is $\sim$ 2 cm^{-1}. The excitation sources were a frequency-doubled Lexel Ar-ion laser operating at 5.1 eV (244 nm) and a Kimmon HeCd laser operating at 3.8

eV (325 nm). The Raman scattering was obtained at room temperature. The transmission measurements were performed using an Agilent Cary-300 transmission system operating in double-beam mode.

CaF_2 was used as substrate due to its wide band gap of 11.8 eV at 298 K.[30,31] Figure 4.1 present the transmission spectra of CaF_2 substrate showing its high transparency over a spectral range of $\sim$ 2-6 eV.

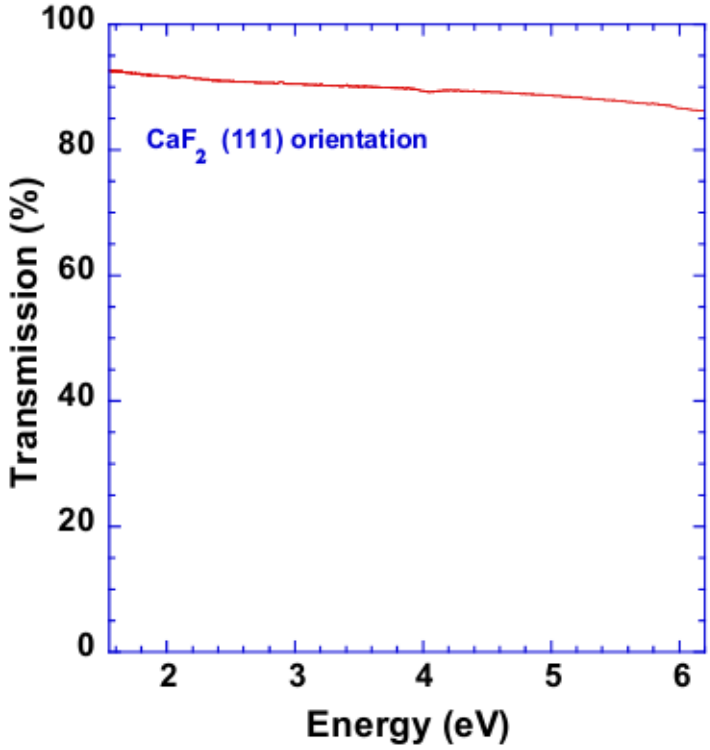

Figure 4.1: *Acquired transmission spectrum of CaF_2 (001) substrate. CaF_2 retains a high transparency to light over a wide range of energy (wavelength) relevant in the current study and hence will not interfere with any optical feature from $Mg_xZn_{1-x}O$ alloy system. Thus, this type of substrate is found to be appropriate for the growth of the films.*

4.4 Results and discussion

4.4.1 Transmission spectra and bandgap analysis of $Mg_xZn_{1-x}O$ films

To investigate the optical properties and bandgap analysis of MgZnO film, transmission spectroscopy has been utilized. Representative transmission spectra are shown in Figure 4.2. As can be seen in the figure, the absorption edges of the films are shifted to higher energy with increasing Mg content in the films, and is attributed to the widening of the bandgap in the alloy films. Additionally, the spectra exhibited bandedge broadening as the Mg is increased. Such an enhanced bandedge broadening with Mg composition is related mainly to morphological structural defects and alloy inhomogeneities. For determining the bandgap, Tauc analysis as described in chapter 3 has been carried out for all films, and presented in Figure 4.3. The Tauc analysis was first utilized by Tauc in 1966 to obtain the optical bandgap of amorphous germanium; now it is among the most used methods for analyzing bandgap of semiconductors.[32,33] This method uses the absorption spectrum to extract the bandgap of the material. As discussed in chapter 3, the absorption coefficient for a direct bandgap semiconductor material is given by:

$$\alpha^2 E^2 = A(E - E_g) \tag{4.4}$$

where A is a constant, E_g is the bandgap, and α is the absorption coefficient.

Thus, the Tauc plot involves a plot of $(\alpha E)^2$ versus the incident photon energy; an extrapolation of the linear region to the energy axis yields a bandgap value. As a note, the values of absorption coefficients required for the Tauc plot analysis can be obtained via the transmission spectra using the relation:

$$T = -lnT/t \tag{4.5}$$

where t is the thickness of the film.

Though this method of finding the bandgap is quite simple and powerful, it may not yield right value of bandgap, particularly when the absorption edge is not sharply defined. The previous studies had suggested that a more appropriate procedure for phase segregated alloys and nanostructures with a relatively broad transmission spectral line is the method that employs the derivative of the transmission with respect to energy, i.e., dT/dE.[34–36] As discussed in chapter three, in this method, as the energy approaches that of the bandgap, the derivative should exhibit a minimum for which its sharpness depends on the characteristics of the transmission spectrum.[34]

Figure 4.4 presents the derivative analyses, and Figure 4.5 summarizes the obtained values of the bandgaps for both methods. The results indicate that for all but two samples, the 61% and 65%, both methods are in good agreement. As will be discussed in the following sections, the 61% and 65% are among the samples that were found via SRRS analysis to exhibit structural inhomogeneity. We suggest that the derivative method in that case is a more straightforward approach for obtaining the majority-phase bandgap value of our alloys.

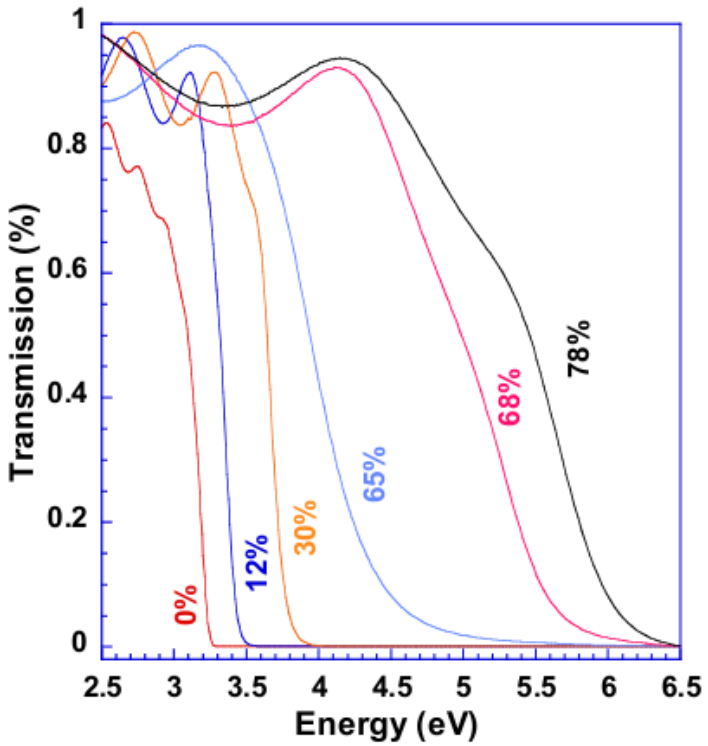

Figure 4.2: *Representative transmission spectra of the $Mg_xZn_{1-x}O$ alloys with Mg content indicated. With increasing Mg composition the band edge moves toward higher energy and simultaneously becomes increasingly broadened. The shifting of bandgap toward higher energy is caused by the widening of bandgap in MgZnO alloy films while the increased broadened bandedge is attributed to the inherent morphological structural defects and alloy inhomogeneities. The additional sinusoidal features at low energies are due to thin film interference.*

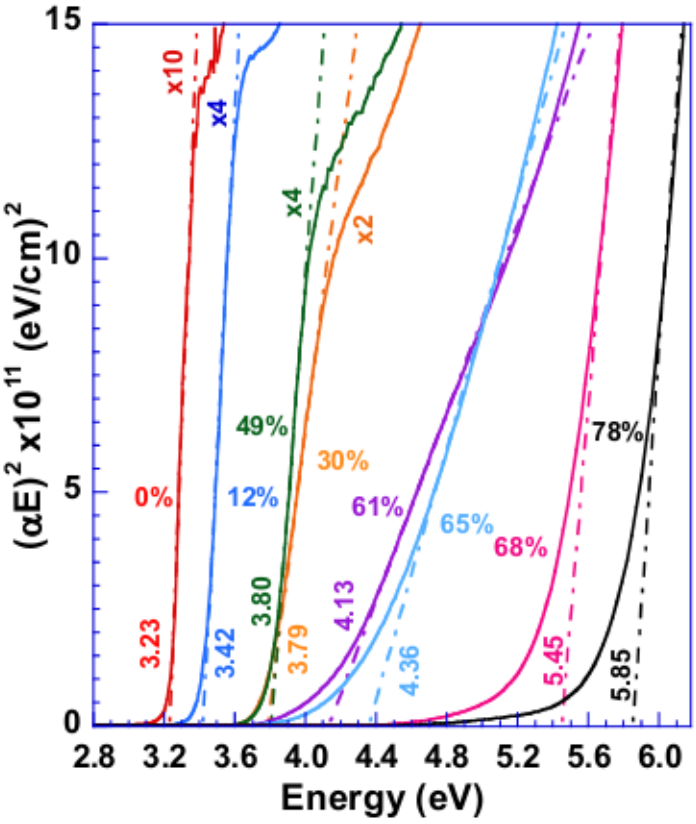

Figure 4.3: *Tauc plot analysis for the determination of bandgap for $Mg_xZn_{1-x}O$ alloys with Mg content indicated. For bandgap determination, Tauc plot method involves the extrapolation of linear region observed in $(\alpha\ E)^2$ versus energy plot, to energy axis, as indicated by by dashed lines in the Figure. For $Mg_xZn_{1-x}O$ with higher Mg composition, Tauc plot method may result a significant uncertainty in the optical gap values due to absence of well defined linear region.*

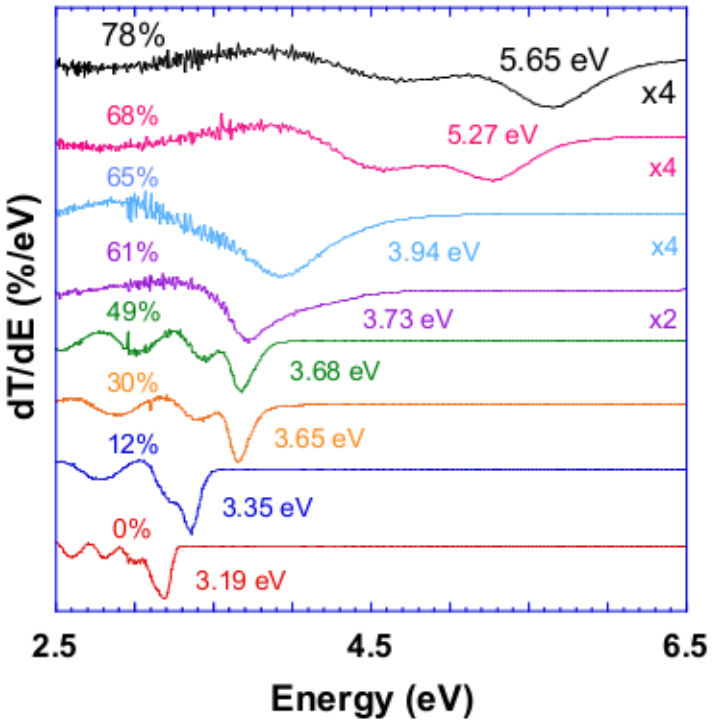

Figure 4.4: *The plots of the derivative of the transmission with respect to energy, dT/dE of the MgZnO alloys. The bandgaps are marked. The main minimum corresponds to the bandgap energy. The additional minima are the film interference patterns.*

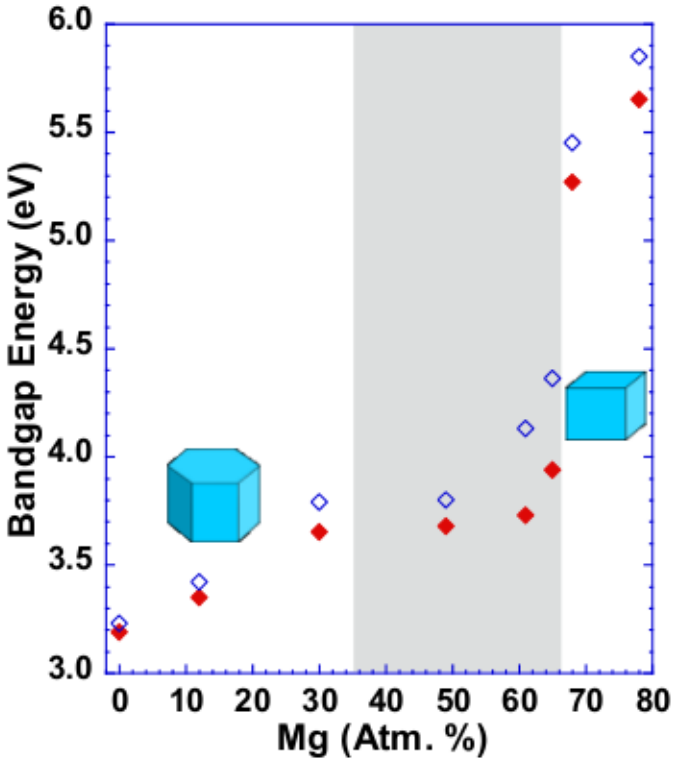

Figure 4.5: *The MgZnO alloy bandgaps as a function of Mg composition. The filled symbols are data points were obtained via the derivative method while the open symbols are data points obtained via Tauc plot analysis. The shaded area presents the phase segregation range obtained from the SRRS analysis.*

4.4.2 Structural characterization of the $Mg_xZn_{1-x}O$ films via XRD

In order to investigate the crystal structure and quality of the $Mg_xZn_{1-x}O$ films, the X-ray diffraction (XRD) was performed using a Siemens Diffractometer D5000 with the CuKα1 line in 2h mode for two different acquisition times of 2 h and 14 h. XRD spectra of several samples are presented in Figure 4.6. The XRD study, for a data acquisition time of 2 h, indicated that the first six samples with Mg composition 0%, 12%, 30%, 49%, 61%, and 65% have diffraction patterns corresponding to the (0002) wurtzite structure. As a note, (0002) XRD peak in all those samples were referenced corresponding to the substrate CaF_2 peak.

In contrast to the $Mg_xZn_{1-x}O$ films with x = 0%, 49%, 61%, 65%, the XRD spectra in Figure 4.6 for last two samples with Mg composition of 68% and 78% display diffraction patterns corresponding to the cubic rock salt structure. In an effort to identify the existence of any phase segregation in all the alloy $Mg_xZn_{1-x}O$ films, a long integration time scan XRD pattern, $\sim$ 14 h, was acquired from all samples. As can be seen in Figure 4.6, the $Mg_{0.65}Zn_{0.35}O$ film which has a wurtzite phase component, was found to also exhibit a weak diffraction peak corresponding to the cubic phase, while the $Mg_{0.68}Zn_{0.32}O$ which is cubic was found to exhibit a very weak diffraction peak assigned to one of the tilted faces of the wurtzite structure. Thus, XRD performed for long integration time provides a direct evidence phase segregation in $Mg_xZn_{1-x}O$ films with x = 65%, 68% where two or more different crystal structures co-exist. However, long integration time XRD experiments of the $Mg_{0.78}Zn_{0.22}O$ film did not show any evidence of the wurtzite minority phase. Further investigation into such structural inhomogeneity in $Mg_xZn_{1-x}O$ based upon the SRRS technique will presented in the later section.

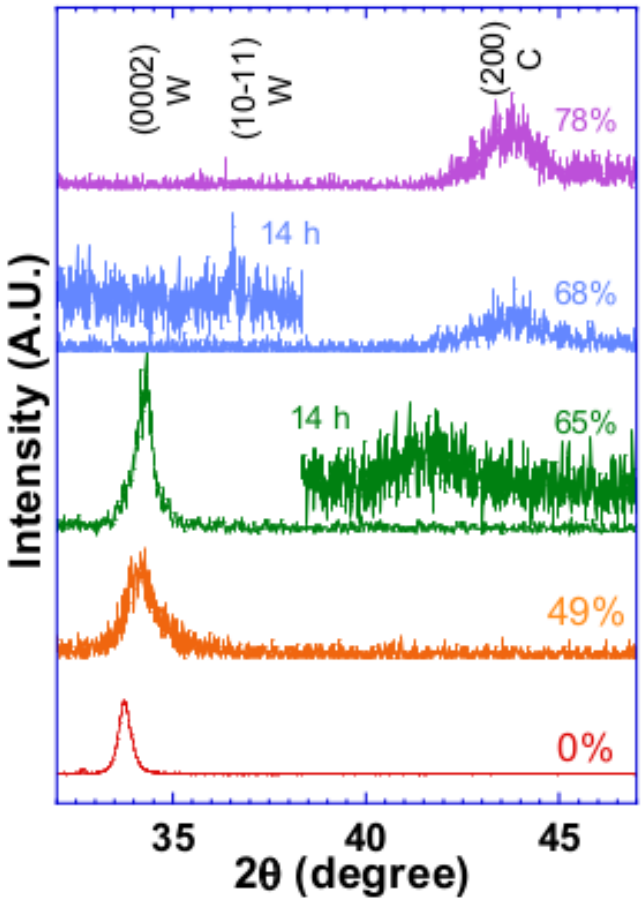

Figure 4.6: *The XRD patterns of several of the MgZnO films. The XRD for a data acquisition time of 2 h indicate that at up to 65% Mg composition the samples have diffraction patterns corresponding to the wurtzite structure, while those of the 68% and 78% compositions correspond to the cubic NaCl structure. For a data acquisition time of 14 h, the XRD indicates that the 65% sample has an additional diffraction peak corresponding to the cubic phase, and the 68% sample has an additional weak peak corresponding to the wurtzite structure phase.*

4.4.3 Structural inhomogeneities in $Mg_xZn_{1-x}O$ alloy films, and their identification via SRRS technique

In this section, a SRRS study of alloy inhomogeneity in all $Mg_xZn_{1-x}O$ samples with Mg composition 0%, 12%, 30%, 49%, 61%, 65%, 68% and 78% is presented. The Raman spectra of the $Mg_xZn_{1-x}O$ films, presented in Figure 4.7 were acquired utilizing both the 3.8 eV and the 5.1 eV laser lines for all samples. Figure 4.8 summarizes the Raman scattering results of 4.7. According to the Raman selection rules, the scattering of longitudinal optical (LO) phonon mode in ZnO with the wurtzite structure is allowed; in contrast, MgO with the cubic NaCl structure has no allowed first order scattering.[37,38] Due to the different Raman selection rules, the properties of the six alloys (0%, 12%, 30%, 49%, 61%, and 65%) with the wurtzite structure are discussed below first, followed by those of the two alloys with the cubic structure (68% and 78%).

As can be seen in Figure 4.7, the spectra of the six samples exhibit the first LO mode and its higher orders, implying a resonant behavior.[39,40] In general, when the laser excitation energy is in the vicinity of some energy states of the crystal, such as bandgap energy, for example, resonant multiphonon scattering occurs. The occurrence of resonant multiphonon scattering, particularly in ZnO and MgZnO alloys has been previously reported in Ref. 41. Thus, probing a phase segregated alloy with different laser lines should result in resonant behavior: conditionally the laser energies are in resonance with the bandgaps of the domains which exist in that alloy.

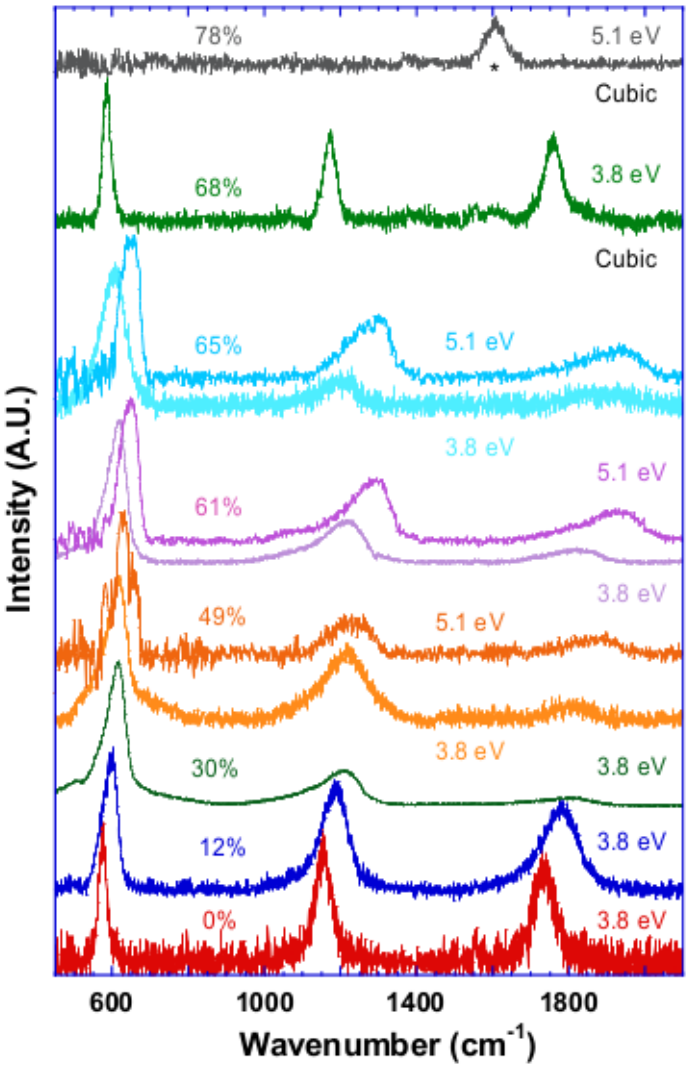

Figure 4.7: *The SRRS spectra of the LO modes and their higher orders of the MgZnO alloys. All spectra, except the 68%, were acquired at room temperature. The 0%, 12%, and 30% samples exhibit Raman scattering only with the 3.8 eV excitation. The 49%, 61%, and 65% samples exhibit Raman scattering with both the 3.8 eV and the 5.1 eV excitations. The 68% and the 78% alloys did not have Raman scattering upon the 5.1 eV excitation. For the 68% sample, the 77K spectrum is presented. The 78% sample did not show any SRRS; a peak at 1620 cm^{-1} is currently under study.*

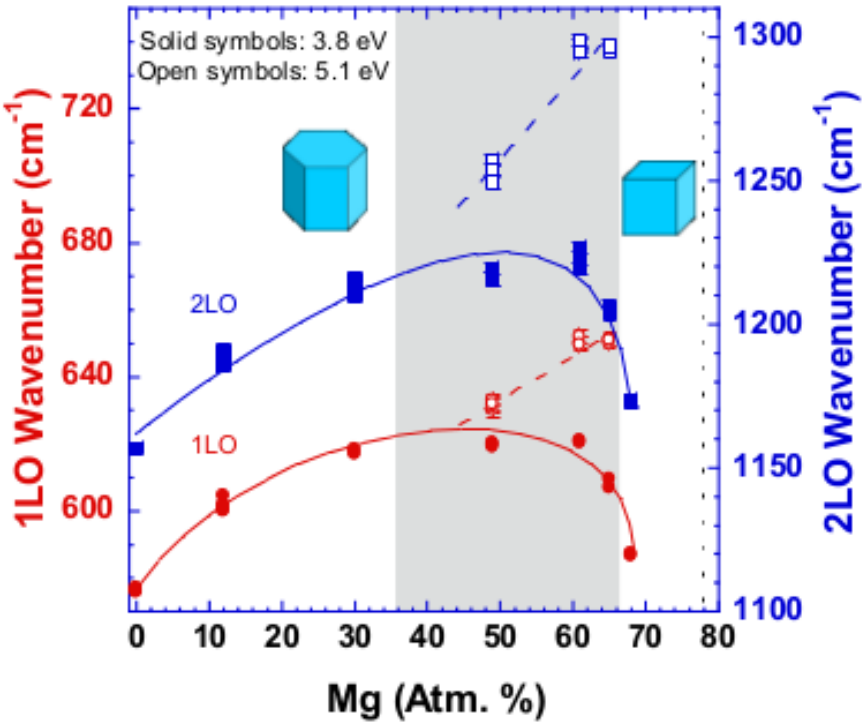

Figure 4.8: *The 1LO and 2LO mode-behavior as a function of Mg composition. The shaded area presents the phase segregation range of the alloys. The vertical dashed line represents the location of the 78% sample. Solid and open symbols are data for the 3.8 and 5.1 eV excitation, respectively. The lines are guide to the eye. As can be seen in Figure, the spectra of the six $Mg_xZn_{1-x}O$ alloy samples (with x = 0%, 12%, 30%, 49%, 61%, 65%) exhibit the first LO mode and its higher orders, implying a resonant behavior. The order of multi-phonon scattering depends on the strength of the electron-phonon interaction. The samples with x = 0.68 and 0.78 did not show any Raman scattering with the 5.1 eV excitation. However, Raman scattering acquired at 77 K for these samples revealed a LO scattering at the lower frequency regime ∼620 cm^{-1} for 68% sample, which corresponds to the scattering from Zn-rich domains.*

With regard to the 0%, 12%, and 30% samples, this group was found to exhibit resonant Raman scattering with the 3.8 eV excitation; the 5.1 eV excitation did not result in any LO Raman scattering. The bandgaps of those aforementioned group of samples as can be seen in figure 4.4 are at the range of $\sim$ 3.2 to 3.7 eV, which is within the excitation energy range. Our results indicate that SRRS was observed and moreover this group of alloy samples does not have significant phase segregation. As can be seen in Figure 4.8, the Raman frequency in the composition range 0%-30% has a shift of ~ 45 cm^{-1}, a result that is similar with that found in a previous study on the resonant Raman behavior of the LO mode in MgZnO films with the wurtzite structure utilizing the 3.8 eV laser line.[18]

In contrast to the samples with the low Mg composition, the samples of higher Mg composition: 49%, 61%, and 65% were found to exhibit resonant behavior with both excitations of 3.8 eV and 5.1 eV, as can be seen in Figures 4.7 and 4.8. For these samples, the 5.1 eV excitation energy resulted in a significantly higher LO mode frequency. This trend excludes the possibility that the two different Raman frequencies, which resulted from the two excitations, are due to probing into the Brillouin Zone. The dispersion curve of the LO phonon of ZnO and MgO is a decreasing function of the k-vector;[42] thus, the 3.8 eV laser, which has a smaller wave vector relative to that of the 5.1 eV laser, should couple to a LO phonon of higher frequency than that of the 5.1 eV excitation. However, this is not what was observed. Furthermore, a depth profile of the Raman frequency was performed with the 5.1 eV laser in order to check the impact of its short absorption length and look for possible surface domain segregation with higher Mg-rich alloy. This experiment resulted in a variance of about 3 cm^{-1} which is within the experimental error, pointing to negligible surface segregation.

The different Raman frequencies resulting from the two laser excitations can be explained within the framework of the selective resonant enhancement for which each excitation is in resonance with energetically compatible composition fluctuation. The

higher LO frequency is due to resonance from Mg rich domains of higher bandgaps, while the lower frequency is due to Zn-rich domains of narrower bandgaps.

To further investigate the structural characteristic of the domains, a long integration time scan XRD pattern, 14 h, was acquired from all samples. These results were shown in Figure 4.6, and indicate that the 65% sample, which has a wurtzite phase component, was found to also exhibit a weak diffraction peak corresponding to the cubic phase. As was stated above, first order Raman scattering from the NaCl structure, which has inversion symmetry, is not allowed. However, defects and impurities can destroy the symmetry, which in turn may result in first order Raman scattering, a phenomenon that was previously observed in MgO and NaCl crystals.[38,43,44]

Additionally, it has been reported that forbidden LO phonons may become Raman active under resonant conditions due to the Frohlich interaction mechanism.[45] In light of the above results, it can be stated that the high-frequency LO-phonon at 650 cm^{-1} of the 65% sample is a SRRS originating in a Mg-rich phase with the NaCl cubic structure. The other two samples, 49% and 61%, which were also concluded via the Raman study to have alloy inhomogeneities, did not show any evidence, from XRD analysis, for the presence of the cubic phase. However, the 49%, and 61% samples are in the range of sufficiently high Mg concentration to favor domain segregation with the NaCl cubic structure. Previous study on the phonon characteristics of pure cubic phase MgZnO, utilizing far-infrared reflection, has found that for a similar Mg composition as the above two samples, LO phonon components are at $\sim$650 cm^{-1}, which is within the frequency range found in the present study utilizing SRRS.[9] The lack of distinctive XRD peaks in this present study may indicate that the cubic domains are too small to be detected via this method.

The investigation of the alloys with the cubic phase, the 68% and the 78% samples, found that neither of these alloys showed any Raman scattering with the 5.1 eV excitation, a result that is consistent with the previously discussed Raman selection

rules for the NaCl structure. Moreover, the room-temperature Raman scattering experiments utilizing the 3.8 eV did not show any meaningful evidence in the spectra of a LO mode resulting from wurtzite phase domains. To further investigate the minority phase in these alloys, Raman scattering was acquired at a temperature of 77 K. In this experiment, the 68% sample was found to exhibit LO scattering at the low frequency regime $\sim$ 620 cm^{-1} which corresponds to scattering from Zn-rich domains. The long integration time XRD of this sample, presented in Figure 4.6, was found to exhibit a very weak diffraction peak assigned to one of the tilted faces of the wurtzite structure. The cold temperature Raman scattering and long integration time XRD experiments of the 78% sample did not show any evidence of the wurtzite minority phase. In light of the above results, it can be stated that in these two alloys the symmetry of the NaCl cubic structure is preserved, the samples do not contain a significant amount of minority phase, and the onset to the cubic phase occurs at $\sim$65% Mg composition.

Additionally, the observed LO phonon mode frequency with Mg composition, in the composition range 0%-30%, has been fitted as shown in Figure 4.9[46] using bowing model of Ye et al.[15] According to this model the phonon frequency as a function of Mg composition has the the following form:

$$\omega(x) = \omega_{ZnO}(1-x) + \omega_{MgO}x - bx(1-x) \tag{4.6}$$

where x is the composition and ω_{ZnO} and ω_{MgO} are the phonon frequencies of the end members, and b is a bowing parameter. This bowing model fits well as can be seen in the Figure 4.9.[46] For the fit, ω_{ZnO}=575 cm^{-1}, ω_{MgO}=618 cm^{-1}, and b=-160 cm^{-1} were taken, which are similar to the values reported previously.[15,47] The agreement between the model and the data indicates that the alloy may not exhibit phase segregation below $\sim$30% Mg which is consistent with the SRRS conclusions.

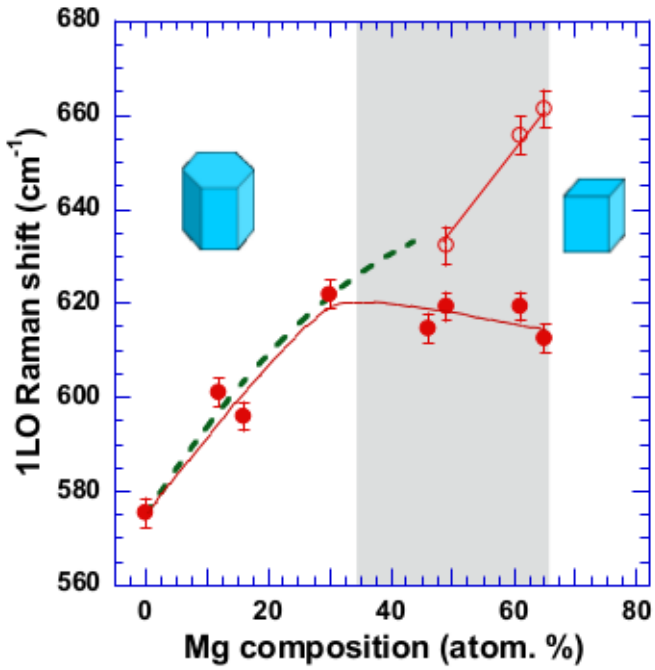

Figure 4.9: *Raman shift for 1LO phonon mode as a function of composition for 3.8 eV (filled circles) and 5.1 eV (open circles) laser excitations. The shaded area represents the wurtzite-rocksalt phase transition region determined from selective resonant Raman scattering. The dashed line is a fit to our observed data following the bowing model.*[15,46] *The solid lines are guides to the eye.*

4.5 Conclusion

In this chapter, a series of MgZnO alloy films with Mg composition ranging from 0 to 78% were successfully synthesized via sputtering and the optical gaps of the samples were found to span the UV range of 3.2-5.8 eV. The issue of phase segregation, inherent to the MgZnO alloy system, was investigated via SRRS which was demonstrated to be a highly sensitive technique for the detection of embedded structural inhomogeneities. The main findings of our work presented in this chapter is:

For the sputtered $Mg_xZn_{1-x}O$ alloy films in the composition range of $0 \leq x \leq 0.78$, the inherent phase segregation range via SRRS was found to be in the range of 35%-65%Mg, in which domains of hexagonal-wurtzite and cubic-NaCl structures coexist.

Some of the other important results obtained via different measurements are included as in the following:

- The $Mg_xZn_{1-x}O$ alloy films with Mg composition $0 \leq x \leq 0.35$ were found to exhibit resonant behavior only with 3.8 eV laser indicating this group of alloy films were in single wurtzite phase without any segregation.

- In contrast, the films with higher Mg composition $0.49 \leq x \leq 0.65$ were found to be in resonance with both the 3.8 eV and 5.1 eV laser energies providing the direct evidence of existence of two embedded wurtzite and cubic structural phases. These results indicate the 3.8 eV laser provides resonance condition for that the wurtzite structural domain while the 5.1 eV laser is in resonance with cubic domains of higher optical gaps.

- As similar to the SRRS result, for $Mg_{0.65}Zn_{0.35}O$ film, the presence two co-existing wurtzite and cubic structural domains were confirmed film via long-

time-integration XRD. Similarly, the long integration time of the sample with the 68% Mg composition was found to exhibit a very weak diffraction peak corresponding to one of the tilted faces of the wurtzite structure while the film with 78% Mg composition did not show any evidence of the minority phase.

- The two alloy films with 68% and 78% Mg composition did not show Raman scattering with the 5.1 eV excitation confirming that the NaCl cubic structure is preserved in these two alloys.

References

[1] A. Ohtomo, M. Kawasaki, T. Koida, K. Masubuchi, H. Koinuma, Y. Sakurai, Y. Yoshida, T. Yasuda, and Y. Segawa, Applied Physics Letters **72**, 2466 (1998).

[2] A. K. Sharma, J. Narayan, J. F. Muth, C. W. Teng, C. Jin, A. Kvit, R. M. Kolbas, and O. W. Holland, Applied physics letters **75**, 3327 (1999).

[3] S. Choopun, R. D. Vispute, W. Yang, R. P. Sharma, T. Venkatesan, and H. Shen, Applied Physics Letters **80**, 1529 (2002).

[4] J. L. Morrison, J. Huso, H. Hoeck, E. Casey, J. Mitchell, L. Bergman, and M. G. Norton, Journal of Applied Physics **104**, 123519 (2008).

[5] X.-B. Chen, J. Huso, J. L. Morrison, and L. Bergman, Journal of Applied Physics **102**, 116105 (2007).

[6] J. Huso, J. L. Morrison, J. Mitchell, E. Casey, H. Hoeck, C. Walker, L. Bergman, W. H. Oo, and M. D. McCluskey, Applied Physics Letters **94**, 061919 (2009).

[7] Ü. Özgür, Y. I. Alivov, C. Liu, A. Teke, M. A. Reshchikov, S. Doğan, V. Avrutin, S.-J. Cho, and H. Morkoç, Journal of applied physics **98**, 041301 (2005).

[8] D. M. Roessler and W. C. Walker, Phys. Rev. Lett. **17**, 319 (1966).

[9] J. Chen and W. Z. Shen, Applied physics letters **83**, 2154 (2003).

[10] C. Bundesmann, A. Rahm, M. Lorenz, M. Grundmann, and M. Schubert, Journal of applied physics **99**, 113504 (2006).

[11] E. R. Segnit and A. E. Holland, Journal of the American Ceramic Society **48**, 409 (1965).

[12] C. W. Teng, J. F. Muth, Ü. Özgür, M. J. Bergmann, H. O. Everitt, A. K. Sharma, C. Jin, and J. Narayan, Appl. Phys. Lett **76**, 979 (2000).

[13] J. Narayan, A. K. Sharma, A. Kvit, C. Jin, J. F. Muth, and O. W. Holland, Solid state communications **121**, 9 (2002).

[14] J. L. Morrison, J. Huso, H. Che, D. Thapa, M. Huso, M. G. Norton, and L. Bergman, Journal of Materials Science: Materials in Electronics **23**, 437 (2012).

[15] J. D. Ye, K. W. Teoh, X. W. Sun, G. Q. Lo, D. L. Kwong, H. Zhao, S. L. Gu, R. Zhang, Y. D. Zheng, S. A. Oh, et al., Applied Physics Letters **91**, 091901 (2007).

[16] C. Bundesmann, M. Schubert, D. Spemann, T. Butz, M. Lorenz, E. M. Kaidashev, M. Grundmann, N. Ashkenov, H. Neumann, and G. Wagner, Applied physics letters **81**, 2376 (2002).

[17] C. Bundesmann, M. Schubert, A. Rahm, D. Spemann, H. Hochmuth, M. Lorenz, and M. Grundmann, Applied physics letters **85**, 905 (2004).

[18] J. F. Kong, W. Z. Shen, Y. W. Zhang, C. Yang, and X. M. Li, Applied Physics Letters **92**, 191910 (2008).

[19] D. Gammon, in *Raman scattering in materials science*, edited by W. H. Weber and R. Merlin (Springer, New York, 2000), p. 109.

[20] D. Gammon, S. W. Brown, E. S. Snow, T. A. Kennedy, D. S. Katzer, and D. Park, Science **277**, 85 (1997).

[21] S. Hernández, R. Cuscó, D. Pastor, L. Artús, K. P. O'Donnell, R. W. Martin, I. M. Watson, Y. Nanishi, and E. Calleja, Journal of Applied Physics **98**, 013511 (2005).

[22] N. Wieser, O. Ambacher, H.-P. Felsl, L. Görgens, and M. Stutzmann, Applied physics letters **74**, 3981 (1999).

[23] V. Lemos, E. Silveira, J. R. Leite, A. Tabata, R. Trentin, L. M. R. Scolfaro, T. Frey, D. J. As, D. Schikora, and K. Lischka, Physical review letters **84**, 3666 (2000).

[24] A. Kar, D. Alexson, M. Dutta, and M. A. Stroscio, Journal of Applied Physics **104**, 073502 (2008).

[25] D. Behr, J. Wagner, A. Ramakrishnan, H. Obloh, and K.-H. Bachem, Applied physics letters **73**, 241 (1998).

[26] L. Bergman, M. Dutta, and R. J. Nemanich, in *Raman scattering in materials science*, edited by W. H. Weber and R. Merlin (Springer, New York, 2000), p. 273.

[27] M. Cardona, in *Light scattering in solids I*, edited by M. Cardona (Springer, Verlag, New York, 1983), p. 1.

[28] J. C. Manifacier, J. Gasiot, and J. P. Fillard, Journal of Physics E: Scientific Instruments **9**, 1002 (1976).

[29] S. Kumar, V. Gupte, and K. Sreenivas, Journal of Physics: Condensed Matter **18**, 3343 (2006).

[30] Y. C. Liu, H. Y. Xu, R. Mu, D. O. Henderson, Y. M. Lu, J. Y. Zhang, D. Z. Shen, X. W. Fan, and C. W. White, Applied physics letters **83**, 1210 (2003).

[31] T. Tsujibayashi, K. Toyoda, S. Sakuragi, M. Kamada, and M. Itoh, Applied physics letters **80**, 2883 (2002).

[32] J. Tauc, in *Amorphous and liquid semiconductors*, edited by J. Tauc (Plenum, London, 1974), p. 159.

[33] S. T. Tan, B. J. Chen, X. W. Sun, W. J. Fan, H. S. Kwok, X. H. Zhang, and S. J. Chua, Journal of Applied Physics **98**, 13505 (2005).

[34] H. Che, J. Huso, J. L. Morrison, D. Thapa, M. Huso, W. J. Yeh, M. C. Tarun, M. D. McCluskey, and L. Bergman, Journal of Nanomaterials **2012**, 1 (2012).

[35] M. Wang, E. J. Kim, S. Kim, J. S. Chung, I.-K. Yoo, E. W. Shin, S. H. Hahn, and C. Park, Thin Solid Films **516**, 1124 (2008).

[36] R. Viswanatha, S. Chakraborty, S. Basu, and D. D. Sarma, The Journal of Physical Chemistry B **110**, 22310 (2006).

[37] T. C. Damen, S. P. S. Porto, and B. Tell, Physical Review **142**, 570 (1966).

[38] K. Ishikawa, N. Fujima, and H. Komura, Journal of applied physics **57**, 973 (1985).

[39] R. C. C. Leite, J. F. Scott, and T. C. Damen, Physical Review Letters **22**, 780 (1969).

[40] M. V. Klein and S. P. S. Porto, Physical Review Letters **22**, 782 (1969).

[41] J. Huso, *Advanced Optical Alloys: Thin Films and Phonon Properties, Ph.D. Dissertation* (2012).

[42] H. Bilz and W. Kress, *Phonon dispersion relations in insulators* (Springer, New York, 1979).

[43] C. Raptis, Physical Review B **33**, 1350 (1986).

[44] R. T. Harley, J. B. Page Jr, and C. T. Walker, Physical Review Letters **23**, 922 (1969).

[45] G. D. Smith, S. Firth, R. J. H. Clark, and M. Cardona, Journal of applied physics **92**, 4375 (2002).

[46] J. Huso, H. Che, D. Thapa, A. Canul, M. D. McCluskey, and L. Bergman, Journal of Applied Physics **117**, 125702 (2015).

[47] H. von Wenckstern, R. Schmidt-Grund, C. Bundesmann, A. Müller, C. P. Dietrich, M. Stölzel, M. Lange, and M. Grundmann, in *Handbook of Zinc Oxide and Related Materials*, edited by Z. C. Feng (Taylor and Francis/CRC Pressr, Boca Raton, FL, 2013), p. 257.

Chapter 5

Achieving Highly-Enhanced UV Photoluminescence and its Origin in ZnO Nanocrystalline Films

5.1 Introduction

As discussed previously in chapter 1, ZnO is a II-VI direct wide bandgap semiconductor material with bandgap value 3.37 eV[1] at room temperature. In recent years, it has received a considerable attention by prospects of its applications in optoelectronic devices due to its unique optical properties such as large exciton binding energy 60 meV[2] and efficient radiative recombination. Examples of some applications of ZnO include gas sensors,[3,4] surface acoustic wave devices[5] transparent conductive contacts,[6] solar cells,[7] ultraviolet light-emitting diodes[8] and ultraviolet lasers.[9,10] Owing to its direct wide band gap, ZnO will emit light in the UV and blue spectral range while its large exciton binding energy will ensure an intense near bandedge excitonic emission at room and even higher temperatures. These properties render ZnO as a key technological material in fabrication of deep UV optoelectronic devices.

In order to realize the potential applications of ZnO films, it is crucial to achieve films with high optical quality that exhibit a strong UV luminescence. However, most of the as-grown films, irrespective of the growth method or substrate, are commonly observed to contain some type of native defects[11] as well as structural defects. The presence of defects can lower the UV emission efficiency and create luminescent centers in the visible, thus limiting the applications of ZnO in optical device technologies.

Previous studies have reported that post-growth annealing treatment is an effective approach to reduce the defect centers, resulting in the enhancement of the films' optical quality.[12–14]. In particular, depending on annealing temperature and ambient, the post annealing of the samples can modify or eliminate native intrinsic defects.

In an effort to achieve an effective route towards enhancement of UV photolumi-

nescence (PL), and gain further understanding of the defect dynamics involved in the process, this research focused on annealing studies and its impact on a wide range of the film's properties. Specifically, two as-grown films were subjected to annealing treatment under two different atmospheres: one film was annealed in an O_2 environment and the other in Ar. The scanning electron microscopy (SEM), X-ray diffraction (XRD), and Raman scattering studies indicate significant improvement of crystal quality and stress relaxation upon annealing. Similarly, the band-edge properties that were investigated via absorption spectroscopy and Urbach analysis indicate that the band-edge characteristics of both annealed films exhibit improvement relative to the as-grown film.

The native defects specific to our films were also analyzed via luminescence spectroscopy. It was found that the as-grown ZnO film is rich in Zn_i that were annealed out under either Ar or O_2 ambient. The O_2 environment was found to introduce some O_i optical centers, while the Ar annealing ambient was found to be the ideal environment for the enhancement of the UV-light emission. The above results are discussed below in terms of the stabilities of the native defects in ZnO with respect to the sputtering growth technique and annealing environments. Finally, the UV-PL at the cold temperature regime was attributed to luminescent centers not associated with the usual excitons of ZnO but rather to structural defects. At room temperature the two emissions convolve.

5.2 Synthesis of ZnO films

Numerous methods have been reported for the fabrication of ZnO films such as molecular beam epitaxy,[9] metallorganic chemical vapor deposition,[5] spray pyrolysis,[15] pulsed laser deposition[16] and magnetron sputtering.[12] In the present work, DC magnetron sputtering has been utilized, which is considered to be relatively cost effective and convenient due to its simple set up. As described for the growth of $Mg_xZn_{1-x}O$

alloy films in chapter 4, the sputtering chamber was evacuated to a base pressure of 10^{-6} Torr, and deposition of the films was carried out by sputtering the Zn metal target in an oxygen-argon gas mixture at a pressure of 11 mTorr and a delivered power of 30W. The films were grown on sapphire substrates for an hour at 250 °C.

5.3 Overview of the post annealing treatment

Post growth annealing is generally desirable in improving the structural and optical properties of the film. The advantages of annealing include the ability of re-using the same sample for multiple studies in different temperatures and environments. This process is essential for the study of the evolution of defects that impact the optical properties of the alloy, and investigations regarding the relation between the growth temperatures and the annealing parameters are needed for the optimization of the samples. Due to pratical reasons; the heater in the growth chamber is expensive, and moreover the low temperature may prevent the corrosion of the chamber by the oxygen in the plasma. In that regard, post growth annealing becomes an attractive and useful methodology.

Upon annealing of the sample, the material from the sample tends to evaporate: the evaporation rate is mainly temperature dependent. In practice, the vapor pressure provides a quantitative estimate of the rate of material loss. The vapor pressure is highly material dependent, and becomes much larger near the material's boiling or sublimation point, though it can be significant even below these points. We are most often concerned about the vapor pressure of the solid phase at a temperature close to our annealing temperature that is relevant to the creation or elimination of defects.

The concept of vapor pressure remains fairly simple as long as we are dealing with evaporation of the material in elemental form or even in the compound as long as the molecule exhibits a stable bond. For example, water is a compound and evaporates as complete water molecules. Thus we may speak of the vapor pressure of water at a

given temperature. Likewise, Zn metal evaporates Zn atoms and Mg metal evaporates Mg atoms. In general, the higher the vapor pressure, the more evaporation takes place.

In the case of binary semiconductor, like ZnO and MgO, it is shown that upon annealing in a given atmosphere and annealing temperature, the semiconductor will dissociate into their constituent materials. For ZnO, it will dissociate into Zn, O_2, ZnO, and O, while MgO will decompose into Mg, O_2, MgO, Mg_2 and O.[17] One can change the vapor pressure of these constituent materials by annealing in a different atmosphere. This behavior can modify the defect dynamics by eliminating or creating defects in the sample being annealed as discussed in section 5.5.

5.4 Annealing experiment

In order to examine the effect of post-annealing treatment on the optical and structural properties of the as-grown films, the films were annealed at 900 °C (1173 K) for 1 h each under a different atmosphere of ultra-high purity O_2 and Ar gases using a Lindberg/Blue M quartz tube furnace controlled by a Yokogawa UP-150 temperature controller, as shown in Figure 5.1 (a). The as-grown sample was placed in a cleaned alumina boat and was inserted into the quartz tube. The inlet and the outlet gas flexible tubes were connected via compression fittings. For Ar annealing, initially the gas lines were purged for 10 min, setting the Ar flow-rate at 1255 cm^3/min. Then, the Ar flow rate was reduced to 273 cm^3/min and the annealing process was started. A similar process was performed for O_2 with flow rates of 100 cm^3/min for purging, and 50 cm^3/min during annealing. The relatively lower O_2 flow rate during the annealing was chosen in consideration of its reactive nature. The purging was done at room-temperature. For the annealing, the program of the furnace was set with a ramp-up and rump-down time of 30 min. The gas flow was continued during the cooling process. The furnace program set for the annealing studies is shown in Figure 5.1(b).

Annealing at such high temperature can result the improvement in the crystal

structure while annealing under different atmospheres can reveal the nature of defects existing in the films based upon their changes and evolution with annealing atmosphere. Chemical composition of the films was determined using energy dispersive X-ray spectroscopy (EDS). Film thickness was determined using a well-known optical interference technique[18] as described in chapter 3. Transmission measurements were performed on the films using a 300 Cary UV-Vis transmission system in double beam mode. Photoluminescence (PL) studies on the films were carried out using the 325 nm line of a Xe lamp, and 325 nm He-Cd laser as excitation sources. Raman spectra are collected using a He-Cd laser (325 nm) as an excitation source. Structural and surface morphology of the as-grown and annealed films were examined utilizing X ray diffraction (XRD) measurements and scanning electron microscopy (SEM), respectively.

It is worth noting that sapphire (0001) substrates were selected as substrates in contrast to CaF_2, used in depositing MgZnO alloy films investigated in previous chapter 4. Since ZnO and $Mg_xZn_{1-x}O$ alloy films grown in this study turn out to be polycrystalline, substrate selection does not seem to play significant role in their structural and optical quality. However, sapphire substrates become desirable particularly when post annealing treatment is intended to perform on the as-grown films. As mentioned in chapter 3, the CaF_2 will become non-transparent upon annealing at 800 °C, and will interfere the optical measurements of the films. Additionally, CaF_2 is found to exhibit photoluminescence (PL) emission nearly in the spectral region where in ZnO luminescence adding complexity while studying luminescent property of ZnO via PL.

(a)

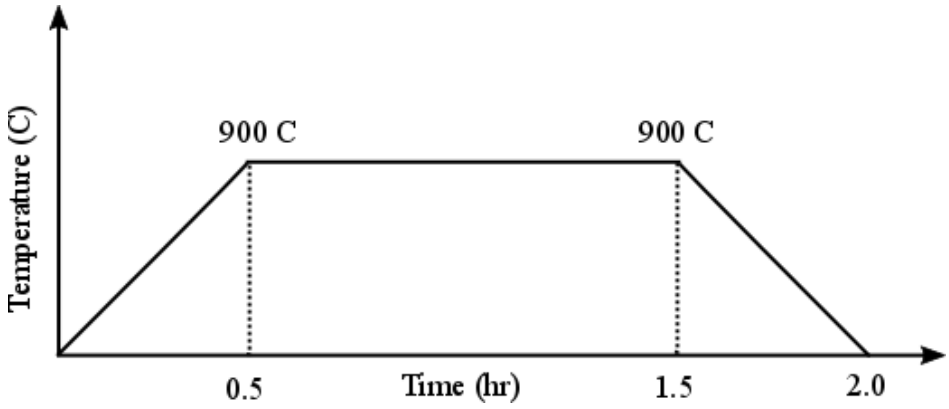

(b)

Figure 5.1: *(a) A photograph Lindberg/Blue M quartz tube furnace controlled by a Yokogawa UP-150 temperature controller used to perform the annealing experiments on the sputtered as-grown ZnO films. (b) The temperature program set in the furnace to perform the annealing studies in this work.*

5.5 Results and discussion

5.5.1 Surface morphology and structural characterization of ZnO films

Figure 5.2(a, b, c) presents SEM images of both the as grown and annealed films. Under high magnification, the image of the as-grown ZnO film reveals that the film consists of a granular morphology with significant secondary nucleation (Figure 5.2a). In contrast, in both annealed films the grains are well defined and exhibit a much improved morphology. No significant difference between the two annealed films is evident from the SEM images.

In order to gain further knowledge on the structural properties of the films, XRD studies were conducted. The XRD scans were referenced to the (0002) line of the sapphire substrate. As can be seen in Fig. 5.3, the XRD patterns of the as-grown and both O_2 and Ar annealed ZnO films showed the (0002) wurtzite peak, indicating that the films are preferentially orientated along the c-axis. The presence of an additional weak diffraction peak, corresponding to (0004) wurtzite structure, in both annealed films indicates their improved crystallinity. Moreover, the (0002) diffraction peak shows strong enhancement in intensity in both annealed films compared to that of the as-grown film. The full-width at half maximum (FWHM) value of the (0002) diffraction peak was found to be $\sim$0.80 degrees for the as grown sample, and much smaller for both of the annealed ones: $\sim$0.30 degrees.

The average grain size was calculated using Scherrer's formula with the calculated FWHM listed above. The calculation indicates that the average grain size for the as-grown sample is $\sim$ 11 nm, while it is $\sim$ 31 nm for both of the annealed ones. It is notable that these calculated values of the grain size are relatively smaller than those presented in the SEM images. A similar observation has been reported previously

where the grain sizes calculated using XRD measurements were found to be smaller than the values revealed under SEM.[19,20] The underlying reasons for the smaller values of grain size estimated from XRD has been attributed to the presence of defects, and to the nature of the method itself.[19,20] Specifically, the XRD method provides preferential information about the size of the region with highly-coherent scattering that usually occurs in smaller regions.[21]

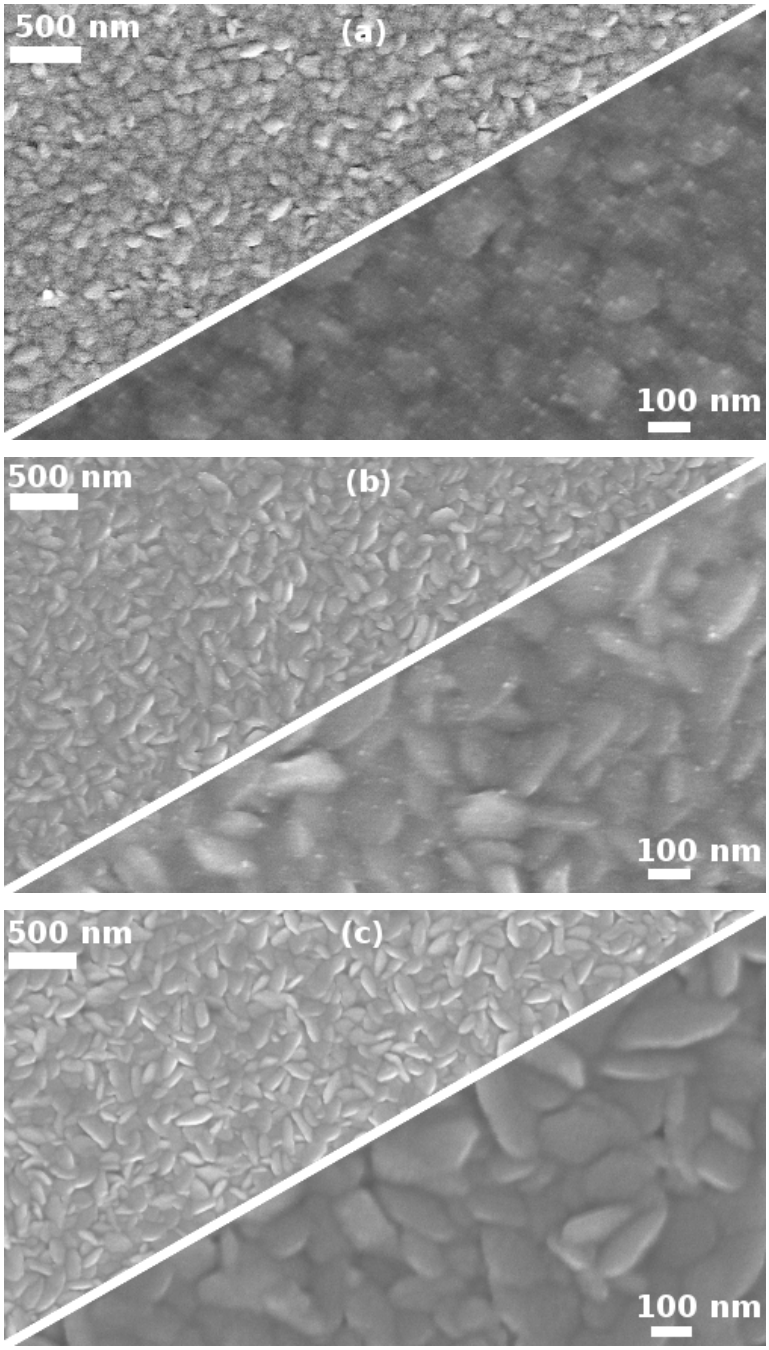

Figure 5.2: *SEM image of ZnO films: (a) as-grown, (b) O_2 annealed, and (c) Ar annealed under low and high magnifications showing their surface morphology. In both annealed films, the grains are well defined and exhibit much improved morphology.*

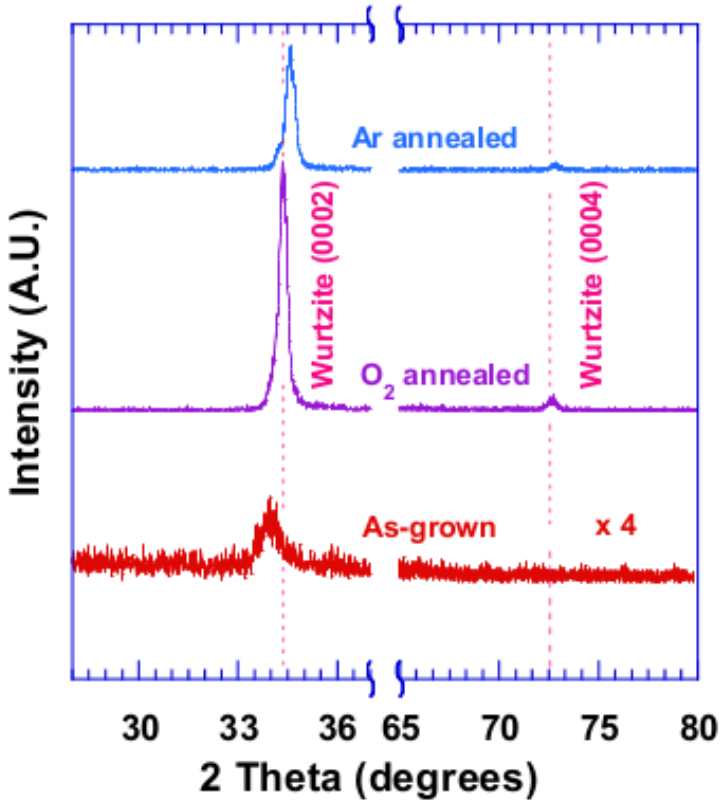

Figure 5.3: *XRD diffraction patterns of ZnO films: as grown, O_2 annealed, and Ar annealed. An additional wurtzite (0004) peak in the annealed films indicate their improved structure after annealing.*

5.5.2 Transmission spectra and Urbach energy analysis

Informative methods that may provide additional insight into crystal dynamics and materials quality are transmission and absorption spectroscopes. One aspect of absorption analysis is what is known as Urbach energy[22,23] that yields a measure of a semiconductor's defects and imperfection, as discussed in the following paragraphs.

The transmission spectra acquired for the as grown and annealed ZnO films are shown in Fig. 5.4. As can be seen in the Figure, the spectra of both annealed samples exhibit a sharper absorption edge relative to that of the as-grown film. Furthermore, no obvious difference can be observed between the transmission spectra characteristics of the films annealed under either Ar or O_2 ambient.

Typically, the presence of defects that include impurities and structural disorders in thin films are known to produce the localized energy states (band tail) within the bandgap, and a good measure of the extent of these states may be given by the Urbach energy.[22,23] The Urbach energy, E_U, can be ascertained using the well known Urbach model.[22–25] According to the model, the absorption coefficient below the optical bandgap follows exponential dependence with the photon energy, i.e.,

$$\alpha(E) = Ce^{\frac{E}{E_U}} \tag{5.1}$$

where $\alpha(E)$ is the absorption coefficient as a function of energy, and C is a constant. Fig. 5.5 presents the Urbach energy analysis for all of the samples, which yields E_U values of 85, 36, and 34 meV for the as-grown, O_2 and Ar annealed films, respectively. The significant reduction in the Urbach energy for both annealed films indicates that a lower concentration of defects exists in these samples relative to that of the as-grown film. As in the case of the XRD analysis, the similar values of Urbach energy of both annealed samples imply that both annealing environments are very useful for defect reduction in ZnO films.

Further studies on the nature of the defects, their dynamics in the annealing process, and their relation to enhancement of the UV-PL, are presented in following section.

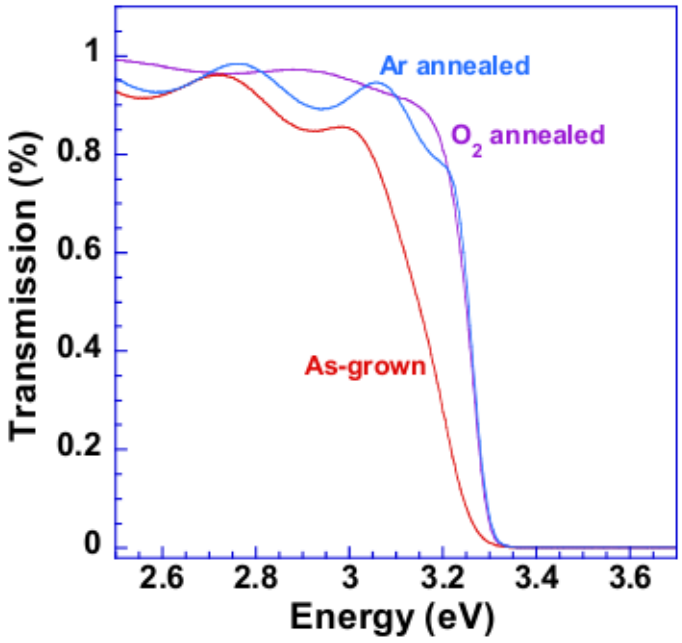

Figure 5.4: *Transmission spectra of ZnO films: as grown, O_2 annealed, and Ar annealed. Transmission spectra indicate the marked improvement in the band edge of the annealed films. The sinusoidal features at low energies are due to the thin film interference.*

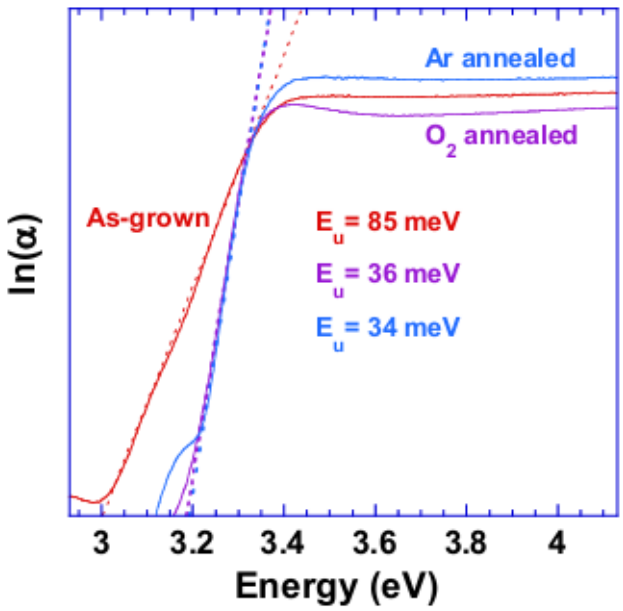

Figure 5.5: *Urbach analysis for the as-grown, Ar annealed and O_2 annealed ZnO films. Urbach energy has been determined via fitting of Urbach model in the linear region below the bandgap. The significant reductions in Urbach energy for both annealed films indicate the lower concentration of the defects in those samples.*

5.5.3 Photoluminescence study

(a) As-grown ZnO film

The above studies indicate that both annealing processes resulted in improving the film quality. However, these studies did not convey insight into the issue of native defects prevalent to ZnO. It has been established that native defects in ZnO luminesce in the visible range, and that PL is a quite informative approach regarding the identification of these defects. In most studies of ZnO, PL spectra show two emission bands.[11,13,26–28] One of these bands, the near band edge (NBE) emission, is located near the bandgap and lies in the ultraviolet region. Another band is located in the visible spectral region and is generally known as the deep level emission (DLE).[16,26,29,30] The NBE emission peak is typically attributed to excitonic recombination, while the origin of the DLE band is usually attributed to optical centers associated with impurities such as native defects. Since the energetics of the NBE and DLE can provide two competing routes to carrier recombination, it is usually desirable to minimize the defect centers in order to enable the enhancement of the UV emission.[30] In the following, we present a study whereby the presence of native impurities was minimized during annealing, and efficient UV emission is achieved.

As can be seen in Fig. 5.6(a), PL spectra of the as-grown films showed a weak and broad PL peak extending from visible to the UV region. The deconvolution of the spectral-line indicates that a visible emission is centered at ∼2.80 eV, and the UV one is at 3.25 eV. The UV PL is attributed to the band-edge emission in ZnO, and its origin in our sample will be discussed further in detail in section 5.6. Hereafter, the emission peak at ∼2.80 eV will be referred to as the blue emission. As can be seen in Fig. 5.6(a), the UV-PL intensity is relatively weak compared to the blue emission.

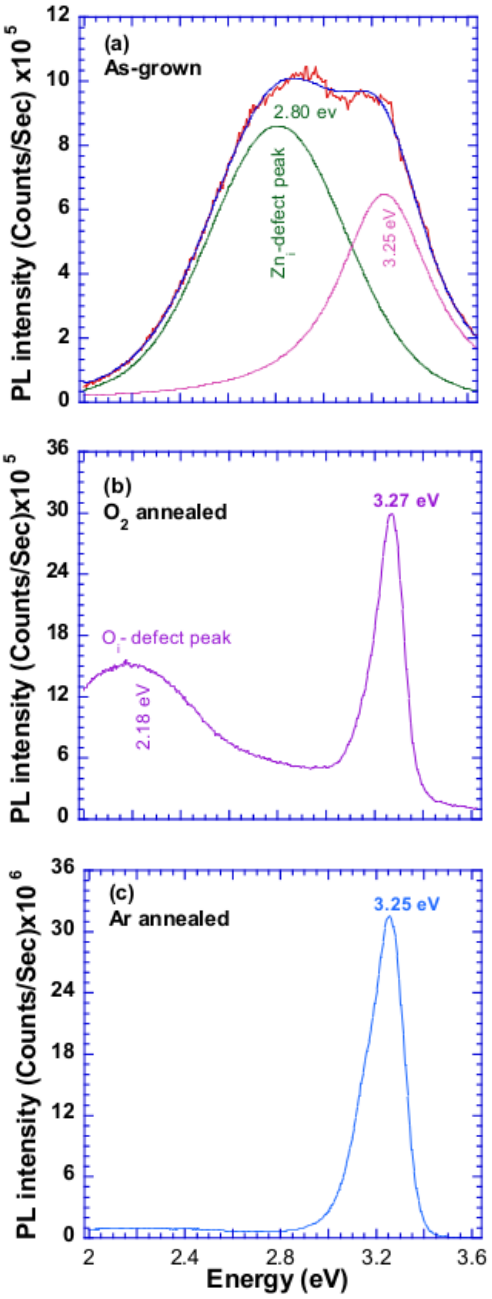

Figure 5.6: *Room temperature PL spectra of the ZnO films: (a) as grown film showing two peaks at ∼2.80 and 3.25 eV were obtained with a Voigt profile fitting to the experimental curve. The 3.25 eV is attributed to UV band-edge emission and the 2.80 eV is due to Zn_i related defects, (b) O_2 annealed film showing enhanced UV PL peak and an Oi related peak, and (c) Ar annealed ZnO film showing the significantly enhanced UV PL with a nearly quenched visible emission peak. Note that the vertical scale in Figure 5.6 (c) is different from 5.6 (a) and 5.6 (b), showing significantly enhanced UV PL after Ar annealing. The UV PL intensity of the Ar annealed film is about 40 times stronger compared to that the as-grown film.*

The observed blue emission has been reported previously in ZnO films[31], micro whiskers[32], and nanoparticles[33]. Fang et al.[31] have previously investigated the blue PL spectra, ∼2.9 eV, of the sputtered ZnO films via PL and electrical measurements, and found it to be correlated with the density of Zn_i defects in the films.[31] Xu et al.[32] studied, via XRD, EDS (energy dispersive X-ray spectrosocpy) and EPR (electron paramagnetic resonance), the evolution of blue (∼2.95 and 2.83 eV) and green emissions (∼2.44 eV) of ZnO microwhiskers grown by a vapor-phase transport method.[32] They have found a correlation between the evolution of visible emissions in the PL with structural features, stoichiometry and paramagnetic defect centers. The blue and green emissions in Xu's study were suggested to be related to Zn_i and V_O^+, respectively, formed during growth.[32]

Additionally, Zeng et al. have established that blue luminescence (∼2.8-3.0 eV) in the ZnO nanoparticles increased rapidly under low annealing temperature, and quenched under high annealing temperature in air and N_2 atmosphere.[33] In their study, the emission was discussed in terms of transition from Zn_i-related defect levels to the valence band. Kayaci et al. have confirmed the existence of Zn_i related defects in ZnO nano-structures via X-ray photoelectron spectroscopy (XPS), and attributed the blue PL (2.83-3.10 eV) to these defects.[34] Table I presents some of the relevant properties of the native defects in ZnO.

Figure 5.7 presents a tentative energy level diagram for Zn_i related defects in ZnO which is consistent with the blue emission observed in this study. The bandgap value of our ZnO film was determined via Tauc analysis to be ∼ 3.27 eV. Taking this value into account in conjunction with the PL value of 2.80 eV, the Zn_i-related defect level appears to lie ∼0.47 eV below the conduction band. This value for the Zn_i energy level is in good agreement, up to experimental error, with the values summarized in Table I.

Table 5.1: Native defects of ZnO: their PL emission, energy levels, and mobility temperature

Defect	PL emission in eV	Energy Levels (values in eV)	Defect type	Mobility temp (migration barrier)
Zn_i or Zn_i-related	∼2.9 [31] ∼(2.83 and 2.95) [32] ∼2.8-3.0 [33] ∼2.83-3.10 [34] ∼2.88 [35]	∼0.4 eV below CB [36] ∼0.30 eV below CB [35] ∼0.28 eV below CB [37] ∼0.15 eV below [38] CBM(+2/+1)	Shallow Donor [39]	170K [40] (0.57 eV) [39]
O_i	∼2.11 [41] ∼2.13 [42]	1.18 above VB(-/2-) [43] 1.59 above VB(-/2-) [39] ∼1.09 above VB [37,44]	Deep acceptor [39]	440K [39,45] (1.1 eV) [39]
V_{Zn}	∼2.5 [45]	0.1-0.2 above VBM(0/-1) and 0.9-1.2 above VBM(-/-2) [40,45,46] 0.9 above VB (exp) [47]	Deep acceptor [45]	473-573K [40] (1.4 eV) [39]
V_O	2.40 [48]	0.5-0.8 above VBM [40] 1-2 below CBM(-/-2) [40] ∼2.1 below CBM [47] (for neutral V_O)	Deep Donor [39]	673K [40] (2 eV [40])
O_{Zn}	-	1.52 above VBM (0/-1) [39] 1.77 above VBM (-/-2) [39]	Deep acceptor [39]	-
Zn_O	-	-	Donor [39]	-

In typical cases, the formation energy of Zn_i is reported to be quite high, but can be reduced in Zn-rich growth conditions in accordance with the reported calculations.[33,38,49] For the study presented here, a DC sputtering technique was utilized to grow the films, which can lead to the growth of Zn-rich films thereby favoring the formation of Zn_i-related defects in the films. The phenomenon of sputtering growth which results in Zn-rich films is commonly reported in the literature[12,21,50] and can be understood by noting that sputtering involves the competing processes of target oxidation and removal of target material. To achieve growth, the target material, i.e., Zn, must be removed at a sufficient rate so as to prevent an oxide overcoating of the target. However, by removing the target material at high rates, the sputtered material

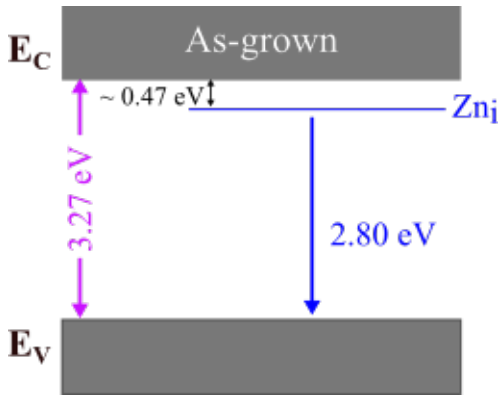

Figure 5.7: *Schematic energy band diagram of the proposed transition mechanism for the blue PL emission in the as grown ZnO film. The bandgap value, 3.27 eV, was obtained via well the known method of Tauc plot analysis. The blue PL is assigned to the transition from Zn_i related defect level to valence band, the Zn_i-defect being placed ∼0.47 eV below the conduction band.*

may not be completely oxidized, a condition that favors Zn-rich film.

In principle, Zn-rich films may contain Zn_i as well as oxygen vacancies (V_O) as native defects. The PL of V_O was suggested to be in the green spectral-range of ∼2.4 - 2.5 eV[16], and as can be seen in Figure 5.6(a), it is not pronounced in our PL spectrum. The latter imply that V_O is not a dominant native impurity in the as-grown ZnO film. It bears noting that the stability of Zn_i is still an ongoing research topic; however, several experimental results showed convincing evidence that Zn_i and related defects centers can be present in the ZnO sample.[32–34]

(b) Annealed ZnO films

Having examined the as-grown film, we now turn our attention to the ZnO film annealed at 900 °C under oxygen atmosphere. As can be seen in Figure 5.6(b), the O_2 annealed films showed a much more pronounced UV emission than that of the as-grown film. Additionally, the blue PL that was observed in the as-grown film at ∼ 2.8 eV is not detectable, and a new visible PL at ∼ 2.18 eV is observed. The disappearance of blue emission, due to Zn_i-related defects, after O_2 annealing treatment can be understood

in terms of the fast diffusive nature of Zn_i-related defects. From density functional calculations, Janotti et al.[39] reported that the migration barrier of Zn_i to be 0.57 eV, which is considered to be relatively low. Alternatively, the mobility temperature of these defects, which was previously found to be ∼170 K (see Table 5.1), is much lower than our annealing temperature 1173 K. In light of these properties, it is reasonable to expect that Zn_i related defects should diffuse out or incorporate into substitution lattice sites.

The emergence of the visible emission PL ∼ 2.18 eV, also known as the yellow luminescence[41,42,51,52] has been previously studied by several groups and was attributed to oxygen interstitial (O_i) defects in ZnO.[41,42,51] We surmise that annealing under O_2 ambient is conducive to the formation of O_i defects. The high partial pressure of oxygen in the environment will lead to diffusion of oxygen into the lattice, resulting in O_i defects.

While the formation energy of O_i defects is predicted to be high in ZnO,[43] resulting in an expectation of minimal O_i defect concentration, O_i defects are also mobile above 440 K[39,45](see Table 5.1). Thus the combination of high annealing temperature (1173 K) and high oxygen partial pressure creates conditions favorable for the formation of O_i defects, and also to rapid diffusion through the lattice. With regards to the bandgap mapping this sample: theoretical calculation by Janotti et al. has previously predicted that O_i defects form a deep acceptor at 1.18 eV above the valence band.[43] The bandgap of the O_2 annealed ZnO film, as was determined from Tauc analysis, is ∼3.29 eV, while the PL is at 2.18 eV: these energetics agree with a transition from the conduction band to a state at ∼1.11 eV above the valence band. Our obtained experimental value agrees closely with the theoretical value of 1.18 eV reported by Janotti et al.[43]

As is shown in Figure 5.6(c), the UV PL for the Ar annealed ZnO film is significantly enhanced, while there is only a trace of the visible emission. This can be understood by noting that during annealing under Ar atmosphere the Zn_i-related defects residing in

the as-grown film will be eliminated. This dynamic is similar to that discussed for the case of the O_2 annealed sample, i.e., the low mobility temperature and low migration barrier of the Zn_i-related defects will cause out-diffusion or lattice incorporation of these defects. Additionally, Ar is a non-reactive atmosphere, and thus no new defects should be introduced. The key point is that the UV PL intensity of the Ar annealed film is about 40 times stronger compared to that of the as-grown film. The enhancement of the UV luminescence is attributed to the elimination of the competing routes to the UV light emission due to the defects.

5.5.4 Raman study on as-grown and annealed ZnO film

As can be seen in the SEM images, the morphology of both annealed samples was significantly improved relative to that of the as-grown sample. Also it is expected that annealing will relax the stress state of a sample. In general, Raman scattering was proven to be a highly sensitive spectroscopy, enabling the assessment of a material's internal stress via the frequency shift of a particular Raman mode. In the following we present Raman analysis of the three ZnO samples. The Raman spectra were acquired in a back scattering geometry utilizing the 325 nm (3.81 eV) HeCd laser line. The experimental error is $\sim \pm 1$ cm^{-1}. Since that excitation energy is close to the bandgap of ZnO, resonant Raman scattering occurs resulting in enhanced LO mode[53].

Fig. 5.8 presents the Raman spectra of the films. As can be seen in the figure, the LO-mode exhibits a systematic shift towards the lower frequency, starting at 578 cm^{-1} for the as-grown sample, then 575 cm^{-1} for the oxygen annealed, and 573 cm^{-1} for the argon annealed sample; i.e., a total shift of $\sim$5 cm^{-1}. The shift towards the lower frequency may be suggestive of a relaxation of intrinsic compressive stress. The pressure coefficient $\left(\frac{\partial\omega}{\partial P}\right)$ for the LO-mode in ZnO (where ω is the phonon frequency) was found previously to be in the range of $\sim$4.14-4.56 cm^{-1}/GPa[54,55]; a similar pressure coefficient, $\sim$4.9 cm^{-1}/GPa, was obtained by our group for the case of ZnO doped with

a small percentage of Mg[56]. Since the observed Raman shift is $\sim$5 cm^{-1}, a relaxation of $\sim$1 GPa took place upon annealing. Furthermore, this relaxed stress of $\sim$1 GPa is comparable to those obtained previously via XRD and curvature measurement studies of ZnO thin films grown via the sputtering method.[57,58] The compressive stress in our samples can be attributed to structural defects and Zn aggregation, both of which were significantly reduced during the annealing process. In addition, the Raman linewidth of the films shows narrowing upon annealing, as is indicated in Figure 5.8. The narrowing may be attributed to the increase in the phonon lifetime, which is a result of the improved crystallinity of both annealed films.

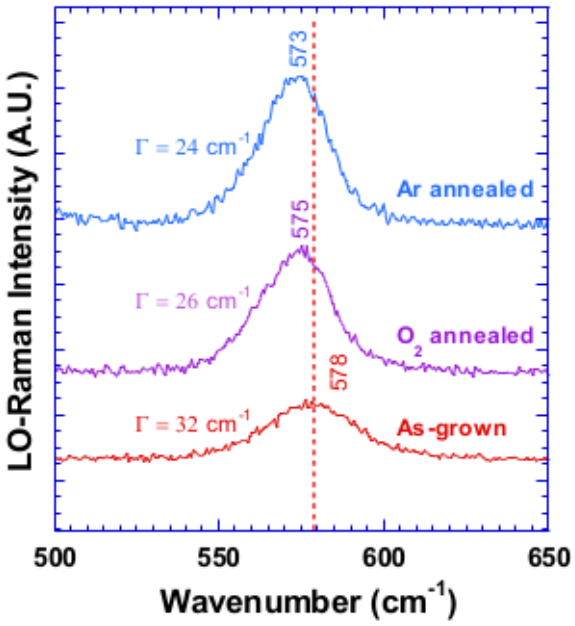

Figure 5.8: *Raman spectra of ZnO films: as grown, O_2 annealed and Ar annealed. Smaller FWHM of Raman first order LO mode in annealed films indicate their improved crystallinity. The shift of Raman phonon mode towards the lower frequency may suggest the relaxation of intrinsic compressive stress.*

5.6 Low temperature PL measurement: Origin of UV PL

Having found that Ar annealing generates the highest UV emission intensity, we next investigate its actual origin. Fig. 5.9 presents the PL spectrum at 77 K for the Ar annealed ZnO film along with that of ZnO nanocrystals reported in our previous work.[59] Additionally, the cold temperature PL spectrum of ZnO single crystal is also included as a reference.

As can be seen in Fig. 5.9, the PL spectrum of the single crystal ZnO consists of two main spectral lines at 3.362 and 3.376 eV. These two PL emissions have been extensively studied by various groups, and have been assigned to a neutral donor-bound exciton D^oX and the A-exciton X, respectively.[59,60] As shown in Fig. 5.9, in the spectrum of Ar annealed sample, the D^oX and the A-exciton are present at nearly at the same energies as those of the single crystal. A key finding is that in addition to two excitonic emission lines, the PL of ZnO film exhibits a strong line at $\sim$ 3.314 eV, referred to as the ε-PL, which is red shifted by $\sim$ 58 meV from the A-exciton. The ε-emission was previously found by us to be the dominant PL in ZnO nanocrystals of size $\sim$ 40 nm, and was attributed to structural defects.[59] The ZnO nanocrystals were grown via a chemical approach, while the films were deposited via a sputtering technique; both methods resulted in a nano-scale granular morphology which seems to be the reason for the onset of the specific UV luminescence.

In order to get further insight about ε-PL emission peak, temperature dependent PL measurements were performed starting from 83 K to room temperature and presented in Figure 5.10 (a) and (b). At lower temp. ε-PL appears to dominate the spectra while at room temperature the bandedge PL of the film becomes the convolution of the ε-PL with that of the exciton peaks.

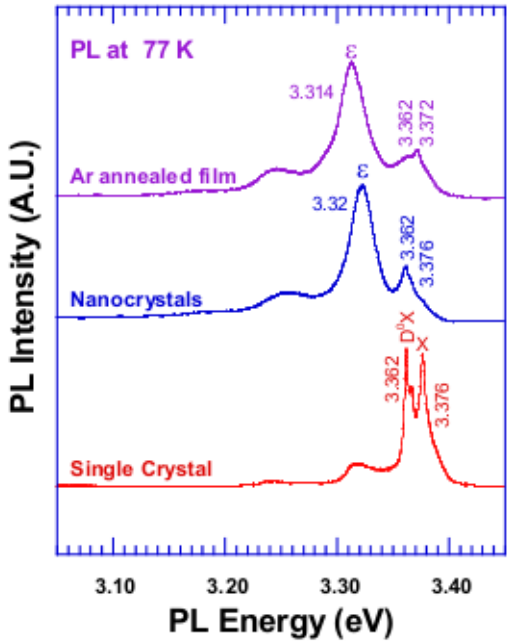

Figure 5.9: *The PL spectra at 77 K of ZnO samples (lower three traces): single crystal, nanocrystals, and Ar annealed film. The single crystal spectrum exhibits the usual ZnO excitons: the bound exciton D^oX ∼3.362 eV, and the free A-exciton X ∼3.376 eV. The peaks observed for the Ar annealed film exhibit the ZnO excitons and an additional peak, ε-PL, related to structural defects. The nanocrystals have a similar PL spectrum to that of the film. The phonon replicas are at the lower energy range. The spectrum for the nanocrystals is from Ref. 59.*

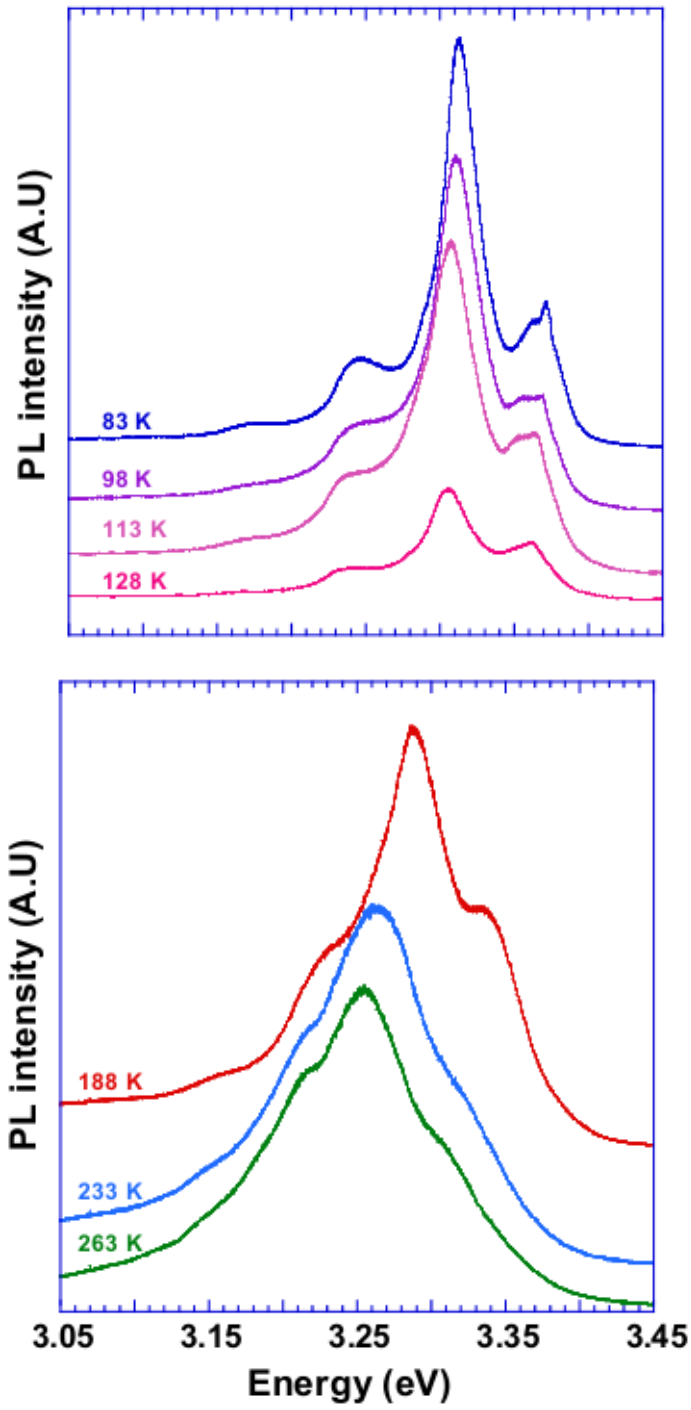

Figure 5.10: *Temperature dependent PL spectra of Ar annealed film at the temperature range (a) 83-128 K (b) 188-263 K. At lower temperature the ε- dominates the spectra while at higher temperature the spectra becomes convolved with ε- and free excitonic emission.*

A discussion follows concerning the impact of the choice of substrates on the optical properties. The research of our group focuses on semiconductors with extreme bandgaps that include ZnO-based alloys such as $Mg_xZn_{1-x}O$. The bandgaps of these alloys span a large UV range of $\sim 3.3-6$ eV.[22] In order to ensure the transparency of the film/substrate product, as is desirable for some technological applications, substrates with a wide-bandgap are chosen. In this research, two-side polished c-face sapphire substrates were used. The bandgap of a single-crystal sapphire is ∼8.8 eV[61] which makes it optically compatible to the $Mg_xZn_{1-x}O$ films. The other substrate that we commonly use, due to its UV compatibility, is quartz with a reported bandgap ∼8.9 eV.[62]

Our ongoing research did not find a significant difference among the optical properties of the films using either sapphire or quartz as a substrate. Fig. 5.11 presents the PL spectra of as-grown ZnO film and that of the Ar annealed film grown on quartz. As can be seen in the figure, the PL characteristics of the as-grown film and that of the Ar annealed are very similar to those of the ZnO grown on sapphire substrate (see Fig. 5.6(a), (c)); an enhancement, of ∼ 35-times, for the UV emission was achieved. Future research will address additional substrates of relevance to opto-electronic technologies, such as silicon and GaN.

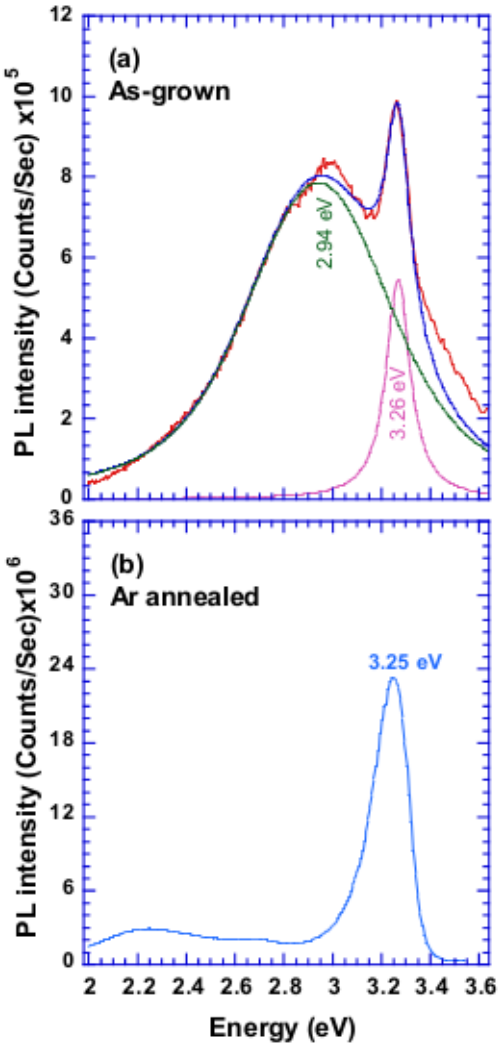

Figure 5.11: *Room temperature PL spectra of the film grown on quartz substrate (a) as-grown film (b) the Ar annealed film.*

5.7 Conclusion

In this chapter, we investigated the defect dynamics and optical properties of of ZnO sputtered films via post growth annealing under each Ar and O_2 environments, with XRD, imaging, transmission, Urbach analysis, Raman scattering, and photoluminescence (PL). The key result of our work presented in this chapter is:

After annealing in either environment, the 2.8 eV emission center observed in the as-grown ZnO film was diminished, accompanied by morphology improvement, and the desirable UV-PL significantly increased. The O_2 ambient was found to introduce nominal O_i centers while the Ar ambient was found to be the ideal environment for the enhancement of the UV-light emission: an enhancement of $\sim$ 40 times was achieved. The increase in the UV-PL is attributed to the reduction of Zn_i-related defects, the presence of which in ZnO provides a competing route to the UV emission. Also the enhanced PL was found to correlate with the improved morphology of the film upon annealing.

Some other additional important results obtained via different measurements techniques are summarized as follows:

- The energy band diagram and mapping for the as-grown and O_2 annealed samples that were ascertained via PL and Tauc plots were found to be consistent with theoretical predictions and previous experimental studies for the energy levels of Zn_i and O_i.
- The imaging, XRD, Raman and Urbach analyses indicate significant improvement in crystal morphology and band-edge characteristics upon annealing. These improvements were found to be independent of the annealing environment.

- The Raman linewidth of both annealed samples are similar. They are smaller than that of the as-grown sample, indicating a similar extent of improvement of the crystal structure in either annealing environment.

- Based on the frequency shift, the stress relaxation of ~ 1 GPa is estimated upon annealing.

- Finally, the UV-PL at the cold temperature regime was attributed to luminescent centers not associated with the usual excitons of ZnO, but rather to structural defects. At room temperature the two emissions convolve.

References

[1] Y. Chen, D. M. Bagnall, H.-j. Koh, K.-t. Park, K. Hiraga, Z. Zhu, and T. Yao, Journal of Applied Physics **84**, 3912 (1998).

[2] W. Y. Liang and A. D. Yoffe, Physical Review Letters **20**, 59 (1968).

[3] N. J. Dayan, S. R. Sainkar, R. N. Karekar, and R. C. Aiyer, Thin Solid Films **325**, 254 (1998).

[4] B. B. Rao, Materials Chemistry and Physics **64**, 62 (2000).

[5] C. R. Gorla, N. W. Emanetoglu, S. Liang, W. E. Mayo, Y. Lu, M. Wraback, and H. Shen, Journal of Applied Physics **85**, 2595 (1999).

[6] N. Ameera, A. Shuhaimi, N. Surani, M. Rusop, M. Hakim, M. H. Mamat, M. Mansor, M. Sobri, V. Ganesh, and Y. Yusuf, Ceramics International **41**, 913 (2015).

[7] W. W. Wenas, A. Yamada, K. Takahashi, M. Yoshino, and M. Konagai, Journal of Applied Physics **70**, 7119 (1991).

[8] H. Ohta, K.-i. Kawamura, M. Orita, M. Hirano, N. Sarukura, and H. Hosono, Applied Physics Letters **77**, 475 (2000).

[9] Z. K. Tang, G. K. L. Wong, P. Yu, M. Kawasaki, A. Ohtomo, H. Koinuma, and Y. Segawa, Applied Physics Letters **72**, 3270 (1998).

[10] D. C. Reynolds, D. C. Look, and B. Jogai, Solid State Communications **99**, 873 (1996).

[11] F. K. Shan, G. X. Liu, W. J. Lee, and B. C. Shin, Journal of Applied Physics **101**, 053106 (2007).

[12] W. S. Shi, O. Agyeman, and C. N. Xu, Journal of Applied Physics **91**, 5640 (2002).

[13] Y. R. Jang, K.-H. Yoo, and S. M. Park, Journal of Vacuum Science & Technology A **28**, 216 (2010).

[14] L. M. Kukreja, P. Misra, J. Fallert, D. M. Phase, and H. Kalt, Journal of Applied Physics **112**, 013525 (2012).

[15] S. A. Studenikin, M. Cocivera, W. Kellner, and H. Pascher, Journal of luminescence **91**, 223 (2000).

[16] H. S. Kang, J. S. Kang, J. W. Kim, and S. Y. Lee, Journal of Applied Physics **95**, 1246 (2004).

[17] R. H. Lamoreaux, D. L. Hildenbrand, and L. Brewer, Journal of physical and chemical reference data **16**, 419 (1987).

[18] J. C. Manifacier, J. Gasiot, and J. P. Fillard, Journal of Physics E: Scientific Instruments **9**, 1002 (1976).

[19] J. Huso, J. L. Morrison, H. Che, J. P. Sundararajan, W. J. Yeh, D. McIlroy, T. J. Williams, and L. Bergman, Journal of Nanomaterials **2011**, 1 (2011).

[20] K. Srinivasarao, G. Srinivasarao, K. V. Madhuri, K. Krishna Murthy, and P. K. Mukhopadhyay, Indian Journal of Materials Science **2013**, 1 (2013).

[21] V. V. Khomyak, M. M. Slyotov, I. I. Shtepliuk, G. V. Lashkarev, O. M. Slyotov, P. D. Marianchuk, and V. V. Kosolovskiy, Journal of Physics and Chemistry of Solids **74**, 291 (2013).

[22] J. Huso, H. Che, D. Thapa, A. Canul, M. D. McCluskey, and L. Bergman, Journal of Applied Physics **117**, 125702 (2015).

[23] M. F. Malek, M. H. Mamat, Z. Khusaimi, M. Z. Sahdan, M. Z. Musa, A. R. Zainun, A. B. Suriani, N. D. Md Sin, S. B. Abd Hamid, and M. Rusop, Journal of Alloys and Compounds **582**, 12 (2014).

[24] S. Dutta, S. Chattopadhyay, D. Jana, A. Banerjee, S. Manik, S. K. Pradhan, M. Sutradhar, and A. Sarkar, Journal of applied physics **100**, 114328 (2006).

[25] J. I. Pankove, *Optical processes in semiconductors* (Dover, New York, 1975).

[26] M. Willander, O. Nur, J. R. Sadaf, M. I. Qadir, S. Zaman, A. Zainelabdin, N. Bano, and I. Hussain, Materials **3**, 2643 (2010).

[27] L. Irimpan, D. Ambika, V. Kumar, V. P. N. Nampoori, and P. Radhakrishnan, Journal of Applied Physics **104**, 033118 (2008).

[28] D. Li, Y. H. Leung, A. B. Djurišić, Z. T. Liu, M. H. Xie, S. L. Shi, S. J. Xu, and W. K. Chan, Applied Physics Letters **85**, 1601 (2004).

[29] C. Tsakonas, W. Cranton, F. Li, K. Abusabee, A. Flewitt, D. Koutsogeorgis, and R. Ranson, Journal of Physics D: Applied Physics **46**, 095305 (2013).

[30] Y. G. Wang, S. P. Lau, X. H. Zhang, H. H. Hng, H. W. Lee, S. F. Yu, and B. K. Tay, Journal of Crystal Growth **259**, 335 (2003).

[31] Z. Fang, Y. Wang, D. Xu, Y. Tan, and X. Liu, Optical Materials **26**, 239 (2004).

[32] X. Xu, C. Xu, J. Dai, J. Pan, and J. Hu, Journal of Physics and Chemistry of Solids **73**, 858 (2012).

[33] H. Zeng, G. Duan, Y. Li, S. Yang, X. Xu, and W. Cai, Advanced Functional Materials **20**, 561 (2010).

[34] F. Kayaci, S. Vempati, I. Donmez, N. Biyikli, and T. Uyar, Nanoscale **6**, 10224 (2014).

[35] N. S. Han, H. S. Shim, J. H. Seo, S. Y. Kim, S. M. Park, and J. K. Song, Journal of Applied Physics **107**, 084306 (2010).

[36] B. Lin, Z. Fu, and Y. Jia, Applied Physics Letters **79**, 943 (2001).

[37] S. Kuriakose, B. Satpati, and S. Mohapatra, Physical Chemistry Chemical Physics **16**, 12741 (2014).

[38] P. Erhart, K. Albe, and A. Klein, Physical Review B **73**, 205203 (2006).

[39] A. Janotti and C. G. Van de Walle, Reports on Progress in Physics **72**, 126501 (2009).

[40] M. D. McCluskey and S. J. Jokela, Journal of Applied Physics **106**, 071101 (2009).

[41] X. L. Wu, G. G. Siu, C. L. Fu, and H. C. Ong, Applied Physics Letters **78**, 2285 (2001).

[42] C. Chandrinou, N. Boukos, C. Stogios, and A. Travlos, Microelectronics Journal **40**, 296 (2009).

[43] A. Janotti and C. G. Van de Walle, Journal of Crystal Growth **287**, 58 (2006).

[44] C. H. Ahn, Y. Y. Kim, D. C. Kim, S. K. Mohanta, and H. K. Cho, Journal of Applied Physics **105**, 13502 (2009).

[45] A. Janotti and C. G. Van de Walle, Physical Review B **76**, 165202 (2007).

[46] M. G. Wardle, J. P. Goss, and P. R. Briddon, Physical Review B **72**, 155108 (2005).

[47] S. M. Evans, N. C. Giles, L. E. Halliburton, and L. A. Kappers, Journal of Applied Physics **103**, 043710 (2008).

[48] K. Vanheusden, W. L. Warren, C. H. Seager, D. R. Tallant, J. A. Voigt, and B. E. Gnade, Journal of Applied Physics **79**, 7983 (1996).

[49] A. Kohan, G. Ceder, D. Morgan, and C. G. Van de Walle, Physical Review B **61**, 15019 (2000).

[50] S.-Y. Chu, W. Water, and J.-T. Liaw, Journal of the European Ceramic Society **23**, 1593 (2003).

[51] L. E. Greene, M. Law, J. Goldberger, F. Kim, J. C. Johnson, Y. Zhang, R. J. Saykally, and P. Yang, Angewandte Chemie **42**, 3031 (2003).

[52] M. A. Reshchikov, J. Garbus, G. Lopez, M. Ruchala, B. Nemeth, and J. Nause, in *Mater. Res. Soc. Symp. Proc.,* (2006), vol. 957 (2007), p. 219.

[53] L. Bergman, X.-B. Chen, J. Huso, J. L. Morrison, and H. Hoeck, Journal of applied physics **98**, 093507 (2005).

[54] Y. C. Lin, C. L. Tseng, W. C. Chou, C. H. Chia, T. C. Han, and J. L. Shen, The Journal of Physical Chemistry C **115**, 19962 (2011).

[55] J. S. Reparaz, L. R. Muniz, M. R. Wagner, A. R. Goñi, M. I. Alonso, A. Hoffmann, and B. K. Meyer, Appl. Phys. Lett **96**, 231906 (2010).

[56] J. Huso, J. L. Morrison, L. Bergman, and M. D. McCluskey, Physical Review B **87**, 125205 (2013).

[57] W. L. Dang, Y. Q. Fu, J. K. Luo, A. J. Flewitt, and W. I. Milne, Superlattices and Microstructures **42**, 89 (2007).

[58] V. Gupta and A. Mansingh, Journal of Applied Physics **80**, 1063 (1996).

[59] J. L. Morrison, J. Huso, H. Hoeck, E. Casey, J. Mitchell, L. Bergman, and M. G. Norton, Journal of Applied Physics **104**, 123519 (2008).

[60] B. K. Meyer, H. Alves, D. M. Hofmann, W. Kriegseis, D. Forster, F. Bertram, J. Christen, A. Hoffmann, M. Straßburg, M. Dworzak, et al., physica status solidi (b) **241**, 231 (2004).

[61] R. H. French, Journal of the American Ceramic Society **73**, 477 (1990).

[62] R. B. Laughlin, Physical Review B **22**, 3021 (1980).

Chapter 6

UV-Luminescent MgZnO Semiconductor Alloys: Nanostructure and Optical Properties

6.1 Introduction

As discussed in chapter 1, the $Mg_xZn_{1-x}O$ alloy has become a highly desirable material in UV optoelectronics. To successfully utilize this alloy system for device application, it becomes crucial to optimize their UV luminescent properties. Particularly, a strong UV luminescence is highly desirable for their uses in device applications. However, the as-grown $Mg_xZn_{1-x}O$ alloy generally contains large number of defects, in the presence of which, the UV-PL emission is highly diminished. Unlike in ZnO films, in which native and structural defects are prevalent (chapter 5), the alloy system may exhibit some additional form of defects which can impact the alloy's optical properties. These additional defects inherent to our alloy system are as follows:

- Phase segregation of cubic and wurtzite structure: as we discussed in chapter 4, for a certain range of Mg composition, sputtered $Mg_xZn_{1-x}O$ alloy films exhibit a phase segregation region in which the wurtzite as well as cubic phase may coexist. Thus, in the phase segregation range, the alloy usually emits two relatively weak UV-PL lines corresponding to the two different phases. Additionally, in such case, the absorption edge becomes broadened.

- Fluctuations, i.e. inhomogeneity in alloy composition: For example, the alloy can be in a single wurtzite phase, however, some domains are more Zn-rich than others. In this case, as will be discussed in section 6.4, the luminescence can exhibit two or multiple lines reflecting the fluctuation in the alloy composition.

In this chapter, since our focus is on optimization of the optical properties of the alloy film with a smaller Mg composition (17 at.%), the phase segregation may not

be an issue. Thus, in this section we will mainly investigate the possible role of other defects such as alloy fluctuation, structural defects and native defects on the alloy's optical properties.

In our effort to optimize the optical properties of $Mg_{0.17}Zn_{0.83}O$ alloy films that were grown by a reactive DC magnetron sputtering technique, we performed a post growth annealing treatment under Ar atmosphere. As-grown and Argon annealed samples were studied via scanning electron microscopy (SEM), X-ray diffraction (XRD), atomic force microscopy (AFM), transmission, photoluminescence (PL), and micro-Raman scattering. The as-grown alloy was found to be segregated into Zn-rich and Mg-rich domains, had poor morphology, and exhibited defect-related PL in the visible range while the UV-PL was weak. Annealing at 900 °C under Argon atmosphere was found to significantly improve the nanostructure, solubility, and optical properties of the alloy, specifically that of the desired UV luminescence. Moreover, the inherent internal compressive stress in the nanocrystalline film was found to relax upon annealing.

6.2 Synthesis and annealing of the $Mg_xZn_{1-x}O$ alloy films

$Mg_{0.17}Zn_{0.83}O$ alloy films were grown by reactive DC magnetron sputtering using custom Zn Mg targets (99.99%) with 30W of power and (0001) sapphire substrates. In this paper we will refer to the alloys as MgZnO. The chamber was evacuated to a base pressure of 10^{-6} Torr before growth. A total working chamber pressure of 11 mTorr was used, with high purity Ar as the working gas and high purity O_2 as the reactive gas. The gas flow was held constant throughout the experiment using MKS p4b mass flow controllers. The substrates were held at a constant temperature of 250 °C throughout growth. The thickness of the films were $\sim$ 350 nm.

The photoluminescence experiments were carried out using a JY-Horiba Fluorolog-3 spectrometer with an excitation source of a Xe lamp. The cold temperature, 77 K, Raman and PL measurements were performed utilizing a Jobin Yvon T64000 micro

Raman and PL system in conjunction with an Instec 621 V microcell customized for UV measurements. The transmission spectra were collected at room temperature using an Agilent Cary 300 spectrophotometer operating in double beam mode to remove substrate effects. The film composition was determined to be $\sim$ 17% Mg by energy dispersive X-ray spectroscopy (EDS). The surface morphology of the films was examined utilizing SEM. The structural properties of the films were determined by XRD using a Siemens Diffractometer D5000 with the CuKα1 line operating in 2 theta mode.

For post annealing experiment, two as-grown samples were annealed for 1 hour under flowing, high purity Ar gas: one at 750 °C and another at 900 °C. The annealing experiments were performed utilizing a Lindberg/Blue M quartz tube furnace controlled by a Yokogawa UP-150 temperature controller. The as-grown sample was placed in a cleaned alumina boat and was inserted into the quartz tube. The inlet and the outlet gas flexible-tubes were connected via compression fittings. Initially the gas lines were purged at room-temperature for 10 minutes, setting the Ar flow-rate at 1255 cm^3/min. Subsequently, the Ar flow rate was reduced to 273 cm^3/min and the annealing process was started.

6.3 Results and discussion

6.3.1 SEM and XRD: morphology related studies

The surface morphology of the as-grown and the two Ar annealed films were studied via SEM, and representative images are presented in Figure 6.1 (b, c, d). For comparison purposes an image of an as-grown ZnO film is also included (Figure 6.1(a)). As can be seen in Figure 6.1(b), the as-grown MgZnO film displays a rough granular morphology with small grains of size $\sim$ 10 nm, which is much smaller than that of the as-grown ZnO $\sim$ 100 nm. The reduced grain size in MgZnO alloy films has been previously observed.[1,2] The XRD of the alloy films is presented in Figure 6.2, indicating the

preferential c-axis orientation of the wurtzite structure and a successive improvement of material quality upon annealing.

As will be discussed in a later section, the PL spectrum of the as-grown MgZnO film exhibits two peaks in the UV region, as can be seen in Figure 6.7. One peak is at 3.25 eV, attributed to Zn-rich domains, and the other is at 3.50 eV, attributed to Mg-rich domains, implying that the MgZnO is not fully alloyed. Due to the incomplete alloyed nature of the as-grown film, it is reasonable to assume that some of the MgO is in aggregate form in the grain boundaries. It has been previously reported that MgO in alumina ceramics acts as a grain size suppressor via the solute drag mechanism.[3] This mechanism involves the segregation of solute material to a grain boundary, which impedes grain boundary motion resulting in small grains. Similar behavior of grain growth impediment due to MgO has been also observed and analyzed for ZnO and ZnO-V2O5 varistors doped with Mg.[4,5] In these studies, an inverse correlation was found between the mole percent of the MgO to the grain size: the higher the percent the smaller the grain size.[4,5] The effect of MgO on the films microstructure may explain the difference in the grain size between the as-grown MgZnO and the ZnO films observed in our study.

Upon annealing at 750 °C, the smaller grains in that sample appear to agglomerate forming coarse clusters of grains (Figure 6.1 c). During annealing at this temperature, intermixing between the Zn-rich and Mg-rich wurtzite phase is initiated, and the MgO aggregates in the grain boundary may incorporate into the grains. The onset of the alloying process is further evidenced from the observed single broad UV-PL peak (Figure 6.7) and the relatively improved XRD. In a previous study by our group on $Mg_{0.10}Zn_{0.90}O$ ceramic, an onset of alloying was found to take place $\sim$ 800-900 °C, which concurs with the present results.[6] Additionally, in MgZnO thin film grown via pulse laser deposition (PLD), it was reported that a temperature $\sim$ 850 °C was required for the thermal diffusion of Mg to create the alloy.[7]

In contrast to the morphology of the as-grown, the image of the 900 °C annealed film presented in Figure 6.1 d shows an improved morphology with larger well-defined and smooth grains. To gain further knowledge on the surface morphology of the 900 °C, annealed alloy, AFM analysis was conducted, and its result is presented in Figure 6.3. As can be seen in the AFM images, the granular surface has a smoothness of only a few nano-meters: the height profile analysis indicated that the average surface roughness is ∼8.5 nm (with RMS value ∼1.6 nm). This surface quality may be understood in terms of the lateral growth of the grains in the annealed film. Figure 6.3c displays the height profile analysis performed along the line indicated in Figure 6.3a; and the average surface roughness is found to be ∼ 8.5 nm (with RMS value ∼ 1.6 nm). This surface quality may be understood in terms of the lateral growth of the grains in the annealed film. After annealing at 900 °C, the MgZnO film is expected to be fully alloyed, an assertion which is also supported by the significantly enhanced UV-PL peak 3.45 eV (Figure 6.7) and by the significantly improved XRD peak as can be seen in Figure 6.2. The rather smooth and lateral surface morphology can be understood in terms of the suppression of c-axis due to the addition of the MgO with rock salt structure. Similar results to ours have been reported previously for MgZnO film grown via Magnetron co-sputtering.[8] Also, in sol-gel MgZnO films, the addition of Mg was reported to markedly improve the surface flatness of the films.[1]

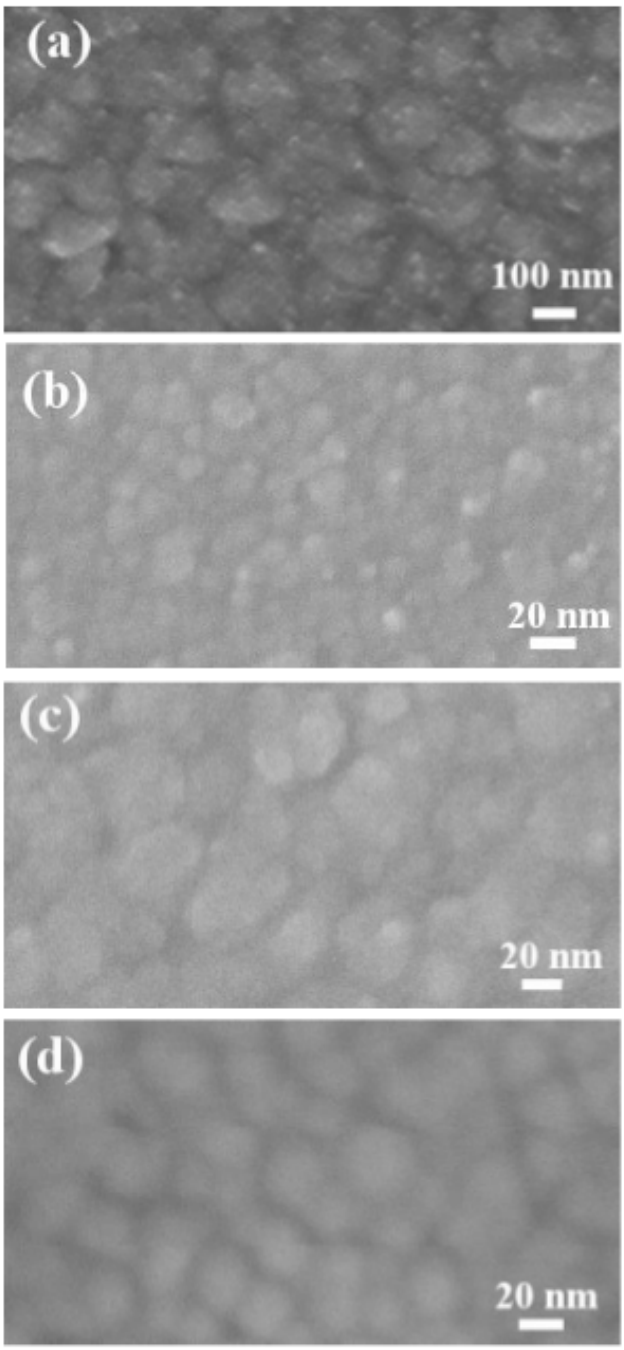

Figure 6.1: *Figure 1. The SEM images of: (a) ZnO as-grown film, (b) MgZnO as-grown, (c) MgZnO 750 °C, annealed, and (d) MgZnO 900 °C, annealed. The magnification of the SEM is 180 kX.*

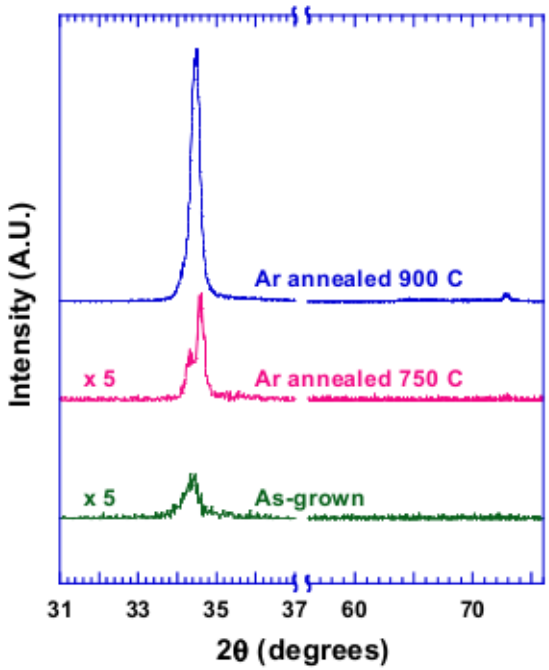

Figure 6.2: *XRD spectra of the MgZnO films: as-grown, and that of both annealed samples.*

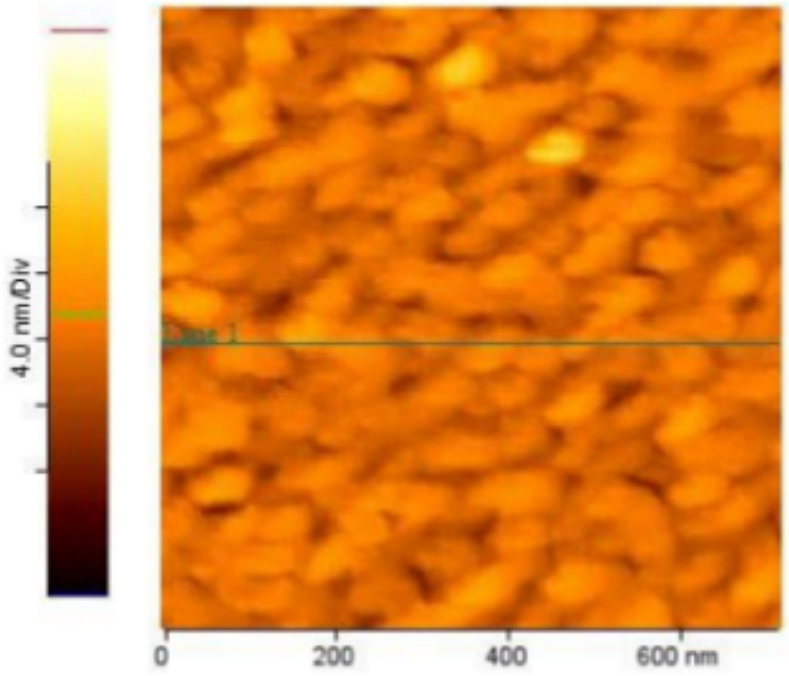

(a)

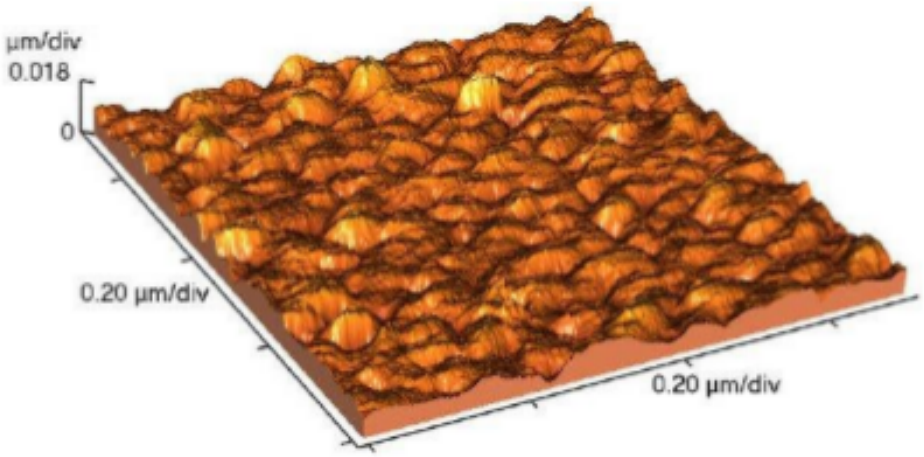

(b)

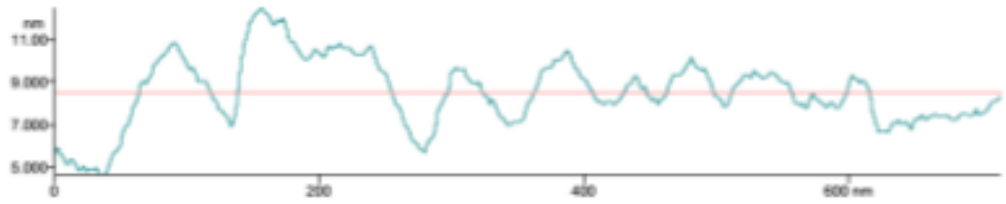

(c)

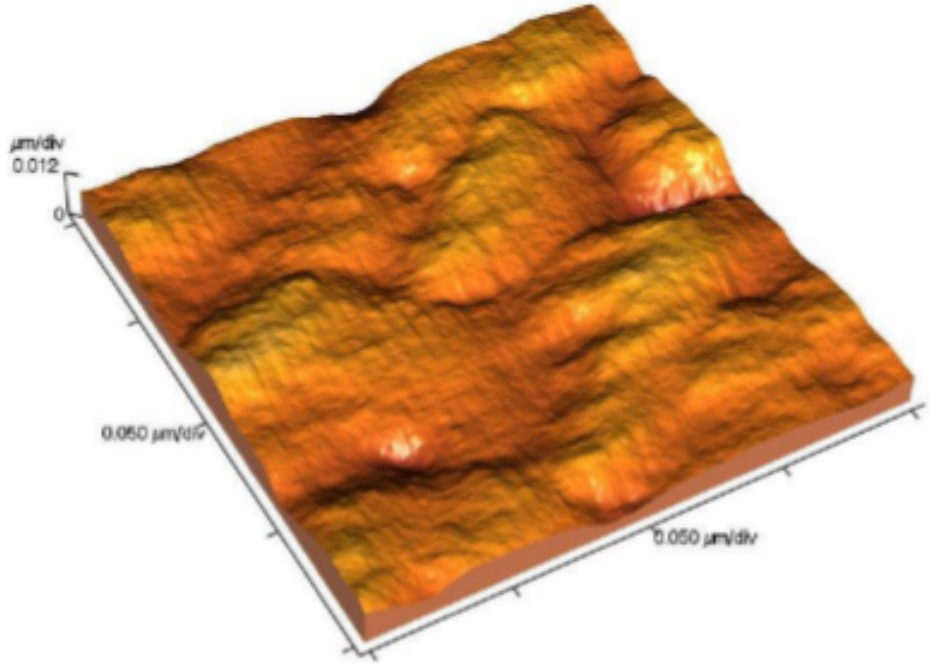

(d)

Figure 6.3: *AFM images of the 900 °C, annealed MgZnO: (a) A top view image, and (b) a side view: both images show an area ∼ 700 nm × 700 nm.,(c) The height profile extracted from the line in the upper figure; the scale of the axis is in nm. (d) A zoomed-in area 200 nm × 200 nm.*

6.3.2 Bandgap properties: transmission and Urbach analysis

Transmission spectroscopy may yield valuable information regarding the electronic structure of a semiconductor including its bandgap energy and the extent of the in-gap defect states. The bandgap energy can be ascertained via Tauc analysis, while the in-gap properties can be studied via Urbach analysis.[9,10] These two methods are well-established and commonly used for the investigation of semiconductor properties.[11–13] Figure 6.4 presents the transmission spectra of the as-grown and the two annealed samples; while Figure 6.5 depicts the Tauc analysis for the MgZnO samples and that for an annealed ZnO sample. As indicated in Figure 6.5, the bandgap of the three alloys are very similar $\sim$ 3.5 eV, while that of ZnO is at 3.29 eV; a bandgap shift of $\sim$ 200 meV was achieved via alloying.

Typically, the presence of defects in a semiconductor alloy that include impurities, structural disorders, and alloy compositional fluctuations as well as phase segregation, are known to produce localized energy states (band tail) within the bandgap. A good measure of the extent of these states may be given by the Urbach energy, E_U.[14,15] According to the Urbach model, the absorption coefficient below the optical bandgap follows exponential dependence with the photon energy, $\alpha(E) = Ce^{\frac{E}{E_U}}$, where C is a constant, $\alpha(E)$ is the absorption coefficient as a function of energy, which can be extracted utilizing transmission spectra via the relation $\alpha = -\frac{lnT}{t}$, t being the thickness of the film. Figure 6.6 presents the Urbach analysis for the alloys, which yields E_U values of 97 meV for the as-grown film, 52 meV for the 750 °C annealed film, and 45 meV for the 900 °C annealed film, respectively.

The gradual reduction in the Urbach energy of the films as a function of annealing temperature implies the trend of defect elimination. One type of defect is the morphology of the film. As is evident from the SEM and the XRD analyses discussed above, the film morphology was step-wise improved, starting as a degraded morphology for

the as-grown film and improving as a function of annealing temperature. Another type of defect of impact that will be discussed in detail in the following section is the domain segregation in the alloy, which was significantly reduced upon increasing annealing temperature.

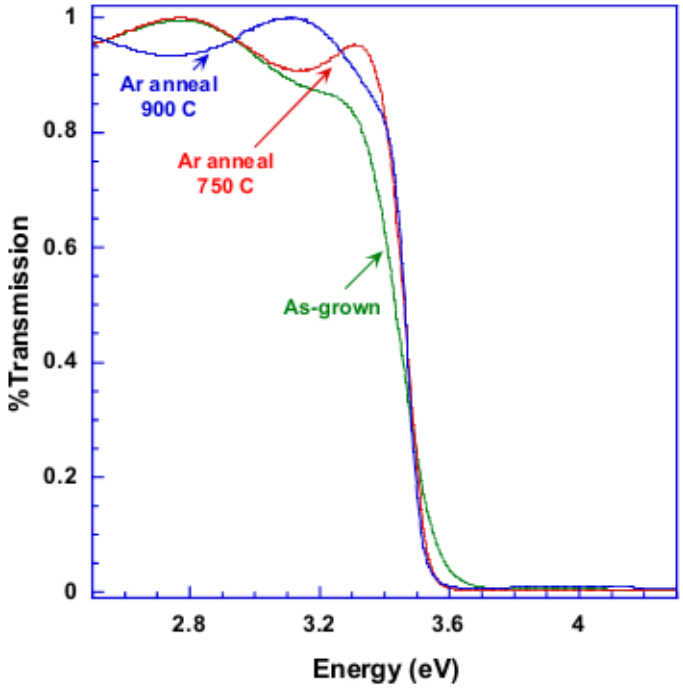

Figure 6.4: *The transmission spectra of the three MgZnO films. Both annealed films exhibits sharp bandedge.*

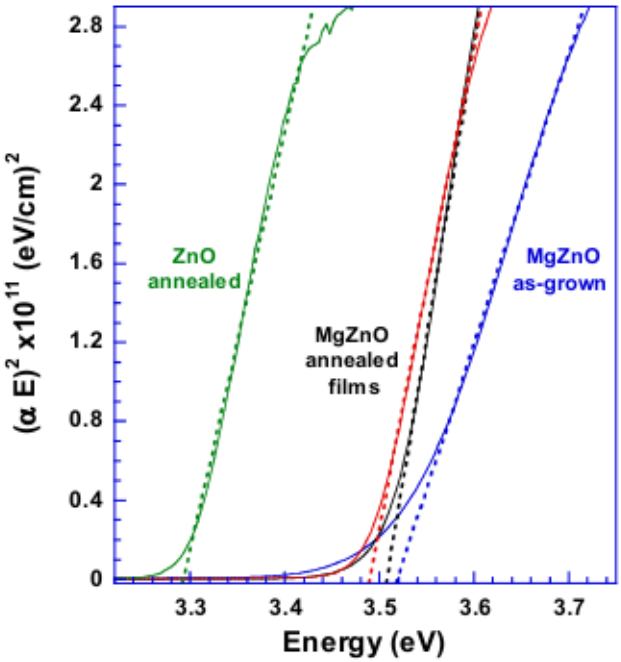

Figure 6.5: *The Tauc plots for the determination of the bandgaps. The as-grown alloy has a bandgap of 3.52 eV, that of the 750 °C annealed film is 3.51 eV, and for the 900 °C annealed film is 3.49 eV. The bandgap of the ZnO Argon annealed is 3.29 eV. A shift of ∼0.2 eV was achieved via alloying.*

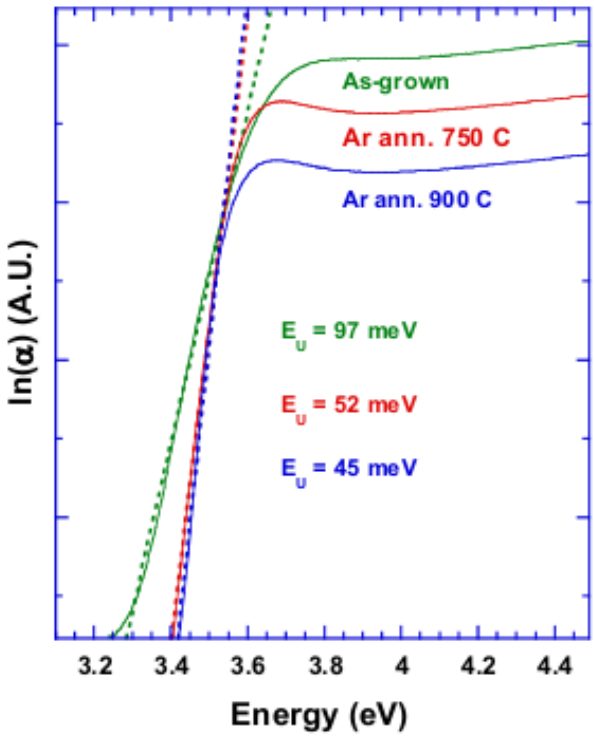

Figure 6.6: *The Urbach energy analysis. Urbach energy is 97 meV for the as-grown film, 52 meV for the 750 °C annealed film, and 45 meV for the 900 °C annealed film.*

6.3.3 Photoluminescence: from the visible to the UV range of the spectrum

As can be seen in Figure 6.7, the visible PL of the as-grown sample exhibits a broad PL centered at $\sim$ 2.3 eV. Such visible PL has been observed and studied by several groups in ZnO material.[16,17] The general consensus is that a visible PL in the range of 2.3 eV-2.4 eV, referred to as the green PL, is mainly due to oxygen vacancy (V_{O}) native defects in ZnO.[16–18] Since our alloy has relatively low Mg composition, one may expect that its green PL is in a similar energy range as that of ZnO. Further insight into the origin of the green PL of MgZnO can be inferred from the annealing studies. Figure 6.7 indicates that upon annealing at 750 °C and 900 °C the green PL at $\sim$ 2.3 eV was significantly diminished, and a weak PL at$\sim$ 2.18 eV appeared. This is in contrast with previous studies that have shown that annealing in reduction atmospheres, such as N_2:H_2, and argon gases, has the tendency to increase the green PL.[16,18] Additionally, studies via XRD and resistivity of annealed ZnO have indicated the loss of oxygen due to evaporation, which in turn resulted in the creation of V_{O}.[19]

Another important factor to consider in order to understand the origin of the green PL with relation to V_{O} in the MgZnO, is the issue of the formation energy of vacancies. Density functional calculations found that the vacancy formation energy of oxygen in ZnO is 7.01 eV, while in MgO it is much higher at 10.08 eV.[20] This implies that in MgZnO, due to the presence of Mg ions, the creation of V_{O} should be less thermodynamically favorable than in ZnO. There are emerging reports that MgZnO might be a viable component in ZnO-based transistor technology due to its lower V_{O} defects that may improve device performance.[21,22] In light of the above discussion we suggest that the 2.3 eV emission in our MgZnO is not due to V_{O}. Previous work by Trunk et al. on $Mg_xZn_{1-x}O$ films grown by metal-organic vapor phase epitaxy have suggested that the PL at $\sim$2.30 eV is due to transitions that involve intrinsic shallow donors to deep

acceptors.[23] Such transitions can occur between Zn_i to O_i energy levels, and possibly Mg_i to O_i.[23] As is discussed below, our annealing experiments support this assertion.

As can be seen in Figure 6.7, the 2.3 eV PL-band was almost entirely diminished after the annealing procedure, indicating the removal of some of its related native defects. It is expected that during annealing under Ar atmosphere, most interstitial defects diffuse out or incorporate into the lattice sites. While the migration barrier for Zn_i in $Mg_xZn_{1-x}O$ is not currently available, the low migration barrier for Zn_i in ZnO[24–26] suggests that any Zn_i related defects will diffuse out rapidly upon annealing of the alloy. From density functional calculations, Janotti et al. reported the migration barrier of Zn_i to be 0.57 eV, which is considered to be relatively low.[24] Alternatively, the mobility temperature of these defects, which was previously found to be $\sim$170 K[27], is significantly lower than our annealing temperature range at 1173 K and 1023 K (for further discussion on the stability of Zn_i in our samples see ref. 28). In light of these properties, it is reasonable to expect that Zn_i related defects should be eliminated by out- diffusion as well as via incorporation into substitution lattice sites, thus diminishing the 2.3 eV PL emission. Our previous work on MgZnO ceramics found that the onset of Mg diffusion is $\sim$ 800 °C to 900 °C,[6] a similar diffusion temperature was found for MgZnO films grown via pulsed laser deposition.[7] These findings may imply that Mg atoms, via annealing as in the case of Zn_i, may be removed from their interstitial sites into lattice substitutions or out-diffused, thus diminishing the radiative recombination of the 2.3 eV. With regard to the relative weak PL at 2.18 eV that appears upon annealing (see Figure 6.7), tentatively we associate it with the small concentration of vacancies-type defects that were created during the anneal process.

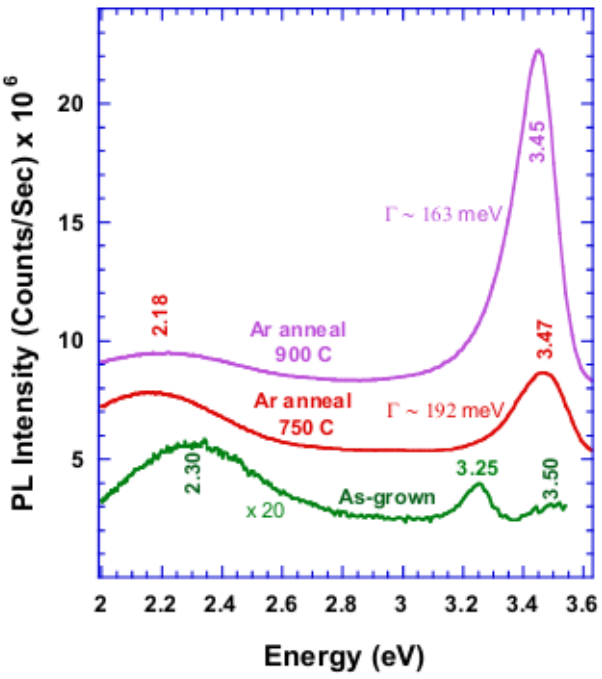

Figure 6.7: *The PL spectra of the three alloys acquired at room-temperature. The as-grown exhibit visible PL at* $\sim$ *2.30 eV and two UV-emissions, one at 3.25 eV attributed to segregation of Zn rich domains, and the other at 3.50 eV due to Mg-rich domains. The UV-PL of the 750* $^\circ$*C, annealed film is a broad linewidth* $\sim$ *192 meV attributed to a residual segregation. The UV-PL properties of the 900* $^\circ$*C, is significantly improved: it has enhanced intensity* $\sim$ *4 times that of the 750* $^\circ$*C, annealed film, and a narrower linewidth* $\sim$ *163 meV.*

6.3.4 Improved solubility of MgZnO alloy film

One of the key desirable features among the optical properties of MgZnO alloys is their bandedge UV luminescence capability. In has been previously demonstrated that the UV-PL of ZnO can be profoundly enhanced via annealing.[28] Less work has been done regarding this topic for MgZnO alloys.[29,30] Figure 6.7 demonstrates the impact of annealing on the UV emission of our MgZnO films. As can be seen in Figure 6.7, the effect of annealing at the two elevated temperatures is the diminishing of the doublet peaks one at 3.25 eV, attributed to Zn rich domains in the MgZnO alloy, and the other at 3.5 eV attributed to Mg-rich domains. The annealing temperatures of 750 °C, and 900 °C, are well within the range of Mg and Zn thermal diffusions[6,7], which facilitates an improved mixing of the alloy constituents. The PL line width of the 750 °C, annealed sample $\sim$ 192 meV is considered to be quite broad, reflecting the existence of residual segregation. The narrowing of the line to $\sim$ 163 meV for the 900 °C, annealed film indicates the improved solubility of this sample.

The other optical impact of annealing, as was discussed above, is the reduction of native defects that luminescence at $\sim$ 2.3 eV. This defect reduction may eliminate a competing route to the UV luminescence in the MgZnO bandgap contributing the efficiency of the bandedge UV luminescence. The fact that the major native defect contributing luminescence at 2.3 eV was diminished significantly during the 750 °C, annealing as well as during the 900 °C, annealing; however, only the 900 °C, annealed sample exhibits enhanced UV luminescence that correlates well with its good structural morphology and its homogenity of alloy mixing. Thus, for the 900 °C, annealed film, the significant enhancement of the UV-PL relative to that of the as grown film is mainly assigned to the combined effect of being a more complete soluble alloy, an improved morphology. It bears noting that annealing of MgZnO at much higher temperatures may not be a stable route for optimizing the optical properties of the alloy. The high

vapor pressure of Zn may cause its out-diffusion, changing the composition of a given alloy to become a more Mg-rich.[31]

The impact of a random distribution of the atomic constituents in ternary semiconductor alloys is to broaden the PL linewidth significantly relative to that of the pure end-members. This is a well-known phenomenon, referred to as the alloy or inhomogeneous broadening, which takes place even in high-quality epitaxial films such as $Al_xGa_{1-x}As$, and is due to fluctuation in the distribution of the substitution atoms, Zn and Mg in our case.[32] Figure 6.8 presents the PL at 77 K of annealed MgZnO and that of annealed ZnO films. Both samples have similar granular morphology. The UV-PL of the ZnO shows the expected emissions of the excitons and the emission which is characteristic to nanocrystalline-type ZnO studied previously in our papers.[28,33] The key issue is that in contrast to the ZnO, the PL of the MgZnO is featureless and broad with a linewidth $\sim$ 88 meV. This implies that even at the relatively low Mg composition $\sim$ 17% the impact of the inherent alloy random distribution is quite significant.

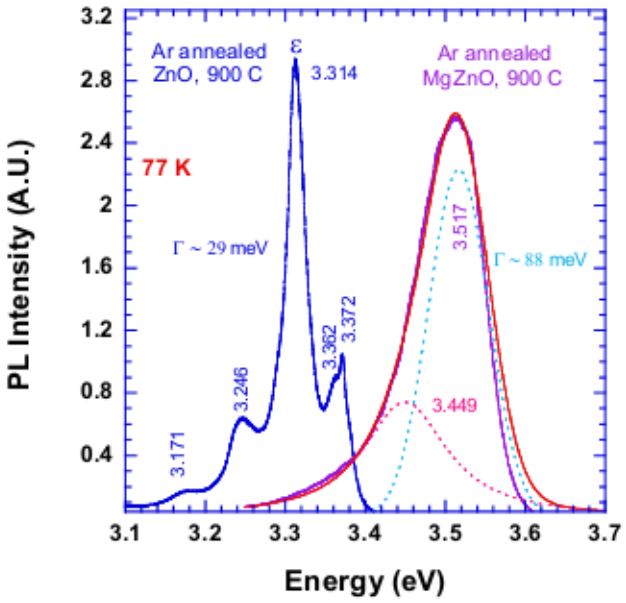

Figure 6.8: *The 77 K UV-PL spectrum of the MgZnO 900 °C, annealed film. For comparison, the PL of a ZnO film is included that indicates its emission characteristics: excitons at the high energy range, ε – emission at 3.314 eV, and phonon replicas at the lower energy range. The PL of the alloy exhibits broadening, attributed to the random distribution of the atomic Mg and Zn substitution atoms which masks the fine structure of the luminescence. The fit to the data shows the main PL at 3.517 eV, and its phonon-replica.*

6.3.5 Raman scattering and internal stress in the film

In addition to improved solubility and optical properties, annealing is also expected to relax the internal stress in the films. In general, Raman scattering has proven to be a highly sensitive spectroscopy, enabling the assessment of a material's internal stress via the frequency shift of a particular Raman mode. In our experiments, Raman spectra were acquired in a back scattering geometry at 77 K utilizing the 325 nm (3.81 eV) HeCd laser line. The experimental error is $\sim$ 1 cm^{-1}. Since that excitation energy is close to the bandgap of the MgZnO, resonant Raman scattering occurs, resulting in enhanced LO-mode.[34] Figure 6.9 presents the Raman spectra of the two samples of interest: the as-grown as a reference, and that of the 900 °C, annealed films. As can be seen in Figure 6.9, the LO-mode exhibits a shift towards the lower frequency: it is at 611 cm^{-1} for the as-grown sample, and 602 cm^{-1} for the annealed one; i.e., a total shift of $\sim$ 9 cm^{-1}. The shift towards the lower frequency may be suggestive of a relaxation of intrinsic compressive stress.

The pressure coefficient $\left(\frac{\partial\omega}{\partial P}\right)$ for the LO-mode in $Mg_{0.2}Zn_{0.8}O$ (where ω is the phonon frequency) was obtained previously by our group to be $\sim$ 4.9 cm^{-1}/GPa.[35] Since the observed Raman shift is $\sim$ 9 cm^{-1}, a relaxation of $\sim$ 1.8 GPa took place upon annealing. Furthermore, this relaxed stress of $\sim$ 1.8 GPa is comparable to those obtained previously via XRD and curvature measurement studies of ZnO thin films grown via the sputtering method.[36,37] Additionally, in our previous study of ZnO nanocrystalline films grown via the sputtering technique, Raman analysis has indicated a similar relaxation upon annealing of $\sim$ 1 GPa[28] Thus, the compressive stress in our as-grown MgZnO sample can be attributed mainly to morphology, and to some extent to defect aggregations, both of which were significantly reduced during the annealing process.

The deconvolution of the Raman peak indicates that in addition to the principle Raman line, a broad peak at lower energy phonon scattering is present, as can be seen

in Figure 6.9. Our previous study of LO-phonon dynamics in $Mg_{0.20}Zn_{0.80}O$ nanoalloys has concluded that the principle mechanism that activates such low frequency mode is scattering due to a disorder state of the nanoalloys as is expected in random type alloy distribution.[38]

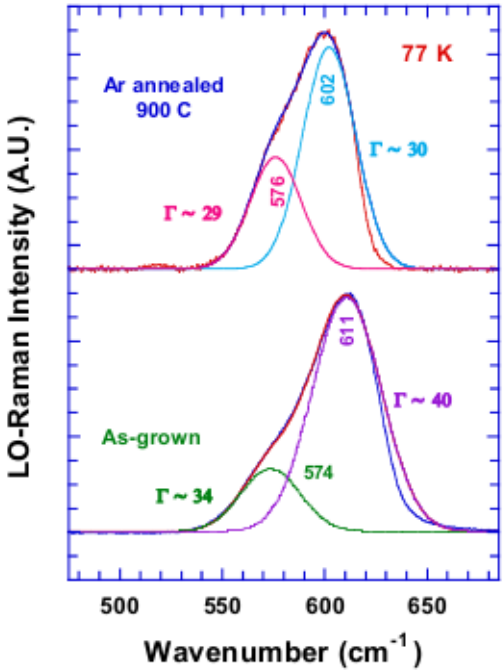

Figure 6.9: *The 77 K Raman spectra of the LO mode of the as-grown alloy and that of the 900 °C, annealed sample. The ∼9 cm^{-1} Raman shift between the two spectra is attributed to stress relaxation initiated by the high-temperature annealing.*

6.4 Conclusions

In this chapter, we presented the studies on the material and optical properties of wurtzite $Mg_{0.17}Zn_{0.83}O$ alloy films utilizing various techniques. The main finding of our work presented in this chapter is:

The UV luminescence of the alloy film was found to be impacted by two major defects: the extent of the mixing i.e., the homogeneity of the alloy and the film's morphology. Specifically, for the 900 °C annealed alloy film, the significant enhancement of the UV-PL relative to that of the as grown film was assigned to a combined effect of being a more complete soluble alloy, and an improved morphology.

Some of the other important results in this chapter are summarized as follows:

- The as-grown alloy was found to exhibit the incomplete alloy with the Zn-rich and Mg-rich segregated domains. Additionally, the as-grown alloy film displayed a degraded morphology, and was found to have a weak UV-PL accompanied with a pronounced visible PL at 2.30 eV.

- Annealing at 750 °C and 900 °C under Argon atmosphere improved the overall structural and optical properties of the alloys. Annealing under Ar enviroment at 750 °C led the onset of the alloying process between the Zn-rich and Mg-rich wurtzite phase resulting in the single broad UV-PL peak in the PL spectrum and the relatively improved XRD.

- The native defects responsible for 2.30 eV emission was found to largely diminish during the 750 °C annealing as well as during the 900 °C; however the 900 °C annealed samples exhibits enhanced UV luminescence that correlates well with its good structural morphology and its homogeneity of alloy mixing.

- The larger PL width of 750 °C annealed sample $\sim$ 192 was attributed due to

the effect of residual domain segregation of the alloy film while the relatively broader linewidth of UV-PL of the 900 °C alloy film relative to that of ZnO was attributed to the random nature of the alloy distribution at the atomic scale.

- A compressive stress relaxation of $\sim$ 1.8 GPa was found to take place upon annealing.

References

[1] C.-Y. Tsay, M.-C. Wang, and S.-C. Chiang, Materials transactions **49**, 1186 (2008).

[2] T. Murakawa, T. Fukudome, T. Hayashi, H. Isshiki, and T. Kimura, physica status solidi (c) **1**, 2564 (2004).

[3] I.-W. Chen, Materials Science and Engineering: A **166**, 51 (1993).

[4] A. Smith, G. Gasgnier, and P. Abélard, Journal of the American Ceramic Society **73**, 1098 (1990).

[5] H. H. Hng and K. Y. Tse, Ceramics International **34**, 1153 (2008).

[6] J. L. Morrison, J. Huso, H. Che, D. Thapa, M. Huso, M. G. Norton, and L. Bergman, Journal of Materials Science: Materials in Electronics **23**, 437 (2012).

[7] A. Ohtomo, R. Shiroki, I. Ohkubo, H. Koinuma, and M. Kawasaki, Applied Physics Letters **75**, 4088 (1999).

[8] S. W. Kang, Y. Y. Kim, C. H. Ahn, S. K. Mohanta, and H. K. Cho, Journal of Materials Science: Materials in Electronics **19**, 755 (2008).

[9] J. Tauc, R. Grigorovici, and A. Vancu, physica status solidi (b) **15**, 627 (1966).

[10] J. I. Pankove, *Optical processes in semiconductors* (Dover, New York, 1975).

[11] T. Aschenbrenner, H. Dartsch, C. Kruse, M. Anastasescu, M. Stoica, M. Gartner, A. Pretorius, A. Rosenauer, T. Wagner, and D. Hommel, Journal of Applied Physics **108**, 063533 (2010).

[12] A. M. El-Naggar, Journal of Applied Physics **109**, 023508 (2011).

[13] S. Dutta, S. Chattopadhyay, D. Jana, A. Banerjee, S. Manik, S. K. Pradhan, M. Sutradhar, and A. Sarkar, Journal of applied physics **100**, 114328 (2006).

[14] J. Huso, H. Che, D. Thapa, A. Canul, M. D. McCluskey, and L. Bergman, Journal of Applied Physics **117**, 125702 (2015).

[15] C. W. Teng, J. F. Muth, Ü. Özgür, M. J. Bergmann, H. O. Everitt, A. K. Sharma, C. Jin, and J. Narayan, Appl. Phys. Lett **76**, 979 (2000).

[16] K. Vanheusden, C. H. Seager, W. L. Warren, D. R. Tallant, and J. A. Voigt, Applied Physics Letters **68**, 403 (1996).

[17] F. H. Leiter, H. R. Alves, A. Hofstaetter, D. M. Hofmann, and B. K. Meyer, physica status solidi (b) **226**, R4 (2001).

[18] S. Ning, P. Zhan, Q. Xie, W. Wang, and Z. Zhang, Journal of Materials Science & Technology **31**, 969 (2015).

[19] S. Dutta, M. Chakrabarti, S. Chattopadhyay, D. Jana, D. Sanyal, and A. Sarkar, Journal of applied physics **98**, 053513 (2005).

[20] J. Carrasco, N. Lopez, and F. Illas, Physical review letters **93**, 225502 (2004).

[21] C.-J. Ku, Z. Duan, P. I. Reyes, Y. Lu, Y. Xu, C.-L. Hsueh, and E. Garfunkel, Applied Physics Letters **98**, 123511 (2011).

[22] S.-T. Lien, J.-Z. Chen, Y.-J. Yang, C.-C. Hsu, and I.-C. Cheng, Ceramics International **40**, 2707 (2014).

[23] M. Trunk, V. Venkatachalapathy, A. Galeckas, and A. Y. Kuznetsov, Applied Physics Letters **97**, 211901 (2010).

[24] A. Janotti and C. G. Van de Walle, Reports on Progress in Physics **72**, 126501 (2009).

[25] A. Janotti and C. G. Van de Walle, Journal of Crystal Growth **287**, 58 (2006).

[26] D. G. Thomas, Journal of Physics and Chemistry of Solids **3**, 229 (1957).

[27] M. D. McCluskey and S. J. Jokela, Journal of Applied Physics **106**, 071101 (2009).

[28] D. Thapa, J. Huso, J. L. Morrison, C. D. Corolewski, M. D. McCluskey, and L. Bergman, Optical Materials **58**, 382 (2016).

[29] A. L. Yang, H. P. Song, D. C. Liang, H. Y. Wei, X. L. Liu, P. Jin, X. B. Qin, S. Y. Yang, Q. S. Zhu, and Z. G. Wang, Applied Physics Letters **96**, 151904 (2010).

[30] Y. Y. Kim, C. H. An, H. K. Cho, J. H. Kim, H. S. Lee, E. S. Jung, and H. S. Kim, Thin Solid Films **516**, 5602 (2008).

[31] A. Ohtomo, M. Kawasaki, T. Koida, K. Masubuchi, H. Koinuma, Y. Sakurai, Y. Yoshida, T. Yasuda, and Y. Segawa, Applied Physics Letters **72**, 2466 (1998).

[32] E. F. Schubert, E. O. Göbel, Y. Horikoshi, K. Ploog, and H. J. Queisser, Physical Review B **30**, 813 (1984).

[33] J. L. Morrison, J. Huso, H. Hoeck, E. Casey, J. Mitchell, L. Bergman, and M. G. Norton, Journal of Applied Physics **104**, 123519 (2008).

[34] L. Bergman, X.-B. Chen, J. Huso, J. L. Morrison, and H. Hoeck, Journal of applied physics **98**, 093507 (2005).

[35] J. Huso, J. L. Morrison, L. Bergman, and M. D. McCluskey, Physical Review B **87**, 125205 (2013).

[36] V. Gupta and A. Mansingh, Journal of Applied Physics **80**, 1063 (1996).

[37] W. L. Dang, Y. Q. Fu, J. K. Luo, A. J. Flewitt, and W. I. Milne, Superlattices and Microstructures **42**, 89 (2007).

[38] J. Huso, J. L. Morrison, H. Hoeck, E. Casey, L. Bergman, T. D. Pounds, and M. G. Norton, Applied Physics Letters **91**, 111906 (2007).

Chapter 7

Main conclusion

The focus of this dissertation was to investigate the optical and material properties of the wide bandgap semiconductors: ZnO and $Mg_xZn_{1-x}O$ alloy films grown via sputtering technique. The films were studied utilizing XRD, imaging and several optical spectroscopic techniques, including transmission, photoluminescence, and Raman spectroscopy. The key aspects of our investigation include: a realization of bandgap engineering, study of phase segregation and structural in inhomogeneity inherent to the alloy films, and UV luminescent properties of ZnO and $Mg_xZn_{1-x}O$ alloy films. This chapter will summarize some of the important results of this work.

Major results

1. Bandgap engineering via the synthesis of $Mg_xZn_{1-x}O$ films

$Mg_xZn_{1-x}O$ films over a wide range of Mg composition ($0 \leq x \leq 0.78$) were synthesized via sputtering. The bandgaps of the alloy films were determined utilizing derivative and Tauc plot methods. The bandgaps of the $Mg_xZn_{1-x}O$ alloy films were found to span the UV range of 3.4-5.85 eV. Additionally, the transmission spectra of the $Mg_xZn_{1-x}O$ films were found to be broadened with the increasing Mg content, and the underlying mechanisms for this behavior were attributed to the inherent structural imperfection, and alloy inhomogeneities of the films with increasing Mg content. Specifically for the ZnO and $Mg_{0.17}Zn_{0.83}O$ films, the bandedge behavior were analyzed via Urbach analysis.

2. Structural inhomogeneities embeded in $Mg_xZn_{1-x}O$ alloy films

The issue of phase segregation, inherent to the $Mg_xZn_{1-x}O$ alloy system, was inves-

tigated via SRRS. Via this technique, the phase segregation of the studied alloy system was found to be approximately 35-65 at% of Mg composition. We also demonstrated that SRRS was a highly sensitive and very useful technique in probing the minority phases in a size regime too small to be detected by XRD. Thus, via SRRS, we managed to achieve a refined range for the phase segregation, inherent to the $Mg_xZn_{1-x}O$.

3. Defect dynamics and an enhanced UV-PL of ZnO films

The defects dynamics and UV luminescent properties of the sputtered ZnO films were analyzed via luminescence spectroscopy. The as-grown films were found to exhibit relatively a weak UV-PL $\sim$ 3.25 eV, and an additional pronounced visible PL at $\sim$ 2.8 eV attributed to Zn_i-related defects. Their presence was attributed to the nature of the sputtering growth technique which supports Zn-rich growth conditions.

After annealing under each Ar and O_2 environment at a high annealing temperature at 900 °C, the 2.8 eV center appeared for the as-grown films were diminished accompanied by morphology improvement, and the desirable UV-PL was significantly enhanced. The O_2 ambient was found to introduce nominal O_i centers while the Ar ambient was turned out to be the ideal environment for the enhancement of the UV-light emission: an enhancement of $\sim$ 40 times was achieved. The significant enhancement in the UV-PL was attributed to the reduction of Zn_i-related defects, the presence of which in ZnO provides a competing route to the UV emission. Additionally, the enhanced UV-PL in the annealed films were found to correlate with the improved morphology of the films.

4. Optimization of the optical and material properties of MgZnO films

In an effort to optimize the optical properties such as UV luminescence, band-edge properties of the $Mg_xZn_{1-x}O$ alloy film, we investigated the optical and material properties of the $Mg_{0.17}Zn_{0.83}O$ nanocrystalline film utilizing different techniques. The

as-grown nanocrystalline alloy film was found to exhibit a weak UV-PL characteristic of Zn-rich and Mg-rich segregated domains, confirming an incomplete alloyed nature of the as-grown film. Additionally, the alloy film was found to display a degraded morphology, and exhibit a pronounced visible PL$\sim$ at 2.30 eV. The major native defect contributing to luminescence at 2.3 eV was found significantly diminished upon annealing at 750 °C as well as 900 °C annealing. However, the 900 °C annealed samples exhibits enhanced UV luminescence correlated well with its good structural morphology and its inhomogeneity of alloy mixing. Thus, the major defects impacting the UV luminescence of the alloy were attributed to inhomogeneity in alloy composition and film's morphology.